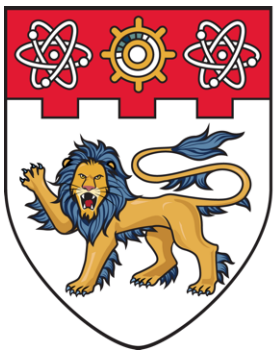

NANYANG TECHNOLOGICAL UNIVERSITY
SINGAPORE

DUAL ATOMIC INTERFEROMETRY FOR DIFFERENTIAL INERTIAL SENSING

LI JIANING

SCHOOL OF PHYSICAL AND MATHEMATICAL SCIENCES

2023

DUAL ATOMIC INTERFEROMETRY FOR DIFFERENTIAL INERTIAL SENSING

LI JIANING

SCHOOL OF PHYSICAL AND MATHEMATICAL SCIENCES

A thesis submitted to the Nanyang Technological University in partial fulfilment of the requirement for the degree of Doctor of Philosophy

2023

Statement of Originality

I hereby certify that the work embodied in this thesis is the result of original research done by me except where otherwise stated in this thesis. The thesis work has not been submitted for a degree or professional qualification to any other university or institution. I declare that this thesis is written by myself and is free of plagiarism and of sufficient grammatical clarity to be examined. I confirm that the investigations were conducted in accord with the ethics policies and integrity standards of Nanyang Technological University and that the research data are presented honestly and without prejudice.

29/11/2023

. . . . . .
Date

. . . . . .
Li Jianing

Supervisor Declaration Statement

I have reviewed the content and presentation style of this thesis and declare it of sufficient grammatical clarity to be examined. To the best of my knowledge, the thesis is free of plagiarism and the research and writing are those of the candidate's except as acknowledged in the Author Attribution Statement. I confirm that the investigations were conducted in accord with the ethics policies and integrity standards of Nanyang Technological University and that the research data are presented honestly and without prejudice.

29/11/2023

. . . . . .
Date

. . . . . .
Prof. David Wilkowski

Authorship Attribution Statement

This thesis contains material from one paper published in the following peer-reviewed journal in which I am listed as an author.

Chapter 1 (part of the introduction), Chapter 3, Chapter 6 (part of the conclusion) are published as Jianing Li, Kelvin Lim, Swarup Das, Thomas Zanon-Willette, Chen-Hao Feng, Paul Robert, Andrea Bertoldi, Philippe Bouyer, Chang Chi Kwong, Shau-Yu Lan, and David Wilkowski. Bi-color atomic beam slower and magnetic field compensation for ultracold gases. AVS Quantum Science, 4(4):046801, 12 2022.

The contributions of the co-authors are as follows:

- Prof. David Wilkowski and Prof. Andrea Bertoldi provided the initial project direction, review and editing the manuscript drafts.
- I constructed the experimental system with Dr. Swarup Das and Dr. Chang Chi Kwong.
- Kevin Lim and Dr. Chang Chi Kwong constructed the active feedback system for magnetic field.
- I collected and analyzed data with Dr. Swarup Das, Dr. Chang Chi Kwong and Kelvin Lim.
- I prepared the original draft with Dr. Swarup Das, Dr. Chang Chi Kwong and Kelvin Lim. The manuscript was revised together with all the co-authors listed in this paper.

29/11/2023

Date

Li Jianing

Abstract

The utilization of light-pulse atom interferometry presents a valuable technique that has found application in both fundamental scientific inquiries, such as investigating constants such as measurements of fine structure constant α and gravitational constant G, and practical endeavors including acceleration sensing and rotation measurements. This thesis delves into our implementation of a dual atom interferometer design involving the clock transition $^1S_0 \rightarrow {}^3P_0$ in strontium, concurrently conducting the interferometric sequence on atoms in both ground and excited states.

To facilitate the dual atom interferometer's operation, we have firstly established a compact experimental setup with a transversely loaded bi-dimensional magneto-optical-trap (2D-MOT) to create a high flux source of cold strontium atoms. Introducing a novel cross-polarized bi-color atomic beam slower, we simultaneously addresses two excited Zeeman substates of the transition $^1S_0 \rightarrow {}^1P_1$ in strontium-88, significantly enhancing the number of atoms prepared in the 461 nm MOT by around 10-fold. Following the 461 nm MOT, the atomic ensemble undergoes cooling in a 689 nm MOT, achieving atomic temperatures below 1 μK. We also install a network of eight magnetic field probes arranged around the cold atomic sample, enabling precise three-axis active control of magnetic fields down to the milligauss level.

With the atoms confined in a 2D lattice at the magic-wavelength of 813.427 nm after the initial preparation phase, we conduct the magnetically-induced clock transition to create a statistical mixture state of ground and excited states. After a velocity selection stage, implementing a Mach-Zehnder interferometer with Bragg pulses operating at the magic-wavelength along the vertical axis, we conduct tests of the weak equivalence principle (WEP).

The Eötvös ratio we found in our system stood at $(1.8 \pm 3.1) \times 10^{-4}$, mainly limited by the finite temperature of the atomic cloud constraining the interrogation time. Furthermore, the dual atom interferometer scheme enables the measurement of state-dependent force and eventually polarizability difference via the phase shift between the atoms in different states, and we experimentally demonstrate this by introducing an additional light field gradient.

Dedication

To the people I cross paths with.

Acknowledgements

First of all, I would like to thank my supervisors, Prof. David Wilkowski and Prof. Lan Shau-Yu, who give me this opportunity to work on this interesting project as a PhD student. Spending four and a half years in David's research group has been truly a lasting and invaluable experience. David is a encouraging, supportive and friendly advisor. His expertise and raw enthusiasm for research are really inspiring and have helped me to be more and more independent in research. I am grateful for the guidance and positive atmosphere within the group, which has undoubtedly shaped my academic and professional journey in significant ways. Prof. Lan is an expert in quantum sensing and atom interferometry, he and his deep insight into scientific research also has provided invaluable information during this four and a half years. I am truly fortunate to have had their patient guidance and help.

There are many people behind the work presented in this thesis. I am grateful to my labmates who played pivotal roles in this project: Swarup, Chang Chi, and Kelvin. When I joined in the research group, I was unfamiliar with the atomic physics experiment. With their great patience, Swarup and Chang Chi have taught me a lot of things from preparation of vacuum chamber, optical alignment to electronics stuff. Starting from a scratch, their knowledge, experience and skill were invaluable to construct the experimental setup. Kelvin also contributed a lot on building up an active control system for the magnetic field and calibration of the clock laser system, all of which are helpful for us to have a stable experimental system. Collaborating with them has been a fortunate and enriching experience, and I am genuinely grateful for the collective efforts on this research project.

I extend my appreciation to my labmates in SrI project: Chetan, Mehedi, Chirantan, and all the members that did not coincide with my graduate career. They built up a really nice experimental setup for SrI, which provided us invaluable experience and references for our SrII project. Special gratitude goes to Chetan, who has helped us a lot in data analysis and constructing the lab control system.

I am also deeply grateful to my labmates from Prof. Lan's group: Mingjie, Wui Seng, Wnag Yu and Zilong. They are experienced in atom interferometer and have provided insightful advice sometimes when things are not going great. Talking with them has been really inspiring and helpful in various aspects, and I am sincerely grateful for all of the help they provided.

I am thankful to my friends and roommates whose companionship makes my life in Singapore more colorful. I did not manage to go home during Chinese New Year for three consecutive years due to the challenges posed by the COVID circumstances. However, the joy and warmth I experienced while spending time with them during this festive period truly created lasting memories.

My appreciation also goes out to the important people I met in Shanghai. They are really excellent and have been teaching me things that I did not manage to learn in universities. I am grateful for all of the warm acceptance and moments of happiness, which do brighten some parts of my live. I spent too much time on study, but getting along with them also makes me realize that a fulfilling life is not only about exploration and mountaineering, but also to give the people around you a bit more

happiness, thoughtfulness and hope. From the bottom of my heart, I hope you all the best and I look forward our company over many many years.

Lastly, and most importantly, I am grateful to my amazing parents and families for everything they have done. Their love, support, encourage and sacrifices have shaped the person I am today. From as far back as I can remember, their thankless care has been a constant source of strength.

Contents

List of Figures

List of Tables

Chapter 1

Introduction

The central focus of this thesis is to establish an experimental setup for the implementation of a dual atom interferometer based on clock transition in strontium. This chapter serves as an introduction to atom interferometry (AI) and outlines the properties of the bosonic isotope, strontium-88, crucial to our dual AI approach. Furthermore, this chapter offers an outline of the contents covered in the thesis.

1.1 atom interferometer (AI)

Since the first demonstration of laser cooling and trapping [7][8], cold and ultracold atoms have been instrumental across diverse domains, spanning quantum sensing, quantum metrology, and quantum simulation. A key application is the precision measurements facilitated by atom interferometry. Analogous to optical interferometers, in an atom interferometer, the wave-function of atoms is coherently splitted, going through different paths and then recombined. The information during this process can be encoded into the interferometry phases [9]. This can be used for fundamental scientific, notably the measurement of significant constants like the gravitational constant [10][11], which is crucial to characterize the interaction between light and charged elementary particles. Moreover, the precision measurements conducted by atom interferometry proves beneficial in technological contexts such as gravitational surveys [12][13][14][15][16] and rotation measurement [17][18].

One of the major interests for the thesis is using atom interferometer for the test of weak equivalence principle (WEP), a fundamental concept in general relativity. The rigorous constraints on Eötvös ratio have been achieved with platforms such as torsion balances in a laboratory setting [19][20] (10^{-13}), Lunar ranging[21] (10^{-13}) or Earth's orbit[22] (10^{-15}). On the other hand, the construction of atom interferometers with various atomic species or atoms in different states enables testing the weak equivalence principle (WEP) with an uncertainty of 10^{-12}[23][24][25][26]. Several strategies have been proposed to enhance the accuracy and reduce uncertainties of this test using atom interferometer. Noteworthy examples include the STE-QUEST project, proposing a WEP test in space aiming for an uncertainty level of 10^{-15} [27]. Additionally, matter-wave interferometry with large momentum trans-

fer [28][14] and a large-scale facility allowing for second-level dark time are also expected to improve the uncertainty by several orders of magnitude.

In addition, dual atom interferometer is also a promising application for advancing the precision of this tests. In this kind of setup, two atom interferometers are simultaneously operated following identical sequences of light pulses. Simultaneous interferometers utilizing the superposition of two hyperfine ground states of rubidium have been implemented to conduct a quantum test of the equivalence principle [29]. A distinct benefit of dual atom interferometry lies in its ability to mitigate common mode noise factors like vibrations, as both interferometers share the same light pulse sequence. The major sources of systematic errors present in the previous works are introduced by the second-order Zeeman effect and AC Stark shits. This can be reduced or eliminated by conducting the dual atom interferometer based on clock transition in strontium atoms, which is one major work carried out in the dissertation.

Moreover, the combination of atom interferometry and atomic clocks holds potential for applications such as time dilation or gravitational redshift. The internal states separated by an energy $\hbar\omega$ embrace a mass difference $\Delta m = \hbar\omega/c^2$, which can be used for the probe of the Einstein's time dilation with a clock ticking at a angular frequency ω [30][31][32][33], c is the vacuum speed of light. Nevertheless, to achieve the general relativity tests, the sensitivity of the current interferometers shall be improved, which might be realized by implementing the atom interferometer with large-scale or large-momentum scheme [28][14][34]. The space missions projects have also been proposed and implemented to improve the sensitivity of the interferometry [35][27]. Additionally, it has been proposed that the clock needs to be activated during the interferometry sequence [31][32], which makes the atom interferometry sensitive to gravitational redshift effects.

1.2 Bosonic Strontium-88 Atom

Strontium (Sr), an alkaline-earth from group II, has garnered significant interest among various trapped cold atomic species. Diverse experimental platforms have been explored, ranging from quantum sensing and metrology [36][37][38] to quantum simulation of condensed matter physics problems with ultracold fermionic and bosonic gases [39][40][41]. Establishment of a stable experimental system for generating ultracold strontium source represents a necessary and basic aspect, and this is one of major works carried out in this thesis.

The low lying energy levels and electric dipole transitions of Sr are shown in Figure 1.1. With its two valence electrons structures, Sr exhibits several advantages to realize various experimental platforms. The dipole allowed transition $^1S_0 \rightarrow {}^1P_1$ provides a large scattering rate (linewidth of 32 MHz) and facilitates large momentum transfer, making it suitable for first stage magneto-optical trap (MOT), fluorescence imaging as well as atomic beam slower. The intercombination transition $^1S_0 \rightarrow {}^3P_1$ (linewidth of 7.5 kHz) is well-suited for narrow line cooling in a second MOT stage, enabling temperatures close to the recoil limit [42][43][44][45]. Another crucial transition is the doubly

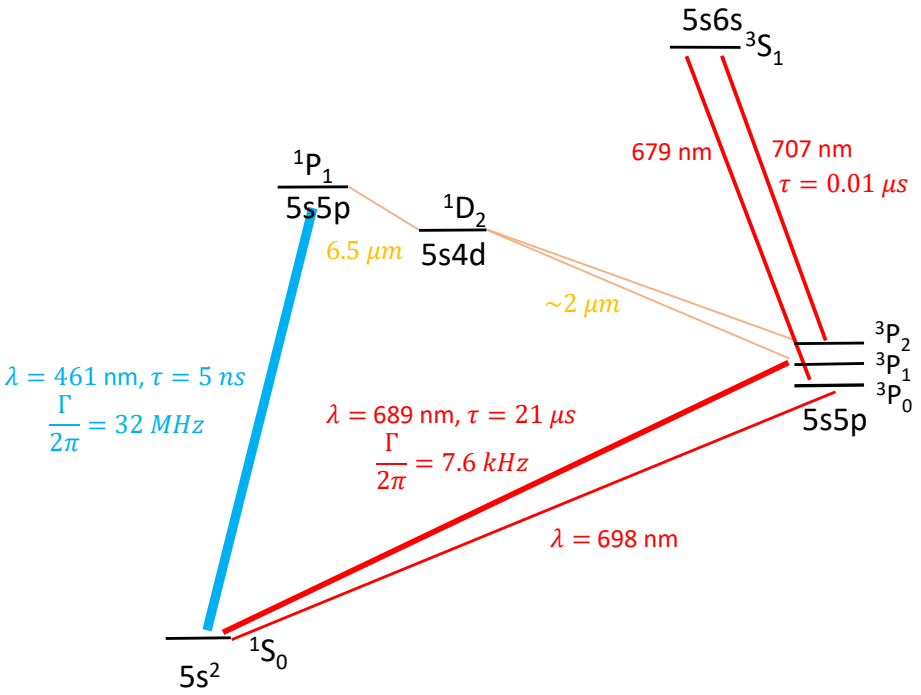

Figure 1.1: Strontium low lying energy levels and electric dipole transitions.

forbidden $^1S_0 \rightarrow {}^3P_0$ clock transition, weakly allowed in fermionic ^{87}Sr due to the hyperfine interaction through nuclear spins [46], whereas it can be magnetically induced in bosonic isotopes, where the nuclear spin is zero [47][48][49][50][51]. This ultranarrow clock transition is a promising candidate for a new frequency standard with redefinition of the second [52][53][54][55]. The clock transition is also useful for atom interferometers involving internal states with a large energy difference [56][57], quantum simulation of many-body spin-orbit coupling physics [58], nonequilibrium phenomena [59], and quantum computation [60][61][62].

Furthermore, the use of far-off resonant optical lattices at the magic-wavelength is extensively employed in the development of highly accurate atomic clocks [37][54], quantum simulation [63] and quantum computation [60], At the magic-wavelength, the ground and excited clock states embrace the same polarizability, resulting in an unchanged transition frequency and insensitivity to the lattice beam fluctuation and beam profile.

Isotope	Abundance (%)	Nuclear spin (I)	Statistics	Scattering length (a_0)
^{88}Sr	82.58	0	Bosonic	-2.00(27)
^{87}Sr	7.00	9/2	Fermionic	97.37(7)
^{86}Sr	9.86	0	Bosonic	798(12)
^{84}Sr	0.56	0	Bosonic	122.76(9)

Table 1.1: The stable isotopes of strontium. Taken from [4][5][6]

Table 1.1 lists the four stable isotopes of strontium along with their abundance, nuclear spin, statis-

tics and the scattering length of ground state $^1S_0$. In our atom interferometer system, we specifically opted for the bosonic isotope ^{88}Sr, which is the most abundant isotope. Due to its zero nuclear spin, the ground state (including the excited clock state $^3P_0$) exhibits insensitivity to the stray magnetic field [64], providing an advantage for inertial sensing. Moreover, as listed in the table, the s-wave scattering length of ^{88}Sr is $-2a_0$, and this weak value makes this isotope insensitive to the cold collisions.

Nevertheless, the challenge we are facing here with ^{88}Sr is that the clock transition is forbidden due to the selection rule, rendering the excitation of this transition with a single photon unfeasible. To address this limitation, the magnetically-induced spectroscopy has been proposed and tested [65][47][66]. This method involves the application of an additional magnetic field, termed the mixing field, to couple the states $^3P_0$ and $^3P_1$. Through this mechanism, the clock transition can be driven by a single probe laser beam operating at 698 nm. It is worth noting that in the magnetically-induced spectroscopy, a mixing field and probe beam can induce the second order Zeeman and AC Stark shifts.

1.3 Overview of this thesis

This thesis describes the establishment of an experimental setup for generating ultracold strontium-88 atomic samples and the implementation of dual atom interferometer based on the clock transition in ^{88}Sr. I begin by an overview of theoretical concepts relevant to this work, serving as a useful resource for both experimental conduct and result analysis. Next, I delve into the description of the experimental apparatus for the generation of ultracold strontium-88 atomic source. Following this, I proceed to discuss the preparation stage for the subsequent dual atom interferometer experiment. Finally, I detail the implementation and results of the dual atom interferometer,

The detailed organizational structure of the thesis is as follows:

- Chapter 2 provides the theoretical foundations for the experiment. It discusses the atom-light interaction, including the polarizability and coherent manipulation of the states. The derivation of phase accumulation in an atom interferometer is also presented, which is crucial for result interpretation.

- Chapter 3 presents the experimental setup for generating the ultracold strontium atomic source, including the vacuum system, laser system and magnetic field system. During the preparation of the atomic source, we implement a new scheme of hybrid bi-color atomic beam slower to enhance the atomic number in blue MOT. Additionally, an active feedback system for the magnetic field is constructed to compensate and control the stray field down to milli-gauss level.

- Chapter 4 describes the preparation stage for the quantum sensing. It includes the loading of the optical lattice, characterization of the clock transition, and Bragg diffraction with the prepared atoms. To obtain an atomic sample with low temperature, a velocity selection is also necessary before the atom interferometer phase, which is also described in this chapter.

- Chapter 5 presents the experimental results for the dual atom interferometer. We prepare the atomic sample in a statistical mixture of ground ($^1S_0$) and excited ($^3P_0$) clock states. This is followed by the implementatio of a Mach-Zehnder interferometer based on Bragg diffraction, which allows for the test of the weak equivalence principle. This dual atom interferometer scheme also enables the measurement of state-dependent forces, and this is demonstrated by applying an extra light field gradient provided by a 671 nm beam.

- Chapter 6 provides the conclusion and outlook of the main work in this thesis.

Chapter 2

Theory

2.1 Introduction

In this chapter, I provide a comprehensive overview of the theoretical foundations essential for conducting the experiment and interpreting the results. Section 2.2 outlines some of the theoretical treatment of the atom-light interactions. In section 2.2.1, the concept of polarizability is introduced, which plays a crucial role in the definition of magic-wavelength in strontium clock states. Section 2.2.2 introduces the dipolar force, resulting from the interaction between an atom and an external electromagnetic field, forming the theoretical foundation for laser trapping of atoms. Section 2.2.3 describes the resonant excitation of a two-level atom with an external field.

The pulses in our atom interferometer are generated by a moving lattice, known as the Bragg diffraction. In section 2.3, the theory behind Bragg diffraction is described. Section 2.3.1 introduces the model for single and double Bragg diffraction. Notably, Bragg pulses manipulate the momentum states of the atoms, making this resonant process highly sensitive to the initial velocities of the particles. In Section 2.3.2, we simulate the dynamics of the momentum states evolution considering the Doppler effect resulting from finite temperatures. This effect is a major limitation in our system.

In section 2.4, the theoretical background of the atom interferometer (AI) is introduced. The phase accumulation in the AI process is firstly calculated in section 2.4.1 and section 2.4.2. Based on this discussion, section 2.4.3 introduces the phase accumulation of Mach-Zehnder interferometer, which is implemented in our experiment.

2.2 Atom-Light interaction

2.2.1 Polarizability

Consider the atom in a monochromatic field with the form:

$$\begin{aligned}\vec{E}(\vec{r},t) &= \vec{E}(\vec{r})\cos(\omega t+\phi)\\ &= \frac{1}{2}\left[\vec{E}(\vec{r})e^{-i\phi}e^{-i\omega t}+\vec{E}(\vec{r})e^{i\phi}e^{i\omega t}\right]\\ &= \vec{E}^{(+)}(\vec{r})e^{-i\omega t}+\vec{E}^{(-)}(\vec{r})e^{i\omega t}\end{aligned} \tag{2.1}$$

where $\vec{E}^{(+)}$ and $\vec{E}^{(-)}$ are in front of the phase factor $e^{-i\omega t}$ and $e^{+i\omega t}$ respectively, which correspond to the positive- and negative frequency part. The force induced by the field on the electron is given by

$$\vec{F}^{(+)} = -e\vec{E}^{(+)} \tag{2.2}$$

Here, the dipole approximation is applied, where we assume the size of the atom is much smaller than the wavelength of the field such that the interaction between the electron and the field is defined at the nuclear position ($\vec{E}(\vec{r}) = \vec{E}(0)$). The equation of motion for the electron can be given by the Lorentzian damping model [67], which expresses a harmonic force interaction.

$$m\ddot{\vec{x}}^{(+)} + m\gamma\dot{\vec{x}}^{(+)} + m\omega_0^2\vec{x}^{(+)} = -\hat{\epsilon}eE_0^{(+)}e^{-i\omega t} \tag{2.3}$$

By solving the equation, the motion of the electron $\vec{x}$ in the field can be obtained. With this, the dipole moment induced by the field is $\vec{d} = -e\vec{x}$. Therefore, the polarizability $\alpha(\omega)$ can be defined as

$$\vec{d}^{(\pm)} = \alpha(\omega)\vec{E}^{(\pm)} \tag{2.4}$$

with the expression

$$\alpha(\omega) = \frac{e^2/m}{\omega_0^2-\omega^2-i\gamma\omega} \tag{2.5}$$

where γ is the damping rate in the Lorentzian model.

In general, since there are multiple resonances in one atom, we need to sum over all the resonances, which gives

$$\alpha(\omega) = \sum_i \frac{e^2}{m}\frac{f_i}{(\omega_{i0}^2-\omega^2-i\gamma_i\omega)} \tag{2.6}$$

The polarizability describes how the energy levels of the atoms change with the field.

Magic-wavelength

Based on the discussion regarding polarizability above, we can now introduce the definition and application of magic-wavelength [36][37]. The magic-wavelength represents the wavelength of a laser field at which two atomic states exhibit identical polarizability. Consequently, this ensures that the transition frequency remains unchanged. Figure 2.1 illustrates the polarizability of the ground $^1S_0$ and excited $^3P_0$ states of the clock transition in strontium atoms, where a magic-wavelength at 813.427 nm ($f_{\text{magic}} = 368554.58(28)$ GHz [68][69]) is observed.

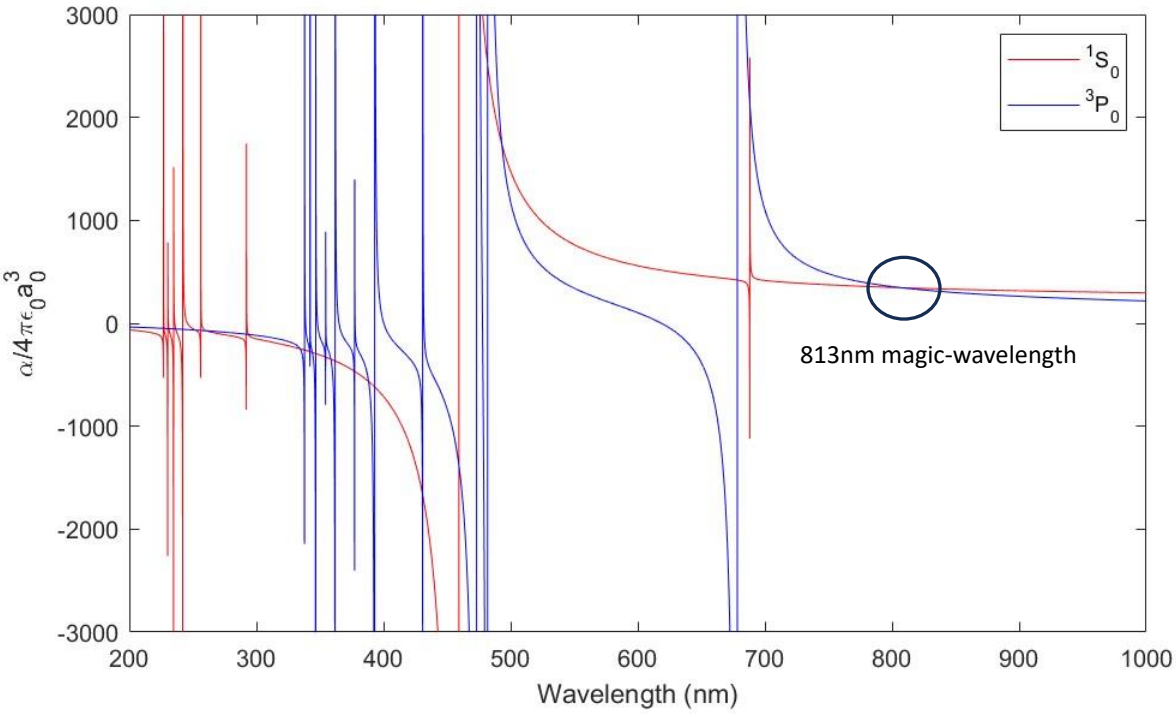

Figure 2.1: The polarizability for state $^1S_0$ and $^3P_0$ with the wavelength from 200 nm to 1000 nm. We highlight the point of intersection at 813.427 nm, which is an important magic-wavelength of the clock transition in strontium. The parameters used in the calculation is from [1]

Given that the laser profile and intensity fluctuations have no impact on the transition frequency between the two states, it becomes advantageous to construct the atomic clock within an optical lattice or tweezer array at the magic-wavelength [70][71][65]. In our experiment focusing on dual atom interferometer with ground and excited states of clock transition, we employ lasers operating at the magic-wavelength to create the optical lattice and the Bragg diffraction beam.

2.2.2 Dipole force

The potential induced by an external field can be given by

$$\begin{aligned} V_{\text{dipole}} &= -\frac{1}{2}\vec{d}\cdot\vec{E} \\ &= -\frac{1}{2}(\vec{d}^{(+)}+\vec{d}^{(-)})\cdot(\vec{E}^{(+)}+\vec{E}^{(-)}) \\ &= -\frac{1}{2}\left[\alpha(\omega)\vec{E}^{(+)|}\right]\cdot\vec{E}^{(-)} - \frac{1}{2}\left[\alpha(\omega)\vec{E}^{(-)|}\right]\cdot\vec{E}^{(+)} \\ &= -\frac{1}{2\epsilon_0 c}\text{Re}\left[\alpha(\omega)\right]I(\vec{r}) \end{aligned} \tag{2.7}$$

The anti-resonant terms at $\pm(\omega_0+\omega)$ are neglected here. Insert the expression of $\alpha(\omega)$ described in Section 2.2.1, the dipole potential can be rewritten as

$$V_{\text{dipole}} = -\frac{e^2}{2m\epsilon_0 c}\frac{\omega_0^2-\omega^2}{(\omega_0^2-\omega^2)^2+\gamma^2\omega^2}I(\vec{r}) \tag{2.8}$$

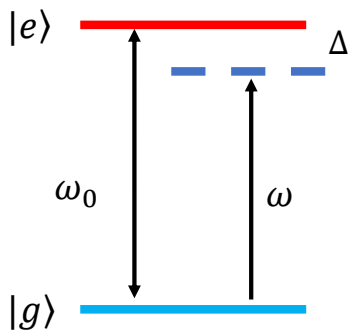

Figure 2.2: Two-level system interacting with a monochromatic field scheme, ω is the frequency of the field, ω_{eg} is the splitting between the ground and excited states, and $\Delta = \omega_0 - \omega$ is the detuning of the field.

With the dipole potential, the dipole force can be deduced by $\vec{F}_{\text{dipole}} = -\nabla V_{\text{dipole}}$, which indicates that the dipole force is proportional to the gradient of the intensity:

$$\vec{F}_{\text{dipole}} \propto \nabla I(\vec{r}) \tag{2.9}$$

With the presence of detuning $\Delta = \omega - \omega_0$, the dipole potential can be further expressed by

$$V_{\text{dipole}} = \frac{e^2}{2m\epsilon_0 c} \frac{(\omega_0 + \omega)\Delta}{[(\omega_0 + \omega)\Delta]^2 + \gamma^2\omega^2} I(\vec{r}) \tag{2.10}$$

Therefore, when $\omega > \omega_0$ ($\Delta > 0$), which is the so-called blue detuning, the dipole potential is positive and the dipole force pushes the atoms away from the brighter region of the optical field. In the case of $\omega < \omega_0$ ($\Delta < 0$), the dipole potential is negative, which means the atom is attracted by the high power region of the beam, and this is known as red detuning.

By utilizing the dipole potential discussed above, one can build up the optical dipole trap experimentally with a focused Gaussian laser beam in the red detuned condition. Additionally, the optical lattice can be achieved in a same way, which is formed by a pair of counter-propagating red-detuned beams. In our experimental system, we construct the optical lattice operating at the magic-wavelength of the clock transition in strontium-88. The detailed information about this is described in Section 4.2.

2.2.3 Atom excitation

Two-level system model

Coherent manipulation of the atoms with an external light field is crucial to describe the generation of superposition as well as the pulses during the atom interferometer. In this section, the useful expressions of the dynamics of atom-photon interaction are derived. We begin with a simple two-level case, and this can also be extended to Raman or Bragg transitions. A scheme of a two-level system splitted by ω_0 interacting with a monochromatic field with a frequency of ω is depicted in Figure 2.2.

The monochromatic plane-wave at $\vec{r} = 0$ can be expressed as

$$\vec{E}(0) = \hat{\epsilon} E_0 \cos(\omega t) \tag{2.11}$$

The internal part Hamiltonian of a two-level system is then given by

$$H = H_{atom} + H_{int}, \tag{2.12}$$

where H_{atom} is the Hamiltonian of the atom, and H_{int} describe the atom-field interaction:

$$\begin{aligned} H_{atom} &= E_e|e\rangle\langle e| + E_g|g\rangle\langle g| \\ H_{int} &= -\vec{d}\cdot\vec{E} = -(\vec{d}_{ge}\cdot\vec{E}|e\rangle\langle g| + h.c.) \end{aligned} \tag{2.13}$$

In the basis of $\{|e\rangle, |g\rangle\}$, the full matrix expression is given by

$$H = \begin{pmatrix} E_e & \hbar\Omega\cos(\omega t) \\ \hbar\Omega\cos(\omega t) & E_g \end{pmatrix} \tag{2.14}$$

where $\Omega = -E_0\hat{\epsilon}\cdot\vec{d}_{ge}/\hbar$ is the Rabi frequency; $\vec{d}_{ge}$ is the matrix element of the dipole operator with $d_{ge} = d^*_{eg}$ and Ω can be taken as real in the two-level system. In a two-level system, the state vector is given by

$$|\psi(\vec{r}, t)\rangle = e(t)e^{-iE_e t/\hbar}|\psi_e(\vec{r})\rangle + g(t)e^{-iE_g t/\hbar}|\psi_g(\vec{r})\rangle \tag{2.15}$$

By inserting it into the time-dependent Schrodinger equation and utilizing $\cos x = (e^{ix} + e^{-ix})/2$, we obtain

$$\begin{aligned} \dot{e} &= -i\frac{\Omega}{2}[e^{i(\omega_0+\omega)t} + e^{i(\omega_0-\omega)t}]g \\ \dot{g} &= -i\frac{\Omega}{2}[e^{-i(\omega_0-\omega)t} + e^{-i(\omega_0+\omega)t}]e \end{aligned} \tag{2.16}$$

where we introduce $\omega_0 = (E_e - E_g)/\hbar$. In the interaction scheme, we consider the case where $\omega_0 \simeq \omega$, which indicates that the terms with $e^{\pm i(\omega_0+\omega)}$ are rapidly oscillating and averaged to zero. This is known as the rotating-wave-approximation. The equations of evolution are then reduced to

$$\begin{aligned} \dot{e} &= -i\frac{\Omega}{2}e^{i(\omega_0-\omega)t}g \\ \dot{g} &= -i\frac{\Omega}{2}e^{-i(\omega_0-\omega)t}e \end{aligned} \tag{2.17}$$

By combining this two equations, we obtain

$$\ddot{e} - i\Delta\dot{e} + \frac{\Omega^2}{4}e = 0 \tag{2.18}$$

where $\Delta = \omega_0 - \omega$ is the detuning. We introduce the generalized Rabi frequency $\bar{\Omega} = \sqrt{\Omega^2 + \Delta^2}$, and the solutions of the equation above are calculated by

$$\begin{aligned} e(t) &= e^{i\Delta t/2}\left[e(0)\cos\left(\frac{1}{2}\bar{\Omega}t\right) + \frac{i}{\bar{\Omega}}[\Delta e(0) - \Omega g(0)]\sin\left(\frac{1}{2}\bar{\Omega}t\right)\right], \\ g(t) &= e^{i\Delta t/2}\left[g(0)\cos\left(\frac{1}{2}\bar{\Omega}t\right) - \frac{i}{\bar{\Omega}}[\Delta g(0) - \Omega e(0)]\sin\left(\frac{1}{2}\bar{\Omega}t\right)\right]. \end{aligned} \tag{2.19}$$

The equations above are the general solution for the population amplitudes of the two-level system.

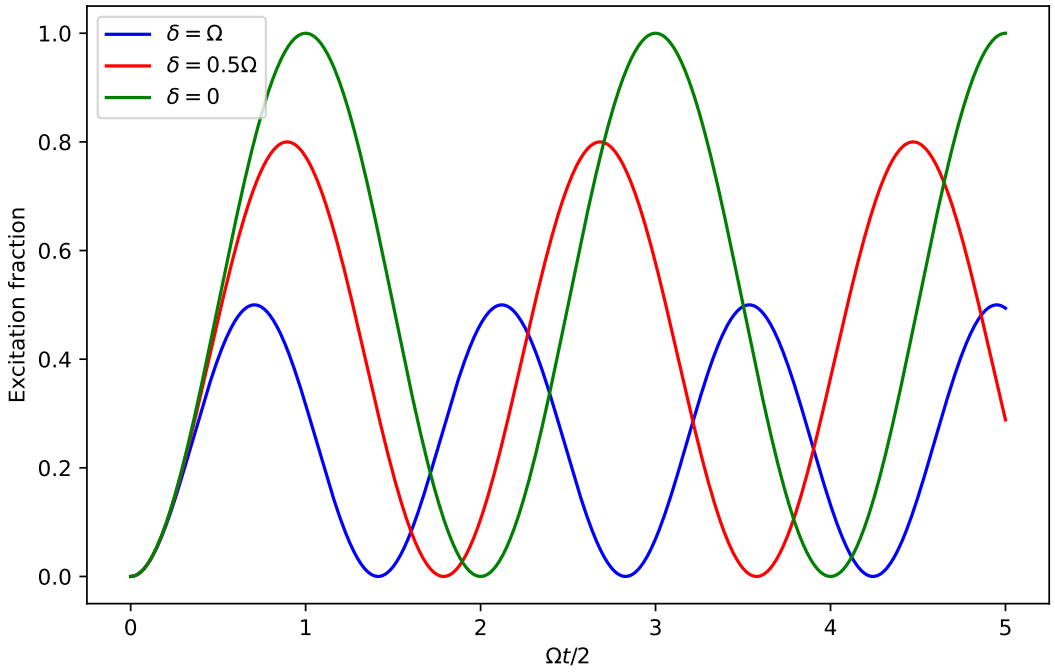

Figure 2.3: The dynamics of a two-level system interacting with a monochromatic field with various detuning.

Rabi Oscillation

We choose the initial condition to be at the ground state ($g(0) = 1$, $e(0) = 0$) and insert into the solutions above. This gives the probability to find the atom in excited state:

$$|e(t)|^2 = \frac{\Omega^2}{\bar{\Omega}^2} \sin^2\left(\frac{\bar{\Omega}}{2}t\right) \tag{2.20}$$

From the equation above, with $|e(t)|^2 + |g(t)|^2 = 1$, we can observe a population oscillation between the ground and excited states, which is known as the Rabi oscillation. The Rabi oscillations with various detunings are depicted in Figure 2.3, from which we can observe that the population is flopping between 0 to 1 on resonant case, while the transfer is not complete with non-zero detuning. Additionally, the oscillation is faster with a larger detuning.

π-pulse and $\pi/2$-pulse

In a resonance case ($\Delta = 0$), the period of one oscillation is given by $T = 2\pi/\Omega$. When the external field is turned on for a duration of $T/2 = \pi/\Omega$, an atom initially in one state undergoes a complete transition to the other state, known as a π-pulse. Furthermore, if the light field is turn on for $T/4 = \pi/(2\Omega)$, an atom initially in the ground state undergoes equal splitting, resulting in a superposition of ground and excited states, a phenomenon referred to as a $\pi/2$-pulse. In the atom interferometer stage, these π- and $\pi/2$-pulses are employed to coherently split and flip the two arms.

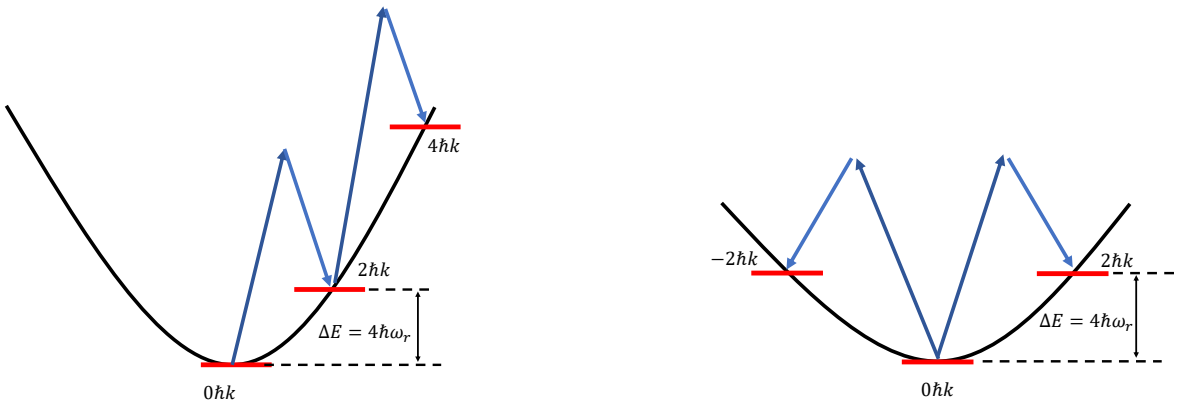

Figure 2.4: Single Bragg diffraction (left) and double Bragg diffraction (right).

2.3 Bragg Diffraction

In section 2.2.3, a simplified calculation about the interaction and dynamics of a two-level system in an external monochromatic field is discussed. Based on that, in this section, I introduce the theoretical model of the interaction between an atom and a moving lattice, referred to as Bragg diffraction. This process involves the manipulation of external momentum states of atoms. In our experiment, we utilize Bragg diffraction for velocity selection and as pulses in the atom interferometer.

2.3.1 Theoretical model

This section provides an overview of the theoretical model of single and double Bragg diffraction, as illustrated in Figure 2.4. Single Bragg diffraction describes the interaction between an atom and a moving lattice, leading to the flopping of the momentum states. This interaction can be treated as a two-level system in the theoretical model. In contrast, double Bragg diffraction involves the atom interacting with two moving lattices, inducing simultaneous transitions with opposite momentum transfer. In the model, this process is represented as a three-level system.

Single Bragg diffraction

Consider a two-level atom interacting with a moving lattice formed by a pair of counter-propagating beams with a frequency difference of δ:

$$\begin{aligned}\vec{E} &= E_0\hat{\epsilon}\cos\left[kz + (\omega + \delta/2)t\right] + E_0\hat{\epsilon}\cos\left[-kz + (\omega - \delta/2)t\right] \\ &= 2E_0\hat{\epsilon}\cos(\omega t)\cos(kz + \delta t/2)\end{aligned} \tag{2.21}$$

The total Hamiltonian of the system is given by

$$\hat{H} = \frac{p^2}{2m} + mgz + \hbar\omega_0|e\rangle\langle e| + \hat{H}_{int}, \tag{2.22}$$

which includes the kinetic energy, gravitational potential and atom-light interaction term with the energy diagram depends on $E_g = 0$. The interaction Hamiltonian reads

$$\begin{aligned}\hat{H}_{int} &= -\vec{d}\cdot\vec{E}|e\rangle\langle g| + h.c. \\ &= -\hbar\omega\left[e^{i\omega t} + e^{-i\omega t}\right]\cos(kz + \delta t/2)|e\rangle\langle g| + h.c.\end{aligned} \tag{2.23}$$

where $\Omega = dE/\hbar$ is the Rabi frequency. The total Hamiltonian in the rotating-wave approximation can be expressed by

$$\hat{H} = \frac{p^2}{2m} + mgz - \hbar\Delta|e\rangle\langle e| + \hbar\Omega_0|e\rangle\langle g|\cos(kz + \delta t/2) + h.c. \tag{2.24}$$

Here, Δ is the single-photon detuning.

Now, we make some assumptions according to the parameters we utilized in experiment, which can help us to put the system into a regime where the gravitational potential can be ignored. Firstly, we use the Bragg beams operating at 813.427 nm, which gives a recoil frequency of $\omega_R = \hbar k^2/(2m) = 2\pi\times 3.42$ kHz. The Bloch oscillation frequency can also be calculated as $\omega_B = mg\lambda/(2\hbar) = 2\pi\times 900$ Hz. This indicates the center-of-mass wavepacket will not deviate strongly with respect to $\lambda/2$, the period of the stationary wave. Additionally, during the experimental sequence, the frequency difference between the two counter-propagating beams is changing with the free-falling of the atomic cloud to maintain the resonance during the interaction. With these two conditions, the gravitational potential can be ignored.

The state vector of the atom is $|\psi(z,t)\rangle = g(z,t)|g\rangle + e(z,t)|e\rangle$. By inserting this into the time-dependent Schrodinger equation, we get

$$\begin{aligned}i\hbar\dot{g} &= -\frac{\hbar^2}{2m}\frac{\partial^2 g}{\partial z^2} + \hbar\Omega_0\cos(kz + \frac{\delta}{2}t)e \\ i\hbar\dot{e} &= -\frac{\hbar^2}{2m}\frac{\partial^2 e}{\partial z^2} - \hbar\Delta e + \hbar\Omega_0\cos(kz + \frac{\delta}{2}t)g\end{aligned} \tag{2.25}$$

The equations can be numerically solved, from which the dynamics of the population can be obtained.

Since the Bragg diffraction beams are usually far-detuned (Δ is large), the exited state follows the slow evolution of the ground state and can be adiabatically eliminated. This elimination gives us $e = (\Omega_0/\Delta)\cos(kz + \frac{\delta}{2}t)g$. With this, the Schrodinger equation reduces to

$$i\hbar\dot{g} = -\frac{\hbar^2}{2m}\frac{\partial^2 g}{\partial z^2} + \hbar\Omega\cos^2(kz + \delta t/2)g \tag{2.26}$$

where we have defined a two-photon Rabi frequency $\Omega = \Omega_0^2/(2\Delta)$. Eq. 2.26 can be used to perform the numerical simulation of the evolution dynamics in the system.

The periodic potential containing in Eq 2.26 is invariant under the translation of an integer multiple of $1/k$. With this, we can apply the Block theorem to separate the spatial-dependent term in $g(z,t)$ with quasimomentum:

$$g(z,t) = \sum_{l=-\infty}^{\infty} g_l(t)\exp(ilkz), \tag{2.27}$$

where the integer-index l corresponds to the state with momentum $l\hbar k$. Insert Eq 2.27 into the differential equation 2.26, we obtain

$$i\hbar \sum_{l=-\infty}^{\infty} \dot{g}_l e^{ilkz} = \hbar \sum_{l=-\infty}^{\infty} \left[(\omega_r l^2 + \Omega) g_l + \frac{\Omega}{2}(g_{l+2} + g_{l-2}) \right] e^{ilkz}, \tag{2.28}$$

where we have introduced the recoil frequency $\omega_r = \frac{\hbar k^2}{2m}$. The equation above holds only if for all the l:

$$i\hbar \dot{g}_l = \hbar \left(\omega_r l^2 + \Omega \right) g_l + \frac{\hbar\Omega}{2} \left(g_{l+2} + g_{l-2} \right) \tag{2.29}$$

The equation above indicates that either even or odd momentum states can be coupled.

In the case of a short interaction ($t \ll 1/\sqrt{\Omega\omega_r}$), the kinetic energy in Eq 2.29 can be neglected and it is reduced to

$$i\hbar \dot{g}_l = \frac{\hbar\Omega}{2} \left(g_{l+2} + g_{l-2} \right), \tag{2.30}$$

the solution of which can be expressed by [72]

$$g_{2l} = (-i)^l J_l(\Omega t), \tag{2.31}$$

where J_l is the l-th order Bessel function. Here we only focus on the states $2l$ since the equation only couples the states with a momentum separation of even number. With the solution given in Eq 2.31, the population of the states with momentum $2l\hbar k$ at time t can be expressed by $P_{2l}(t) = J_l^2(\Omega t)$. At $t = 0$, all the atoms are in the zero momentum state ($g_0 = 1$), whereas when $t \neq 0$, the populations are spreading out among many momentum states. In the case of very short interaction times, there are many momentum states populated, which is defined as the Raman-Nath regime. There are both proposals and experimental realizations reported to demonstrate multi-photon beam splitter via the Raman-Nath regime [73][74].

On the other hand, in the Bragg regime, the interaction time is long enough such that the intermediate states can be eliminated, leaving only two momentum states populated [75]. In the case of long interaction times, the kinetic energy term in Eq 2.26 cannot be neglected. Consider the atoms are initially in the momentum state $-n\hbar k$ ($g_{-n} = 1$), the Eq 2.26 gives a series of differential equations couple the states with the momentum separated by $2q$ (q is the integer number). The intermediate term is negligible if $\left|4q^2 - 4nq\right| \gg \hbar\omega$. With this, we can introduce the effective Rabi frequency as[72]

$$\Omega_{\text{eff}} = \frac{\Omega^n}{(8\omega_r)^{n-1}} \prod_{q=1}^{n-1} \frac{1}{nq - q^2} = \frac{\Omega^n}{(8\omega_r)^{n-1}} \frac{1}{(n-1)!^2}, \tag{2.32}$$

which describes the coupling between $-n\hbar k$ and $n\hbar k$. Based on the elimination, a series of the differential equations are reduced to

$$\begin{aligned} i\hbar g_{-n} &= \frac{\hbar\Omega_{\text{eff}}}{2} g_n \\ i\hbar g_n &= \frac{\hbar\Omega_{\text{eff}}}{2} g_{-n} \end{aligned} \tag{2.33}$$

The solutions of the equations are

$$\begin{aligned} g_{-n} &= \cos(\frac{\Omega_{\text{eff}} t}{2}) \\ g_n &= -i \sin(\frac{\Omega_{\text{eff}} t}{2}) \end{aligned} \tag{2.34}$$

Therefore, in the Bragg regime, the population of the momentum states are oscillating between $-n\hbar k$ and $n\hbar k$, which is analogy to the two-level Rabi oscillation discussed in section 2.2.3.

The intermediate regime between Raman-Nath and Bragg is called quasi-Bragg regime. In the quasi-Bragg regime, the elimination is not valid and the losses into other momentum states are not zero. In this case, the differential equations can be solved numerically with reasonable cutoffs [72]. The details of choosing the cutoff in our simulation are described in section 2.3.2.

Double Bragg diffraction

Based on the single Bragg diffraction, we now consider a three-level atom interacting with two moving lattice:

$$E_{1,2} = 2E_0\hat{\epsilon}\cos(\omega t)\cos(kz \pm \delta t/2) \tag{2.35}$$

The Hamiltonian of the system can be written as

$$H = -\frac{\hbar^2}{2m}\frac{\partial^2}{\partial z^2} + mgz - \hbar\Delta\sum_{i=1}^{2}|e_i\rangle\langle e_i| + \hbar\Omega[\cos(kz+\delta t/2)|e_1\rangle\langle g| + \cos(kz-\delta t/2)|e_2\rangle\langle g|] + h.c. \tag{2.36}$$

The state vector of the double Bragg diffraction system is $|\psi(z,t)\rangle = g(z,t)|g\rangle + e_1(z,t)|e_1\rangle + e_2(z,t)|e_2\rangle$. Analogous to Equation 2.25, the time-dependent Schrodinger equation gives:

$$\begin{aligned}
i\hbar\dot{g} &= -\frac{\hbar^2}{2m}\frac{\partial^2 g}{\partial z^2} + \hbar\Omega[\cos(kz+\frac{\delta}{2}t)e_1 + \cos(kz-\frac{\delta}{2}t)e_2] \\
i\hbar\dot{e_1} &= -\frac{\hbar^2}{2m}\frac{\partial^2 e_1}{\partial z^2} - \hbar\Delta e_1 + \hbar\Omega\cos(kz+\frac{\delta}{2}t)g \\
i\hbar\dot{e_2} &= -\frac{\hbar^2}{2m}\frac{\partial^2 e_1}{\partial z^2} - \hbar\Delta e_2 + \hbar\Omega\cos(kz-\frac{\delta}{2}t)g
\end{aligned} \tag{2.37}$$

Similar as single Bragg diffraction, by introducing the adiabatic eliminating, the Schrodinger equation is reduced to

$$i\hbar\dot{g} = -\frac{\hbar^2}{2m}\frac{\partial^2 g}{\partial z^2} + \hbar\Omega\left[\cos^2(kz+\delta t/2) + \cos^2(kz-\delta t/2)\right]g \tag{2.38}$$

Compared to Eq 2.26, there is an extra term expresses the coupling between g and another excited state. As I will discuss in section 2.3.2, the dynamics and population transfer can also be numerically simulated, which can be utilized as a guide to the experiment.

2.3.2 Sensitivity to temperature

In Bragg diffraction, the manipulation of the momentum states of the atomic sample indicates a high sensitivity of Rabi flopping efficiency to the initial velocity. This sensitivity is primarily due to the Doppler shift resulting from the finite temperature. Figure 2.5 provides a theoretical simulation depicting the population evolution with varying momentum distributions. The cutoff of the momentum states is set to $l = 5$, meaning the momentum Hilbert space has $2l+1$ dimensions during the calculation. Based on Eq 2.26 and Eq 2.38, we obtain a $(2l+1)\times(2l+1)$ Hamiltonian, and the dynamics for the evolution of the system can be simulated by numerically solving the Schrodinger equation.

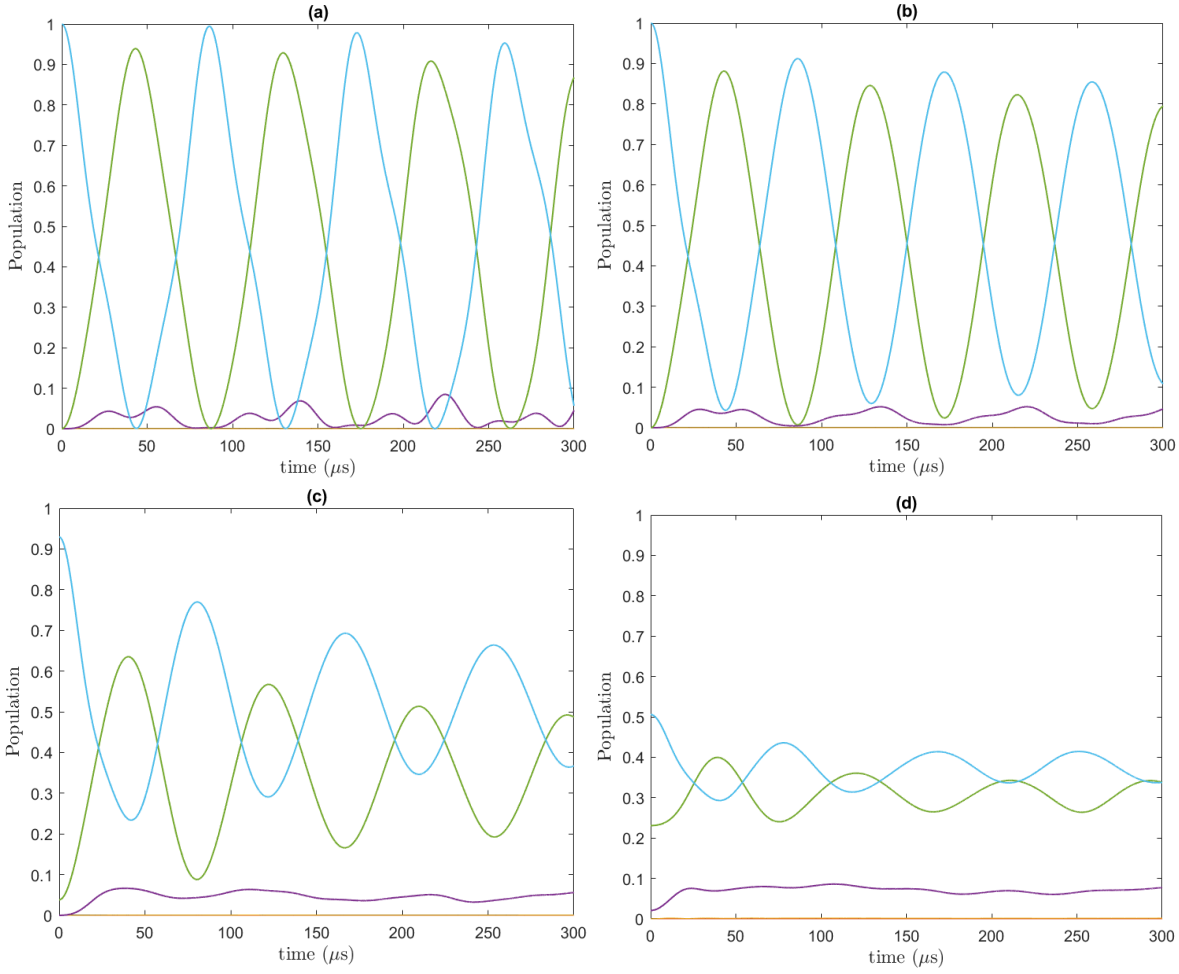

Figure 2.5: The dynamics of population oscillation for first order single Bragg diffraction with various initial temperatures. The blue, green and purple curves represent the population of $0\hbar k$, -$2\hbar k$ and -$4\hbar k$ respectively. (a) δ-momentum distribution; (b) $T = 0.06T_r$; (c) $T = 0.61T_r$; (d) $T = 4.28T_r$, where T_r is the recoil temperature.. The Rabi frequency used in the simulation is $\Omega = 3.5\omega_r$, and the frequency of the Bragg pulses is resonant to the transition from 0 to -$2\hbar k$ with zero-temperature.

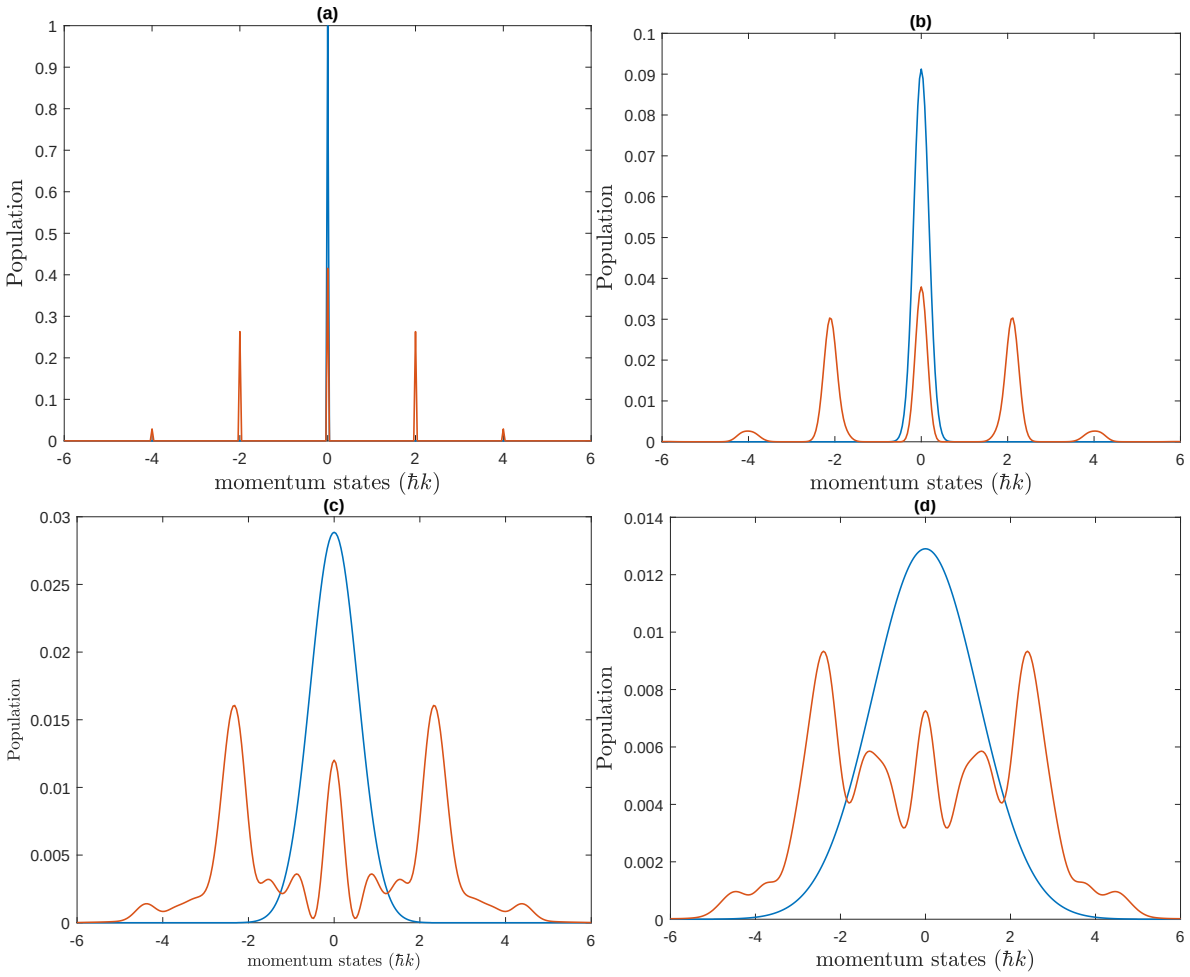

Figure 2.6: The momentum distribution of the system after a π-pulse of double Bragg diffraction with various atomic temperature. The blue and orange curves are the momentum distribution before and after the pulse. (a) δ-momentum distribution; (b) $T = 0.06T_r$; (c) $T = 0.61T_r$; (d) $T = 4.28T_r$. The Rabi frequency used in the simulation is $\Omega = 3.5\omega_r$, and the frequency of the Bragg pulses is resonant to the transition from 0 to $\pm 2\hbar k$ with zero-temperature.

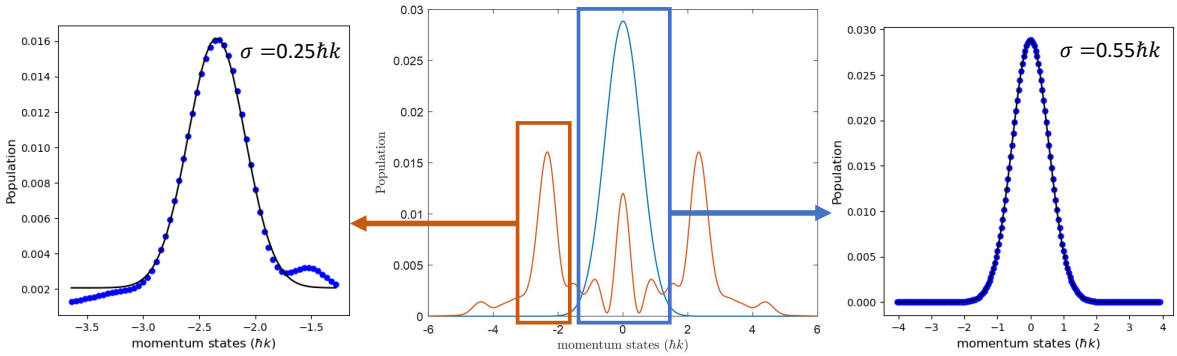

Figure 2.7: The momentum distribution before and after a double Bragg pulse, where parameters used is same as Figure 2.6(c). The momentum distributions around the 0-$\hbar k$ and $-2\hbar k$ are zoomed. The blue dots denote the simulation results, and the plained lines are the Gaussian fitting curve, which gives the width of the momentum distribution before and after the Bragg pulse.

Specifically, Figure 2.5(a) illustrates the dynamics of population amplitude with a δ-momentum distribution, while Figure 2.5(b), (c) and (d) depict the Rabi oscillation with a Gaussian momentum distribution with various cloud temperatures. A damping effects as well as a low flopping efficiency can be observed with finite temperature, which is attributed to the velocity sensitivity due to the Doppler shift in Bragg diffraction [76]. Besides, since the Doppler effect enhances the off-resonance transitions such as -2$\hbar k$ to -4$\hbar k$, the population in momentum state -4$\hbar k$ increases with higher temperature.

Additionally, Figure 2.6 illustrates the momentum distributions after a double Bragg diffraction pulse with various atomic temperatures. This numerical simulation employs a Rabi frequency of $3.5\omega_r$. In the case of δ-momentum distribution, the distribution remains δ-function-shaped after the pulse. The presence of $\pm$4-$\hbar k$ and 0-$\hbar k$ states results from the off-resonance transition during the double Bragg diffraction. With the Gaussian momentum distribution depicted in Figure 2.6 (b), (c) and (d), a reduction of the population in target states is observed. The Doppler shift also causes the presence of various momentum states, potentially posing limitations on data analysis using detection images.

The results shown in Figure 2.5 and 2.6 indicates that the Bragg diffraction is sensitive to the initial velocity of the atoms, so it is crucial to prepare a sample with narrow momentum distribution. It turns out that the Bragg pulses centered at the resonance frequency of zero-temperature can be utilized to narrow the momentum distribution. Figure 2.7 depicts the width of the momentum distribution before and after the Bragg pulse. Atoms with low temperature can be interrogated with the Bragg pulses and transferred to higher momentum states. The parameters used in the simulation is same as Figure 2.6 (c). The width of the momentum distribution is halved with the Bragg pulse. However, as shown in Figure 2.7, the fitting around the momentum distribution of -2$\hbar k$ gives the center of the distribution at -2.34$\hbar k$ due to the finite temperature.

2.4 atom interferometry

2.4.1 Overview of the phase accumulation

Similar as the optical interferometer, in an atom interferometer, the wave-packet of the atom is split coherently, going through different path and then recombined. The information will be encoded into the interferometry phase. Consider the two arms as states $|1\rangle$ and $|2\rangle$. In this two-dimensional Hilbert space, the rotation operator is given by

$$\begin{aligned}\hat{R}(\theta,\hat{\vec{n}}) &= \exp\left[i\vec{\sigma}\cdot\hat{\vec{n}}\,\frac{\theta}{2}\right] \\ &= \begin{pmatrix} \cos\frac{\theta}{2} - in_z\sin\frac{\theta}{2} & (-in_x - n_y)\sin\frac{\theta}{2} \\ (-in_x + n_y)\sin\frac{\theta}{2} & \cos\frac{\theta}{2} + in_z\sin\frac{\theta}{2} \end{pmatrix}\end{aligned} \tag{2.39}$$

where $\hat{\vec{\sigma}}$ is the Pauli matrix, and $\hat{\vec{n}}$ is the rotation direction. With this, the beamsplitter can be expressed by

$$\hat{S} = \hat{R}\left(\frac{\pi}{2}, -n_x\right) = \frac{1}{\sqrt{2}}\begin{pmatrix} 1 & i \\ i & 1 \end{pmatrix} \tag{2.40}$$

which is the specific case of the general rotation operator rotating the spinor by $\theta = \frac{\pi}{2}$ around -$\hat{x}$-axis. This beamsplitter $\hat{S}$ maps the state into an equal superposition of $|1\rangle$ and $|2\rangle$ from $|1\rangle$. During the free evolution stage, we suppose that the arms $|1\rangle$ and $|2\rangle$ acquire the phases ϕ_1 and ϕ_2 respectively. This process corresponds to the operator

$$\hat{U} = \begin{pmatrix} e^{i\phi_1} & 0 \\ 0 & e^{i\phi_1} \end{pmatrix} \tag{2.41}$$

The two arms are recombined after the evolution by applying the operator

$$\hat{S}^\dagger = \hat{R}\left(\frac{\pi}{2}, n_x\right) = \frac{1}{\sqrt{2}}\begin{pmatrix} 1 & -i \\ -i & 1 \end{pmatrix} \tag{2.42}$$

For the initial state $|\psi_i\rangle = |1\rangle = \begin{pmatrix} 1 \\ 0 \end{pmatrix}$, the output state $|\psi_f\rangle$ after this interferometer process is given by

$$\begin{aligned}|\phi_f\rangle &= \hat{S}^\dagger\hat{U}\hat{S}|\psi_i\rangle \\ &= \frac{1}{2}\begin{pmatrix} e^{i\phi_1} + e^{i\phi_2} \\ -i(e^{i\phi_1} - e^{i\phi_2}) \end{pmatrix}\end{aligned} \tag{2.43}$$

The probabilities for ending up with the states $|1\rangle$ and $|2\rangle$ are

$$\begin{aligned}P_1 &= \cos^2\left(\frac{\phi_2 - \phi_1}{2}\right) \\ P_2 &= \sin^2\left(\frac{\phi_2 - \phi_1}{2}\right)\end{aligned} \tag{2.44}$$

Therefore, in an output of the atom interferometer, the population of the states is oscillating between $|1\rangle$ and $|2\rangle$, which is dependent on the phase difference between the two arms. In section 2.4.2, the determination of the accumulated phase ϕ_1 and ϕ_2 will be described.

2.4.2 Phase accumulation in atom interferometer

In an atom interferometer, there are mainly three contributions for the total phase accumulation [77][78]:

$$\Delta\Phi = \phi_l + \phi_{\text{prop}} + \phi_{\text{sep}}, \tag{2.45}$$

The first term is the interaction phase acquired during the interrogation of atomic wave-packets in the light field. The second term expresses the interferometry phase accumulated on the propagation stage. The last term is the separation phase caused by the imperfection of the overlapping of the arms at the output of the interferometer, including the mismatch in position and velocity.

The phase induced by the interaction between atoms and light is the imprinted laser phase during the interrogation [77][78]:

$$\phi_l = \pm(kz - \omega t + \phi_0), \tag{2.46}$$

where ϕ_0 is the offset of the laser phase. The sign illustrates the process of the atom gets or loss momenta. With this, the interferometry phase due to the atom-light interaction can be calculated as the laser phase differences between the two arms:

$$\Delta\phi_l = \sum_{\text{arm1}} \pm\phi_l(z_i, t_i) - \sum_{\text{arm2}} \pm\phi_l(z_i, t_i), \tag{2.47}$$

where arm1 and arm2 represent the upper and lower arm respectively.

The propagation phase can be given by the action along the interferometry trajectory with consideration of the internal state [79][80][77]:

$$\phi_{\text{prop}} = S(q)/\hbar = \frac{1}{\hbar}\int_{t_i}^{t_f} (\mathcal{L} - E)\mathrm{d}t, \tag{2.48}$$

where $S(q)$ is the action along the trajectory q, E is the internal state energy of the atoms, $\mathcal{L}$ is the Lagrangian. In an atom interferometer based on Bragg diffraction, the internal state is unchanged, and the phase shift induced by the propagation is

$$\Delta\phi_{\text{prop}} = \frac{1}{\hbar}\sum_{\text{arm1}} S(q_i) - \frac{1}{\hbar}\sum_{\text{arm2}} S(q_i). \tag{2.49}$$

The third main contribution to the phase shift in atom interferometer is the separation phase, which is caused by the imperfection overlapping of the two wave-packets in position and velocity. This may happen with the existence of the force gradient, which displaces the arms by different values. The separation phase is given by [77], [78]:

$$\Delta\phi_{\text{sep}} = \bar{\mathbf{p}} \cdot \Delta\mathbf{z}, \tag{2.50}$$

where $\Delta\mathbf{z} = \mathbf{z}_u - \mathbf{z}_l$ is the position difference between the two arms, $\bar{\mathbf{p}}$ is the averaged classical momentum of the two arms at the output port of the interferometer.

2.4.3 Mach-Zehnder interferometer

With the formalism we discussed in section 2.4.2, we will calculate the phase accumulation in a $\pi/2$-T-π-T-$\pi/2$ Mach-Zehnder interferometer. From this we can explain how the atom interferometer can be used to implement the inertial sensing.

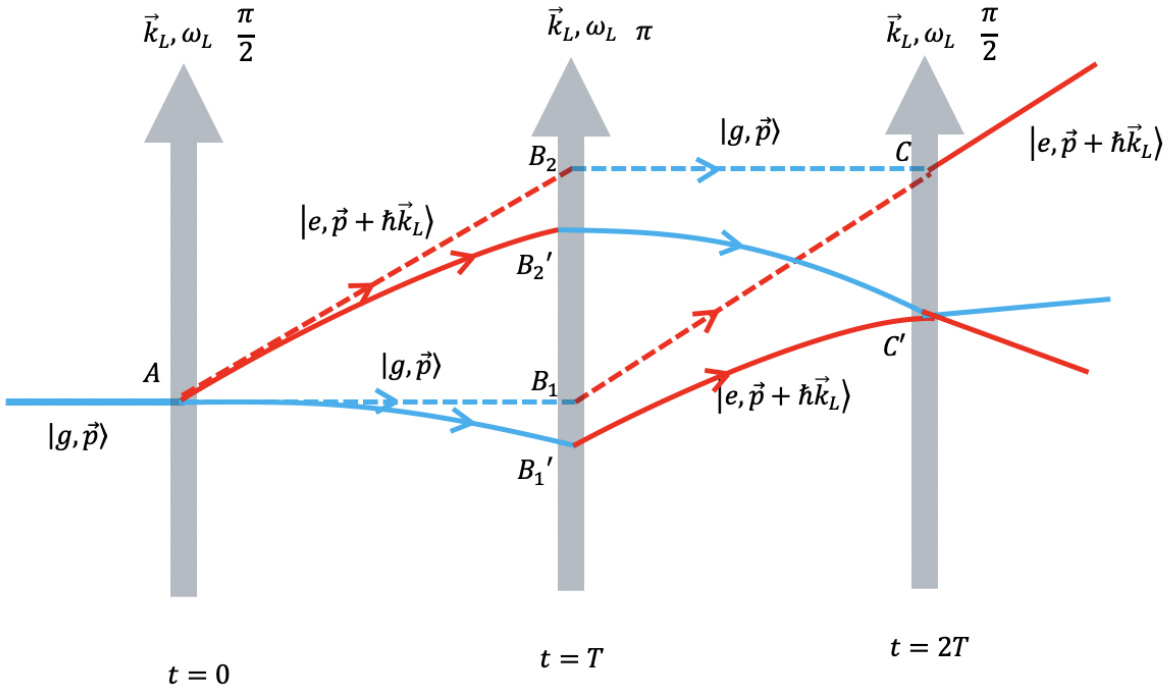

Figure 2.8: Time-space diagram of the Mach-Zehnder interferometer with (solid line) and without (dashed line) the presence of gravitational field.

The time-space diagram of the Mach-Zehnder interferometer is depicted in Figure 2.8, where the dashed line shows the trajectories of the two arms without the gravitational field, while the solid lines shows the paths with the presence of gravity. We first calculate the phase difference between the two arms accumulated during the free evolution stage. In the presence of gravitational field, the Lagrangian of a particle is given by

$$\mathcal{L}(\dot{z}, z) = \frac{M}{2}\dot{z}^2 - Mgz \tag{2.51}$$

From the Euler-Lagrange equation $\frac{\partial \mathcal{L}}{\partial z} - \frac{\mathrm{d}}{\mathrm{d}t}\frac{\partial \mathcal{L}}{\partial \dot{z}} = 0$, the classical path and final state can be derived as

$$\begin{aligned}
\dot{z}(t) &= \dot{z}_i - g(t - t_i) \\
z(t) &= z_i + \dot{z}_i(t - t_i) - \frac{1}{2}g(t - t_i)^2 \\
\dot{z}_f &= \dot{z}_i - g(t_f - t_i) \\
z_f &= z_i + \dot{z}_i(t_f - t_i) - \frac{1}{2}g(t_f - t_i)^2
\end{aligned} \tag{2.52}$$

where $(\dot{z}_i, z_i, t_i)$ and $(\dot{z}_f, z_f, t_f)$ denote the initial and final states of the particle. Also, we can express the initial velocity as

$$\dot{z}_i = \frac{z_f - z_i}{t_f - t_i} + \frac{1}{2}g(t_f - t_i) \tag{2.53}$$

The classical action is defined by the integration of $\mathcal{L}$ along the classical trajectory. Inserting the

expressions above, the classical action can be derived:

$$\begin{aligned} S_{\mathrm{cl}} &= \int_{t_i}^{t_f} \mathcal{L}(\dot{z}(t), z(t))\mathrm{d}t \\ &= \frac{M}{2}\frac{(z_f - z_i)^2}{t_f - t_i} - \frac{Mg}{2}(z_f + z_i)(t_f - t_i) - \frac{Mg^2}{24}(t_f - t_i)^3 \end{aligned} \tag{2.54}$$

With this, the phase difference between the two arms during the first dark time illustrated in Figure 2.8 is given by:

$$\begin{aligned} \hbar\Delta\phi_{prop1} &= S_{\mathrm{cl}}^{AB_2^{'}} - S_{\mathrm{cl}}^{AB_1^{'}} \\ &= \frac{M}{2T}\left[(z_{B_2^{'}} - z_A)^2 - (z_{B_1^{'}} - z_A)^2\right] - \frac{MgT}{2}\left[(z_{B_2^{'}} + z_A) - (z_{B_1^{'}} + z_A)\right] \\ &= \frac{M}{2T}(z_{B_2^{'}} - z_{B_1^{'}})(z_{B_2^{'}} + z_{B_1^{'}} - 2z_A - gT^2) \end{aligned} \tag{2.55}$$

Similarly, the phase difference during the second free evolution time:

$$\begin{aligned} \hbar\Delta\phi_{prop2} &= S_{\mathrm{cl}}^{B_2^{'}C^{'}} - S_{\mathrm{cl}}^{B_1^{'}C^{'}} \\ &= \frac{M}{2T}(z_{B_2^{'}} - z_{B_1^{'}})(z_{B_2^{'}} + z_{B_1^{'}} - 2z_{C^{'}} - gT^2) \end{aligned} \tag{2.56}$$

The total phase difference induced by the propagation of the particle is derived from

$$\begin{aligned} \hbar\Delta\phi_{prop} &= \hbar\Delta\phi_{prop1} + \hbar\Delta\phi_{prop2} = (S_{\mathrm{cl}}^{AB_2^{'}} - S_{\mathrm{cl}}^{AB_1^{'}}) + (S_{\mathrm{cl}}^{B_2^{'}C^{'}} - S_{\mathrm{cl}}^{B_1^{'}C^{'}}) \\ &= \frac{M}{T}(z_{B_2^{'}} - z_{B_1^{'}})((z_{B_2^{'}} + z_{B_1^{'}} - z_A - z_{C^{'}} - gT^2) \\ &= 0 \end{aligned} \tag{2.57}$$

Therefore, in Mach-Zehnder interferometer, the phase difference during the free evolution is zero.

Now we consider the phase difference due to the atom-light interaction during the pulses:

$$\Delta\phi_l = \sum_{AB_2^{'}} \phi_l - \sum_{AB_1^{'}} \phi_l \tag{2.58}$$

As illustrated in Figure 2.8, because of the free fall in gravitational field, the interactions take place at $B_1^{'}$, $B_2^{'}$ and $C^{'}$ instead of B_1, B_2 and C. The corresponding laser phase is scaled by the free falling distance during the dark time. From the discussion in section 2.4.2, the phase difference accumulated from the atom-light interaction based on Bragg diffraction can be calculated as

$$\phi_l = \pm(k_{\mathrm{eff}}z - \omega t_i + \phi_0) \tag{2.59}$$

Thus, the phase difference induced by the atom-light interaction is given by

$$\Delta\phi_l = k_{\mathrm{eff}}T^2 g + (\phi_{\mathrm{I}} - 2\phi_{\mathrm{II}} + \phi_{\mathrm{III}}), \tag{2.60}$$

where ϕ_{I}, ϕ_{II} and ϕ_{III} denote the optical phase for three pulses respectively.

The separation phase in a Mach-Zehnder interferometer is ideally zero with $\Delta\mathbf{z} = 0$ in a uniform field, Therefore, in a Mach-Zehnder interferometer, the phase of interference fringes is accumulated during the atom-light interaction stage. The laser can be regarded as a ruler, which can precisely

measure the free fall of the atomic sample in the laboratory frame, and the gravity g is encoded into the phase:

$$\Delta\Phi = \Delta\phi_l = k_{\text{eff}} T^2 g + (\phi_{\text{I}} - 2\phi_{\text{II}} + \phi_{\text{III}}). \tag{2.61}$$

This can be understood by considering the laser as a ruler in the Mach-Zehnder interferometer. Its phase reflects the free-falling information of the atomic sample, enabling the measurement of gravity.

2.5 Conclusion

In this Chapter, I have discussed the relevant theory of the atom-light interaction and atom interferometry. I initiate the discussion by introducing the theoretical foundations of polarizability, a concept critical to the magic-wavelength phenomenon. In our experiment, both the optical lattice and Bragg beams operate at a wavelength of 813.427 nm, corresponding to the magic-wavelength for the clock transition in strontium-88. Then the dynamics of a two-level atom in an external field is derived, with which the Rabi flopping as well as the pulses in atom interferometer are introduced. During the quantum sensing stage, we employ Bragg diffraction for the splitting and reflection of the atomic wave-packets. Theoretical models and considerations related to finite temperature were described. Lastly, I presented the calculation of phase accumulation in the atom interferometer for interpreting our experimental results.

Chapter 3

The ultra-cold ^{88}Sr atomic source

3.1 Introduction

Before conducting the quantum sensing experiment, we established from scratch a new ultra-cold apparatus that I will discuss in detail in this chapter. In Section 3.2, a comprehensive overview of the experimental setup is provided, encompassing the design of vacuum chamber, breadboards and coils surrounding the chamber. This section further delves into detailing the specifications of lasers and magnetic fields utilized throughout the process of preparing the ultra-cold atomic sample and implementing the dual atom interferometer. The subsequent sections, 3.3 and 3.4, outline the procedures for creating an ultra-cold ^{88}Sr atomic source. These processes primarily entail two key components: the production of a cold atomic beam and the creation of the atomic source. The atomic beam is obtained from an innovative design incorporating a bi-color atomic beam slower and a 2D MOT setup. Following the preparation of the atomic beam, a 461 nm push beam is utilized to push the atoms into the science chamber. In the science chamber, we implement a 461 nm MOT, followed by a 689 nm MOT to finalize the preparation of ultra-cold atomic source, as elucidated in Section 3.4.

3.2 Overview of the experimental system

3.2.1 Vacuum chamber

We designed a dual vacuum chamber setup, inspired by the literature references [81, 82, 83]. The vacuum system comprises two integral sections: an atomic beam production part and an ultra-high vacuum (UHV) science chamber. The sketch of the chamber is depicted in Figure 3.1. The UHV science chamber and atomic beam stage are connected along the y-axis, separated by a 23-cm-long differential pumping tube with 2 mm inner diameter, which facilitates a sufficiently-low conduction to the science chamber. A gate valve is strategically positioned between the atomic beam source and the UHV science chamber, enabling the isolation of the two sections when required. Atoms that are cooled in the 2D-MOT are pushed towards the science chamber using a weak (0.06 mW) 461 nm resonant

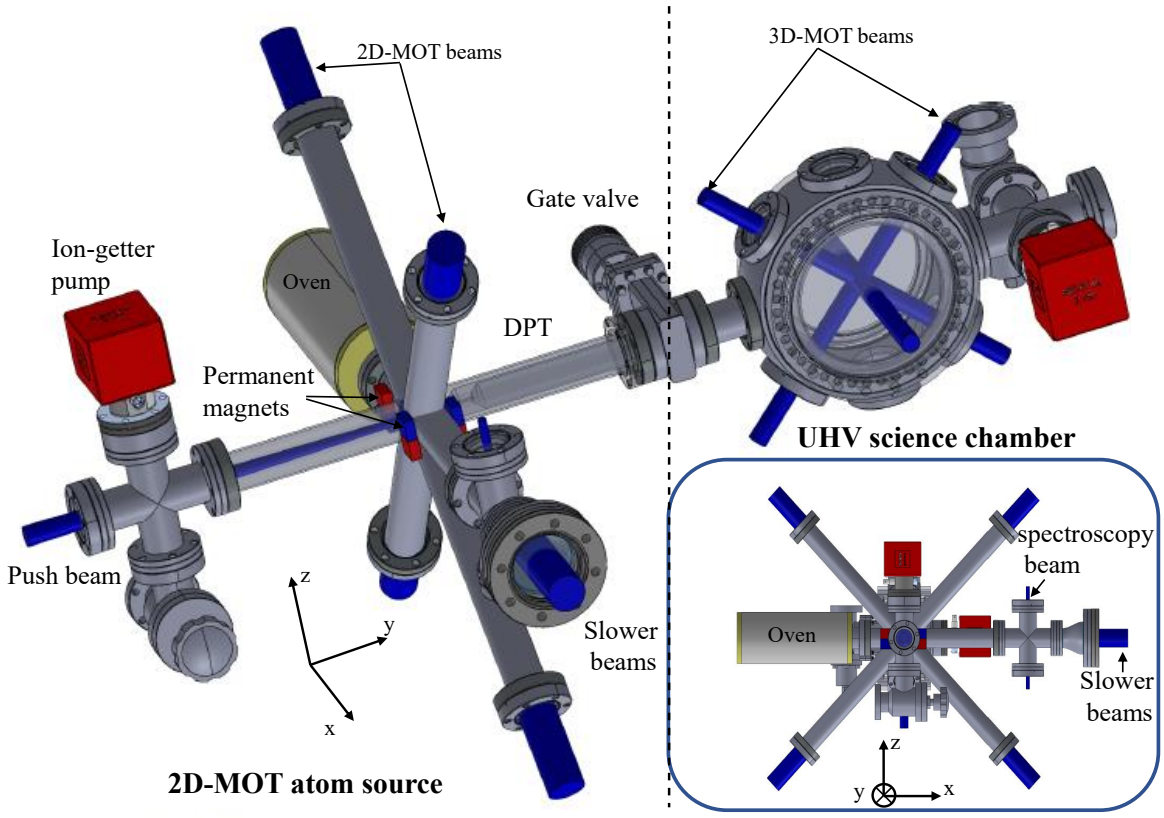

Figure 3.1: A three-dimensional drawing of the experimental setup. The setup consists of two main parts, a 2D-MOT atomic beam source and a UHV science chamber, which are separated by a gate valve and a differential pumping tube (DPT). Four stacks of permanent magnets, color-coded blue and red to indicate the polarity, are arranged around the center of the 2D-MOT chamber to provide the magnetic field needed for both the 2D-MOT and Zeeman slower. The blue cylinders in the drawing represent the 461 nm laser beams used for 2D-MOT, 3D-MOT, bi-color slowing, pushing and spectroscopic reference. The bottom right figure shows an alternative view of the setup along the push beam direction.

push beam, imparting a longitudinal velocity of approximately 15 m/s. The push beam is slightly focused at the 2D-MOT position and defocused at the 3D-MOT location to minimize its mechanical impact on the cold atoms in the 461 nm-MOT.

Both the atoms source and the science chamber on either side of the differential pumping tube are pumped by hybrid getter-ion pumps, which provide the pressure down to 10^{-11} mbar level on science chamber side. This is adequate for our quantum sensing experiment sequence.

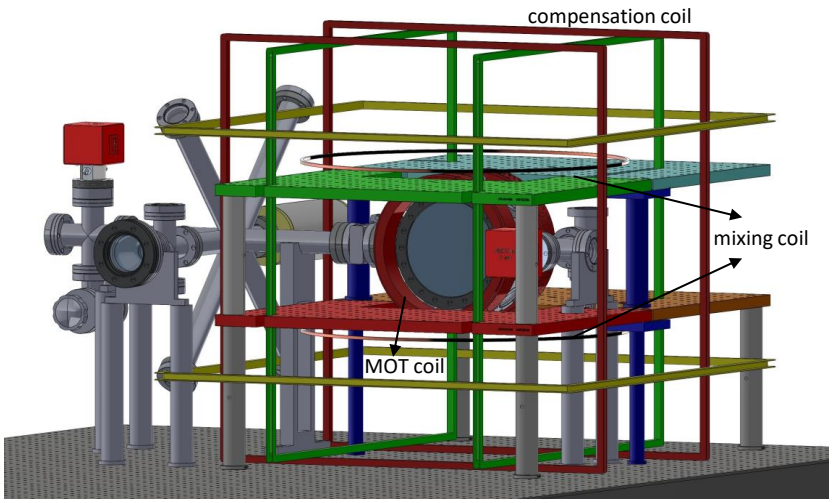

Figure 3.2: The breadboards and coil frame surrounding the science chamber. Four customized breadboards are positioned surrounding the UHV chamber to facilitate the arrangement of optical elements, mixing and compensation coil systems. Three pairs of Helmholtz coils are installed around the chamber to compensate the stray magnetic field. MOT coils are attached to the 8-inch viewports to create magnetic field gradients for the preparation of ultracold atomic source. Moreover, a pair of Helmholtz coils is mounted on the breadbords to provide the mixing field for the clock transition.

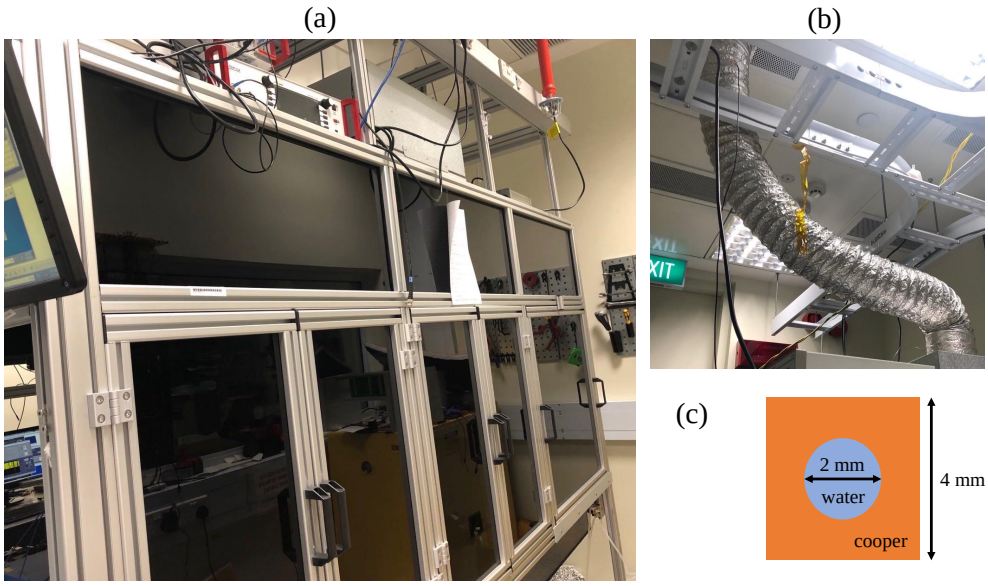

Figure 3.3: (a) The optical table enclosure with two HEPA filters on the top to avoid dust and stray light in the lab. (b) Aluminium tube with the heating wires inside. The tube connects the HEPA filters and air con, which can be used to stabilize the temperature inside the enclosure. (c) The cross section of MOT coil, where hollow core copper wire design is used to improve the efficiency of cooling.

3.2.2 Breadboards, magnetic coil frames and enclosure system surrounding the chamber

The setup incorporates four bespoke Aluminium breadboards strategically positioned around the science chamber, as depicted in Figure 3.2, designated for mounting optical elements and magnetic coil systems. To mitigate the effects of dust and stray light in the laboratory environment, an optical table enclosure equipped with two HEPA filters is installed. These HEPA filters are linked to an air conditioner via an aluminum tube, and the inclusion of heating wire winding within the tube allows for temperature stabilization inside the enclosure, as shown in Figure 3.3 (a) and (b).

There are three magnetic field systems surrounding the science chamber: the compensation, MOT and mixing coils. The compensation coil system comprises three pairs of square quasi-Helmholtz coils strategically positioned around the ultracold atomic cloud to actively compensate stray magnetic fields during the experiment, as depicted in Figure 3.2. Further details concerning this system are discussed in Section 3.5. The MOT coils, consisting of a pair of anti-Helmholtz coils, are mounted on the 8-inch viewports of the science chamber,generating a magnetic field gradient of 50 G/cm with a current of approximately 110 A. This is the typical gradient used for the 461 nm-MOT. To enhance the water cooling efficiency of the MOT coil, squared hollow core wire with dimensions of 4mm side length and 2mm inner diameter is utilized, as depicted in Figure 3.3(c), enabling the maintenance of a temperature below 33°C. Further information on the MOT coil circuit design is provided in Section 3.4.1. Another pair of Helmholtz coils, mounted on the breadboards is the mixing coil, which is essential for enabling the clock transition on bosonic strontium-88. To ensure a uniform mixing field with the Helmholtz configuration, we design the mixing coil with a radius of 272.75 mm. During the clock transition interrogation, the mixing coil is activated to generate a magnetic field of approximately 80 G, employing a typical current of 105 A. An overview of the fully ensembled system is depicted in Figure 3.4, and schematic block diagram featuring the key components in the experimental setup is presented in Figure 3.5.

3.2.3 Parameters in experiment

3.2.3.1 Parameters of lasers in the experiment

The laser beams required for the experiment, alongside their specifications, are outlined in Table 3.1. During the atomic source stage, the 2D MOT beam is split into two parts, collimated, and guided along the cross illustrated in Figure 3.1. These beams are then retro-reflected to transversely load the atoms into the 2D-MOT relative to the direction of the hot atomic beam. A pair of blue beams with two frequencies and cross-polarization are collimated and sent in the opposing direction to the hot atomic beam, constituting a bi-color atomic beam slower crucial for enhancing the 2D-MOT loading. The push beam with low power ($\sim$ 60 μW) and zero-detuning is slightly focused at the 2D-MOT position to push the atoms towards the science chamber. On the science chamber side, a 461 nm blue beam is split into six segments and overlapped with red laser beams (689 nm, 707 nm and 679 nm)

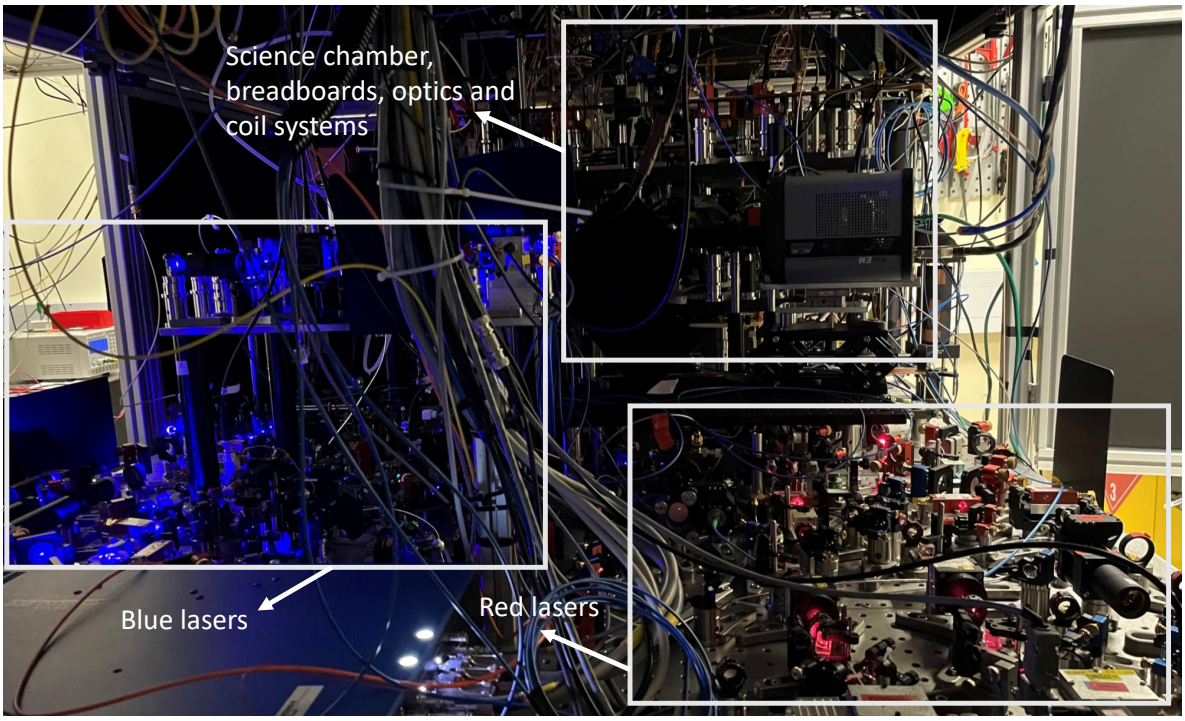

Figure 3.4: Fully ensembled system.

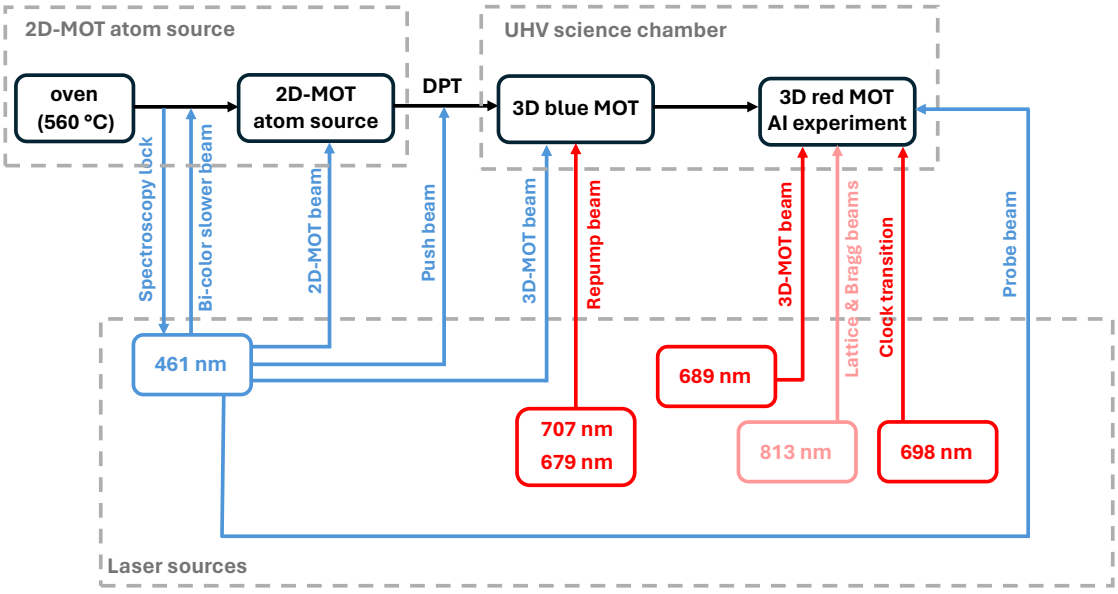

Figure 3.5: A block diagram summarizing the key components including the vacuum system and laser sources used in the experiment.

Laser beams required by the experiment						
Beam	λ (nm)	Transition	Detuning (MHz)	Beam waist	Total Power	Section
2D MOT	461	$^1S_0 \leftrightarrow {}^1P_1$	-28	10 mm	150 mW	3.3
Bi-color atomic beam slower	461	$^1S_0 \leftrightarrow {}^1P_1$	-180, -400	10 mm	160 mW	3.3
Push	461	$^1S_0 \leftrightarrow {}^1P_1$	0	0.5 mm	60 μW	3.3
3D blue MOT	461	$^1S_0 \leftrightarrow {}^1P_1$	-58	15 mm	220 mW	3.4
3D red MOT	689	$^1S_0 \leftrightarrow {}^3P_1$	-2.2 to -0.2	5 mm	14 to 1 mW	3.4
Repump	707	$^3P_2 \leftrightarrow {}^3S_1$	~ 0	5 mm	5.5 mW	3.4
Repump	679	$^3P_0 \leftrightarrow {}^3S_1$	~ 0	5 mm	1.8 mW	3.4
Probe	461	$^1S_0 \leftrightarrow {}^3P_1$	0	5 mm	30 mW	3.4
clock laser	698	$^1S_0 \leftrightarrow {}^3P_0$	0	100 μm	12 mW	4.3.1
Optical lattice	813.427	-	far detuned	80 μm	1 W	4.2.1
Bragg beams	813.427	-	far detuned	80 μm	250 mW	4.2.1

Table 3.1: Specifications of the laser beams required in the experiment.

to generate the ultra-cold atomic cloud. These beams are frequency-shifted and collimated to specific waist sizes with the particulars provided Table 3.1.

Subsequent to the preparation of the ultra-cold atomic cloud, two lattice lasers at magic-wavelength of clock transition are focused with a waist of 80 μm and applied in the horizontal and vertical directions, as depicted in Figure 3.6. Further details concerning the optical lattice are given in Section 4.2.1.

3.2.3.2 Parameters of magnetic field in the experiment

Magnetic field required by the experiment					
Magnetic field	Provided by	B (G)	Gradient (G/cm)	Direction	Section
Atomic beam slower	Permanent magnets	200 (peak)	-	x	3.3
2D MOT	Permanent magnets	0	45	xz-plane	3.3
461 nm MOT	MOT coil	0	50	x, y, z	3.4.1
689 nm MOT	MOT coil	0	0.7, 1.5	x, y, z	3.4.1
Mixing field	Mixing coil	80	0	z	4.3.2
Compensation field	Compensation coil	$\sim$1	0	x, y, z	3.5

Table 3.2: Specifications of the magnetic fields required in the experiment.

The the magnetic field values and their gradient are detailed in Table 3.2. The gradient of the magnetic field for the 2D MOT is produced by four sets of permanent magnets. Additionally, the

magnetic field tail serves as the source of magnetic field for the hybrid bi-color atomic beam slower. Further details are given in Section 3.3. In the science chamber, the 461 nm and 689 nm-MOT are implemented sequentially. The required magnetic fields are generated by a pair of MOT coils attached to the science chamber. The switching system for the MOT coils is illustrated in Section 3.4.1. Before progressing to the interferometer stage, a clock transition process is implemented to separate the atomic sample into ground and excited clock states, necessitating a mixing magnetic field to enable the transition in bosonic strontium-88. We build up a pair of Helmholtz coils attached on the breadboard to provide the mixing magnetic field, the details of which is introduced in Section 4.3.2. Additionally, three pairs of Helmholtz coils are strategically positioned along the $x-$, $y-$ and $z-$axes to actively compensate for the stray magnetic fields that could potentially impact the experiment. The structure and effectiveness of this compensation system are elaborated upon in Section 3.5.

3.2.4 Lasers alignment surrounding the vacuum chamber

The spatial configuration of lasers surrounding the science chamber is depicted in Figure 3.6. There are six MOT beams (three pairs) for both 461 nm and 689 nm as well as the repumpers overlapped for the generation of the 3D MOTs. One pair of MOT beams aligns horizontally, while the other two pairs are set at a 45° angle relative to the gravity axis. The details of this is discussed in Section 3.4.

We establish a 3D optical lattice operating at 813.427 nm in the system facilitate trapping and Bragg diffraction processes. Two of the lattices are on the horizontal plane and aligned at a 45° angle to the horizontal MOT beams. One horizontal lattice is overlapped with clock laser using a dichroic concave mirror. The vertical lattice serves as both lattice and Bragg beams, configured along the gravity direction. Detailed insights on the lattice configurations can be found in Section 4.2.

For experimental detection purposes, we utilize the fluorescence signal generated by a retro-reflected probe beam at 461 nm. The probe beam's frequency is finely tuned to resonance, saturating the transition $^1S_0 \rightarrow {}^1P_1$ (s=30s$_0$). Imaging is conducted in the horizontal plane at an approximate angle of 30° relative to the clock transition axis.

3.3 Cold atomic beam production stage

3.3.1 Oven: production of strontium atomic vapor

The cold atomic beam stage is composed of an oven, a compact Zeeman slower and a 2D-MOT. The oven is a customized CF40 flanged tube loaded with 19 g Strontium Granules ($\geq 99\%$). To minimize the atomic beam divergence, 900 nozzle tubes are put at the output of the oven. The nozzles are made of Monel 400 with the outer and inner diameter of 400 μm and 200 μm respectively, and the length of the nozzle tube is 0.9 mm [84]. Two heating wires are located at oven and nozzle to heat them separately: the temperature of the oven is kept at around 520 $°C$ while the nozzle is kept at higher temperature (around 560 $°C$) to avoid the deposit of strontium in the nozzle tubes. The whole oven

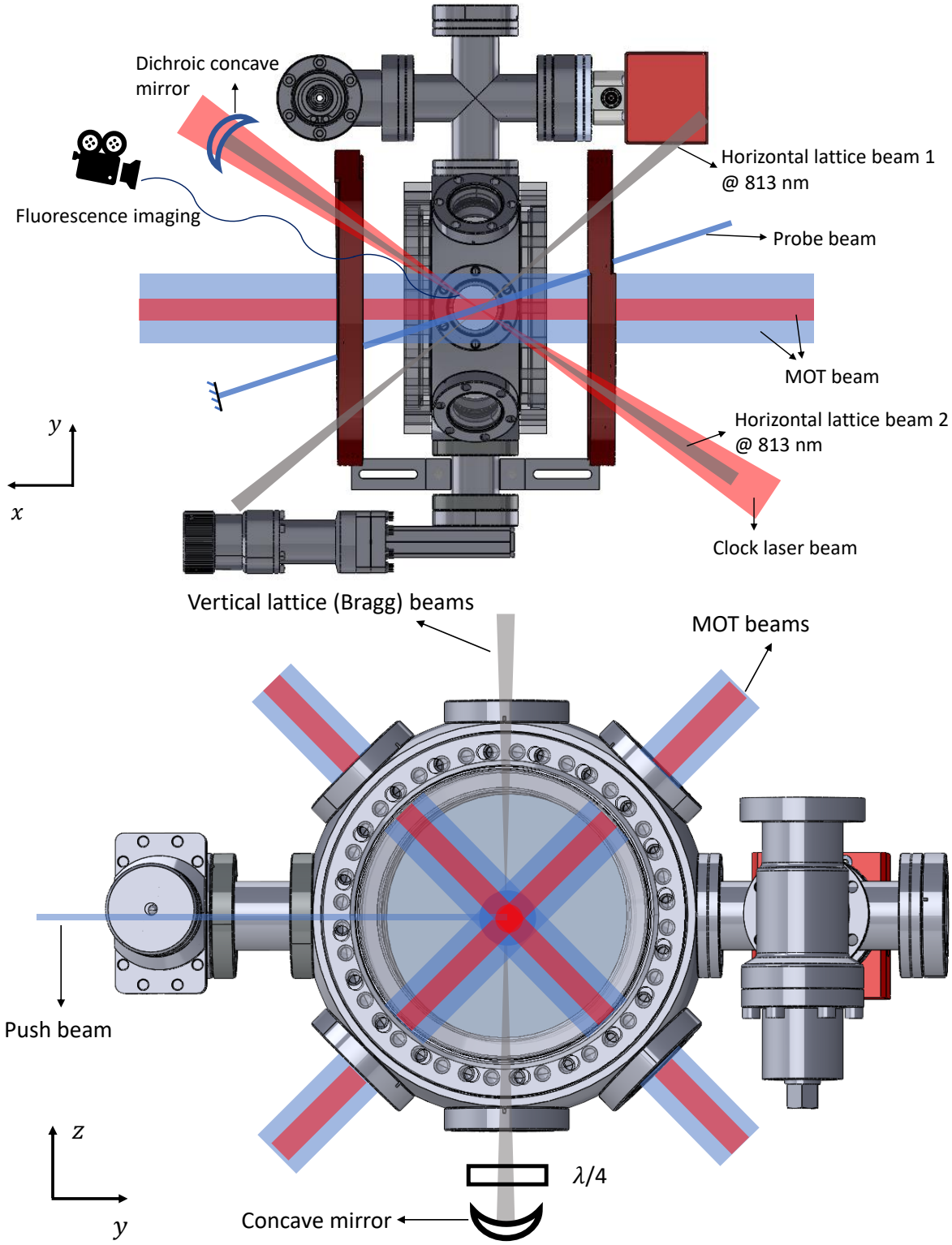

Figure 3.6: Overview of the lasers surrounding the science chamber. Top: vertical view. Bottom: horizontal view.

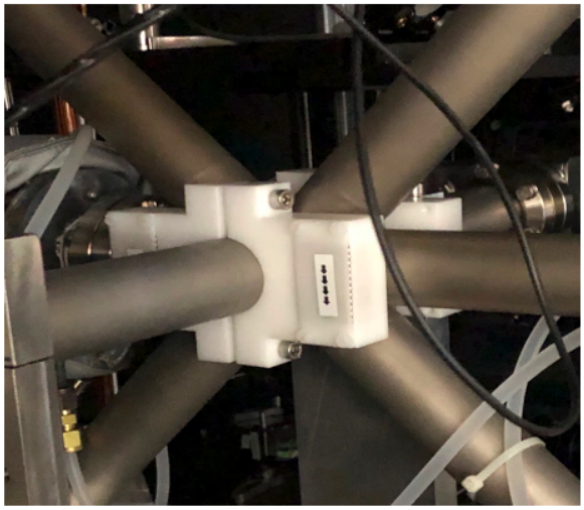

Figure 3.7: Arrangement of permanent magnets for 2D MOT and hybrid bi-color atomic beam slower.

setup is covered by a stainless steel cover, and glass fiber is filled between the cover and oven tube for the thermal isolation. Two cooper water-cooling disks are located at the connection side and back side of the oven to cool down the temperature of the flange and minimize the influence of other parts of the system.

After the strontium atomic effusive beam is extracted from the oven, the atoms are captured in a 2D MOT with the help of a hybrid bi-color atomic beam slower operating at 461 nm, targeting the fast transition of $^1S_0 \rightarrow {}^1P_1$. The free axis of the 2D MOT is along a transverse direction (y-axis) respect to the hot atomic beam, which makes the hot atomic source naturally away from a direct line of sight to the region where the experiments are carried out. The 2D quadrupole magnetic field used to trap the atoms in the xz-plane is produced by four stacks of NdFeB permanent magnets (N750-RB from Eclipse Magnetic Ltd.) arranged around the center of the eight-way cross (see Figure 3.7). This has been successfully implemented in Li [85], Na [81] and Sr [82, 83] in a hybrid configuration where the Zeeman slower and the 2D-MOT share the same magnets configuration, reducing the system size. The 2D MOT arms have a length of 30 cm to avoid the deposition of Sr atoms on the glass windows. The viewports for 2D MOT beams, push beam and spectroscopy are coated for 461 nm blue beam. The Sapphire window for slower beams is uncoated and is heated to $380°C$ to avoid the deposit of strontium from the oven.

3.3.2 461 nm Laser system

The layout of the 461 nm laser is depicted in Figure. 3.9. This blue laser addresses the dipole-allowed $^1S_0 \rightarrow {}^1P_1$ transition, which has a linewidth of $\Gamma_b/2\pi = 32\,\mathrm{MHz}$. This transition is fast enough to serve various functions like pushing, probing, and initial-stage cooling. Our laser source is a commercial system (Toptica TA-SHG pro 24231), generating the 461 nm blue laser through frequency doubling of a 922 nm master laser. The 922 nm master laser is generated using a grating-stabilized Anti-

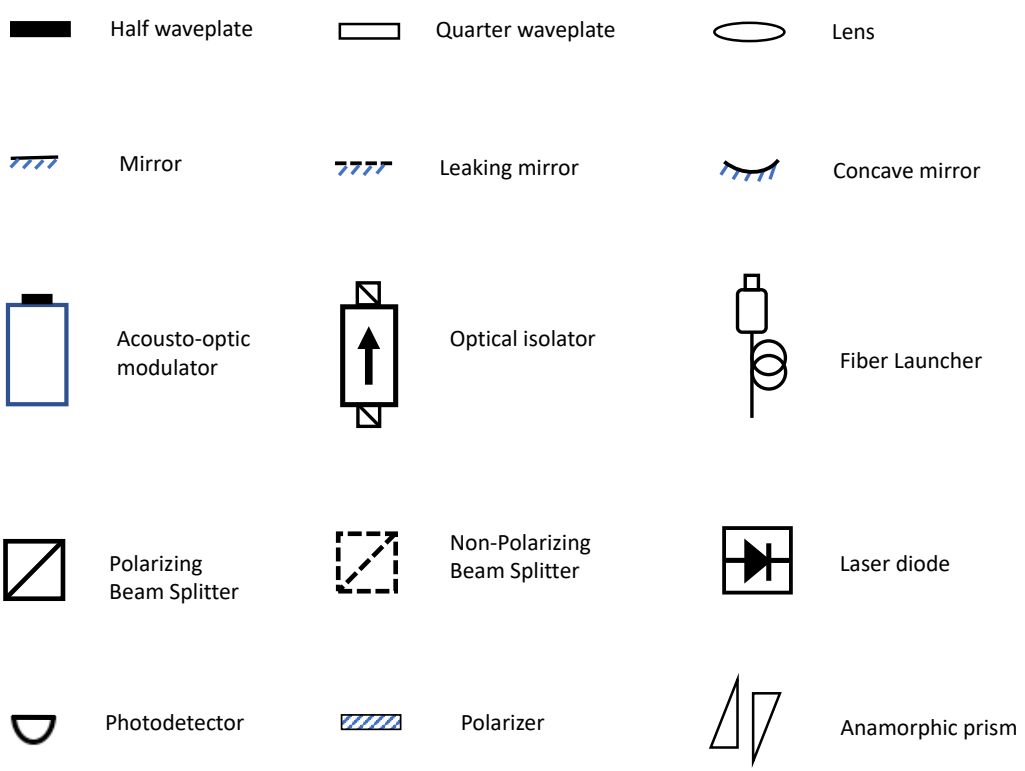

Figure 3.8: Symbols used in laser schematics.

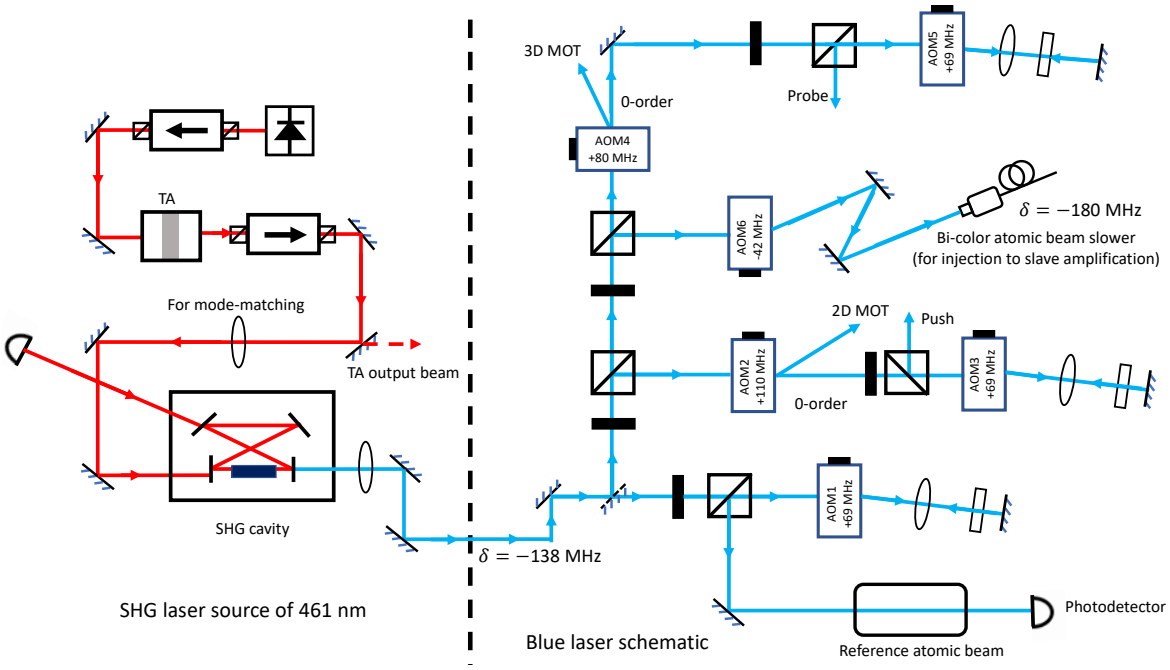

Figure 3.9: Schematics of 461 nm blue laser system. The main beam from the SHG source is split into 4 bunches by half-wave plates and PBS, which are used for frequency reference, 2D MOT beam, 3D MOT beam and master laser of bi-color atomic beam slower. The zero-order of 3D MOT and 2D beams are used for probe and push beams respectively. The symbols are defined in Figure 3.8.

Reflective (AR)-coated diode laser, further amplified by a tapered amplifier (TA) to achieve a power output of up to 1200 mW. After beam shaping, the master laser undergoes second-harmonic generation (SHG) within a cavity, producing the 461 nm laser with an output power of roughly 800 mW.

To lock the frequency of the master laser, a mirror with a leaked backwards is positioned after the output of the SHG source, as indicated in Figure 3.9. This configuration allows for obtaining a small amount of light to lock the master laser by sending it through the spectroscopy window depicted in Figure 3.1. The transmission signal is collected by a photodetector and sent into the PID module. The error signal is then sent to the piezoelectric transducer (PZT) of the master laser to lock the frequency of blue laser.

Subsequently, the light from the SHG 461 nm laser source is split into several bunches, appropriately frequency-shifted, and earmarked for distinct purposes including the 2D MOT, 3D MOT, push beam, probe beam, and the master laser of the bi-color atomic beam slower, depicted in Figure 3.9.

3.3.3 Hybrid bi-color atomic beam slower

To improve the performance of the cold atomic beam source, we send a pair of 461 nm laser beams, counter-propagating with the atomic beam produced by the oven, to perform a hybrid bi-color atomic beam slower on the $^1S_0 \rightarrow {}^1P_1$ transition of ^{88}Sr. The hybrid bi-color slowing scheme consists of a Zeeman slower that operates in combination with an additional beam that slows atoms via radiation pressure on the magnetically insensitive $m = 0 \rightarrow m = 0$ transition of the 461 nm line.

We first characterize the Zeeman slower of the hybrid scheme. The magnetic field profile from the permanent magnets along the x-axis, although not optimized for a standard Zeeman slower that keeps a constant radiation pressure force, it is still suitable to perform Zeeman slowing [82]. In the whole region of interest, the magnetic field direction is mainly along the z-axis, which is perpendicular to the atomic beam. Its magnitude is plotted in Fig. 3.10(a) as a function of d, the distance from the 2D-MOT center. We evaluate the performance of the slowing scheme by measuring the number of atoms trapped in the 461 nm MOT in the steady-state regime, which is achieved after 1.5 s of loading time. For a Zeeman slowing beam polarized along the y-axis, we find that the Zeeman slower reaches its peak efficiency at detunings of ~ -380 and ~ -30 MHz [see the blue curve in Fig. 3.10(b)]. Indeed, the horizontal linear polarization is decomposed into two circular polarization eigen-modes addressing the $m = 0 \rightarrow m = \pm 1$ transitions, respectively. Each circular polarization component is associated with a Zeeman slowing effect on one of the magnetic field slope regions. At large negative frequency detuning of ~ -380 MHz, we address the negative magnetic field slope [blue curve in Fig. 3.10(a)], where the large Doppler effect of atoms at the oven output is not compensated by a substantial Zeeman shift. In this case, we need a negative Zeeman shift corresponding to the $m = 0 \rightarrow m = -1$ transition. We end up with the opposite configuration on the positive slope [red curve in Fig. 3.10(a)]. Here, the deceleration starts with a large magnetic field bias and positive Zeeman shift to compensate for the larger positive Doppler shift of the Zeeman beam seen by the faster moving atoms. In previous works, only one of the frequencies is chosen to operate the Zeeman slower [85, 82]. Usually large negative

frequency detunings are favored to limit the mechanical action of the Zeeman beam on the 2D-MOT. We note also that the orientation of the magnetic field means that only 50% of the optical power is used for Zeeman slowing.

We now consider the slowing effect of a vertically polarized beam. In this case, the $m = 0 \rightarrow m = 0$ magnetic-insensitive transition is used to decelerate the atoms. The performance with respect to the laser frequency detuning is indicated as the green curve in Fig. 3.10(b). Using only the vertically polarized beam, the most effective slowing is achieved at a frequency detuning about -180 MHz.

By fixing the frequency of the vertically polarized beam at -180 MHz, we scan the frequency of the horizontally polarized beam with the same total power to obtain the red curve in Fig. 3.10(b). With this hybrid bi-color slowing scheme, we improve the overall number of atoms in the 461 nm MOT for a detuning of $\sim -400\,\mathrm{MHz}$, meaning slightly more red-detuned than the single-color Zeeman slower case. We obtain a total of $9{\times}10^8$ atoms in the 461 nm MOT. In addition, we note that the optimal number of atoms occurs on a broader slowing beam frequency range, leading to a slowing scheme that is more robust to potential frequency fluctuations.

The hybrid bi-color slowing scheme is optimized using two independent laser systems. However, thanks to the cross-polarization between the two beams, we are able to implement a single laser source with efficient use of the laser power for daily operations as shown in Fig. 3.11. We take 1.5 mW from the 461 nm laser source power to inject a 500 mW laser diode (Nichia, NDB4916). The seed laser beam used for injection locking is frequency shifted with an acousto-optic modulator (AOM) by -180 MHz from the resonance of the $^1\mathrm{S}_0 \rightarrow {}^1\mathrm{P}_1$ transition (AOM6 in Figure 3.9). The laser output from the slave laser passes through another AOM at 220 MHz to provide the two slowing beams required in the hybrid bi-color slowing scheme. The zero-order of the AOM at a detuning of -180 MHz is utilized to address the $m = 0 \rightarrow m = 0$ transition with the polarization parallel to the magnetic field; the minus-one-order at a detuning of -400 MHz is used to slow down the atoms via $m = 0 \rightarrow m = -1$ transition. The two diffraction orders of 0 and -1 are efficiently recombined using a polarizing beamsplitter (PBS). The overlapped collimated beams with a diameter of about 25 mm are sent through a sapphire viewport, onto the oven.

On Fig. 3.12 (a), we show the cold atoms number N as function of the slower total power P. When the optical beam is off, $N \sim 10^8$, indicating a substantial trapping efficiency of the bare atomic beam by the 2D-MOT. We note that, as expected, this value is also obtained with a far off-resonant slower (see green and blue data points in Fig. 3.10 for detuning beyond -500 MHz). For a slower total power above 140 mW, the performance of the bi-color slowing scheme saturates, so operating above this value gives a power-independent and optimum behavior. In practice, we use $P = 160$ mW to minimize the atoms number shot-to-shot fluctuations in the MOT due to the possible drift in the optical power and misalignment of the slowing beams. Additionally, the performance of the hybrid bi-color atomic beam slower is calibrated with different ratio of vertically polarized beam, which shows an optimal performance with the proportion $P_V/P = 0.5$ (P_V is the power of the beam with vertical polarization, and P is the total power). Also, the total power is divided equally between the two

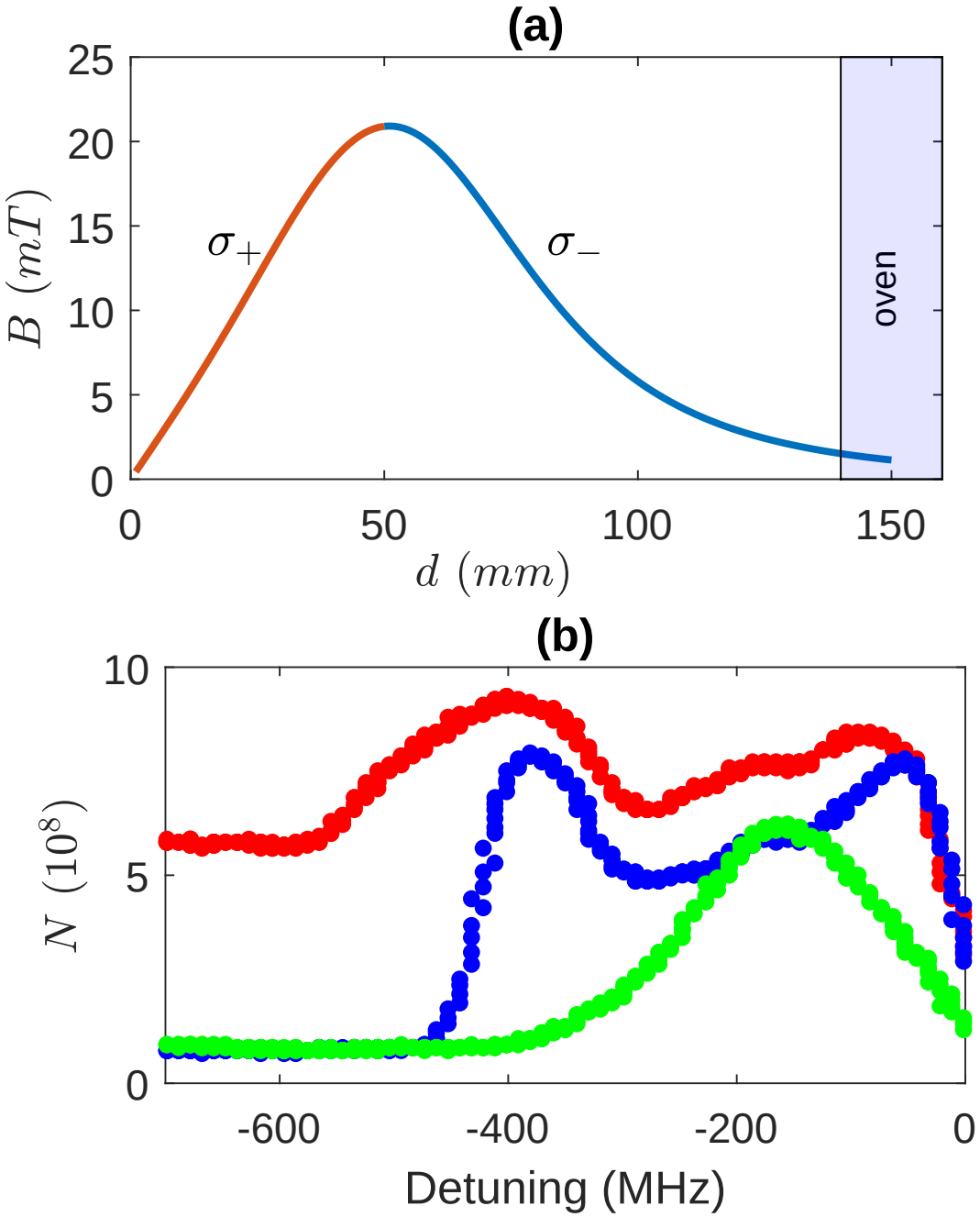

Figure 3.10: (a) Magnetic field B of the permanent magnets as a function of distance d from the 2D-MOT center along the x-axis. (b) Performance of the slowing scheme as measured by the total number of atoms N loaded in the steady-state 461 nm MOT. The blue curve is obtained with the Zeeman slowing beam only (horizontally polarized beam). The green curve shows the effect of slowing on the $m = 0 \rightarrow m = 0$ transition (vertically polarized beam). The red curve shows the performance of the hybrid scheme comprising both horizontally and vertically polarized beam. The vertically polarized beam is set to a frequency detuning of -180 MHz. In all cases, the total power is 160 mW. Figures are from [2].

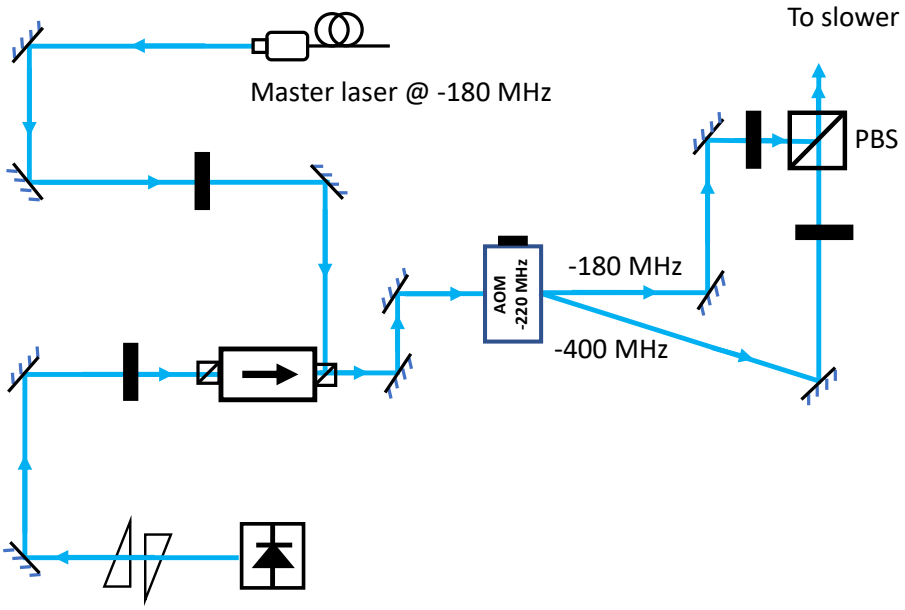

Figure 3.11: Optical setup to generate the two overlapped slowing beams for the hybrid bi-color slowing system. The symbols are given in Figure 3.8

polarization components. Overall, the bi-color slowing scheme enhances the atoms number by one order of magnitude leading to $N \sim 10^9$, a value similar to the current state-of-art setups [86], but obtained here with a more compact and simple system.

3.3.4 2D MOT

Upon emitting from the oven and being decelerated with the bi-color slower, the atomic beam is captured by the 2D MOT located at the center of the eight-way cross, as depicted in Figure 3.1.

The magnetic field gradient required for the 2D MOT is generated using permanent magnets, providing a gradient of 45 G/cm at the center of the cross, showcased in Figure 3.10. The 2D MOT beam comprises a pair of retro-reflected beams, frequency-shifted to the detuning of -58 MHz and collimated with a waist of 10 mm. To optimize the parameters utilized in 2D MOT, we conducted fluorescence signal analysis in the 3D 461nm-MOT while varying the intensity of 2D MOT beam. Based on the data shown in Figure 3.13, the number of atoms captured in 3D 461nm-MOT saturates at around 35 mW/cm^2, a proximity to the saturation intensity (I_0=42 mW/cm^2). Additionally, Figure 3.14 showcases the pictures of the 2D cold atomic beam viewed from the push beam window and atomic beam slower window.

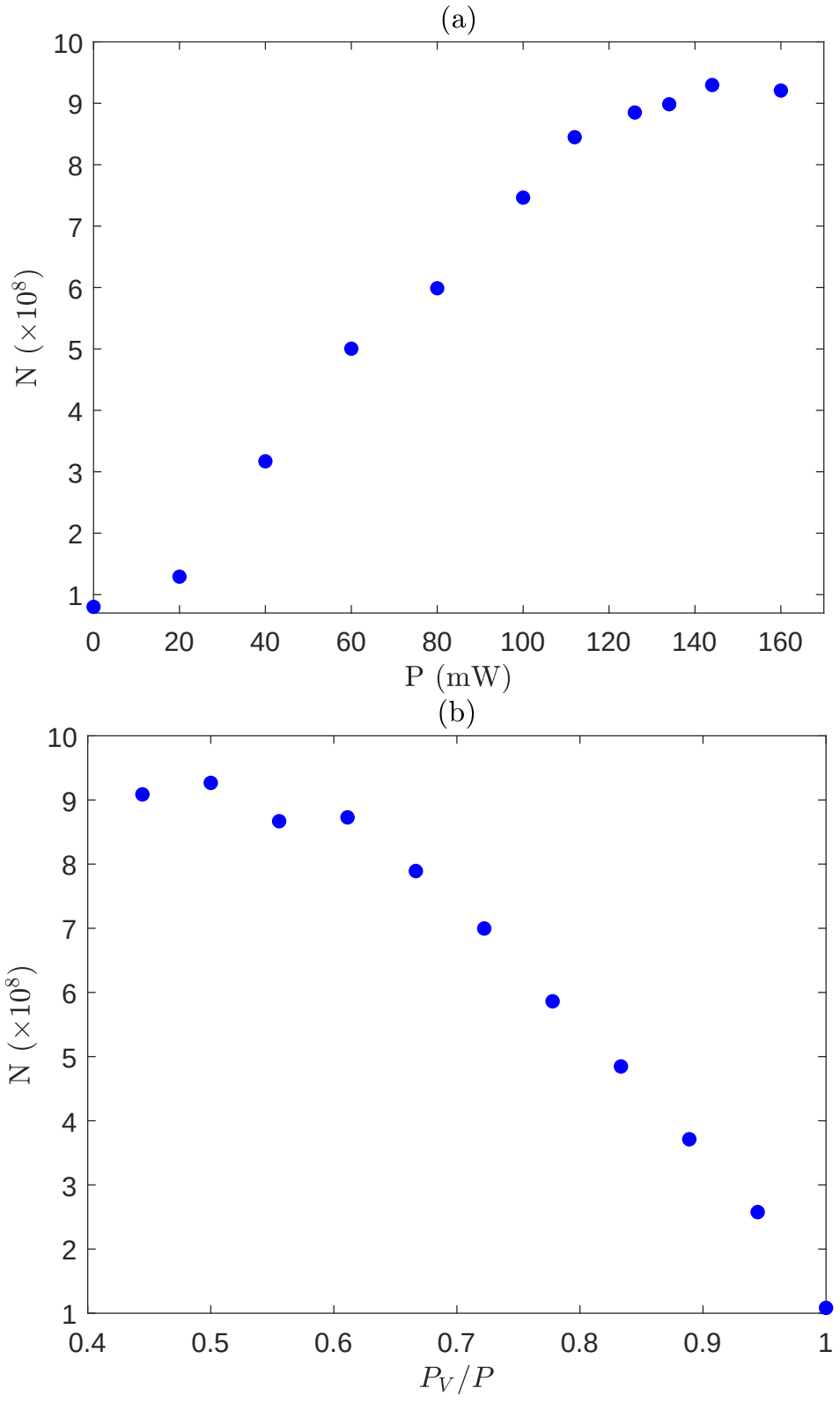

Figure 3.12: (a) Number of atoms in 3D-MOT as a function of total power P. P is divided equally between the two polarization components. (b) The performance of the hybrid slowing scheme as a function of P_V/P. P_V is the power of the beam with vertical polarization.

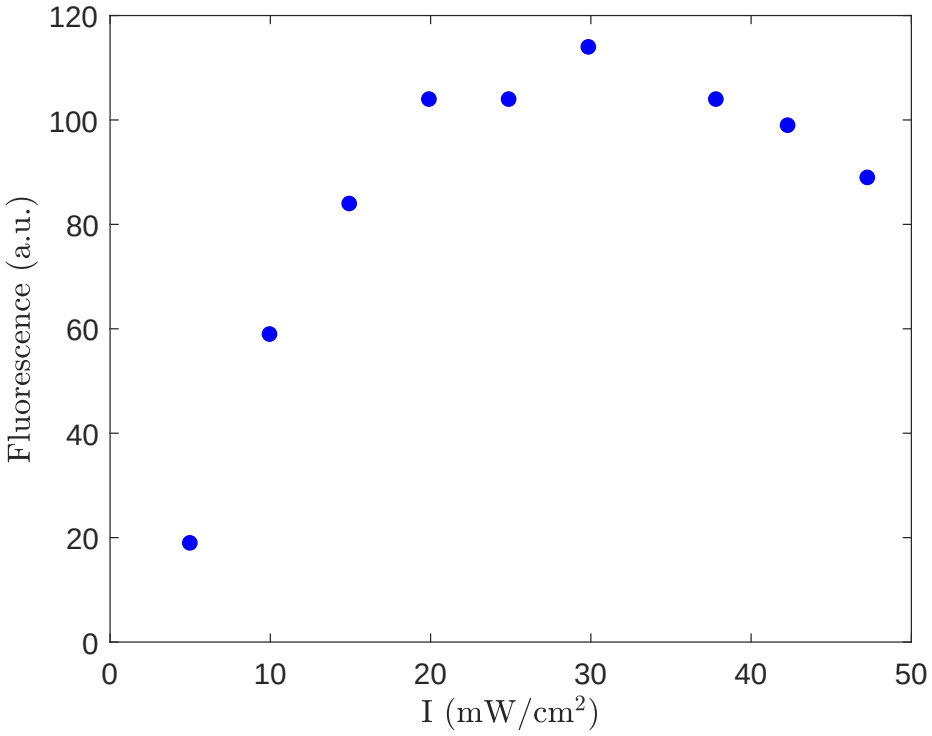

Figure 3.13: Fluorescence signal of 3D 461nm-MOT as a function of total 2D MOT beam power.

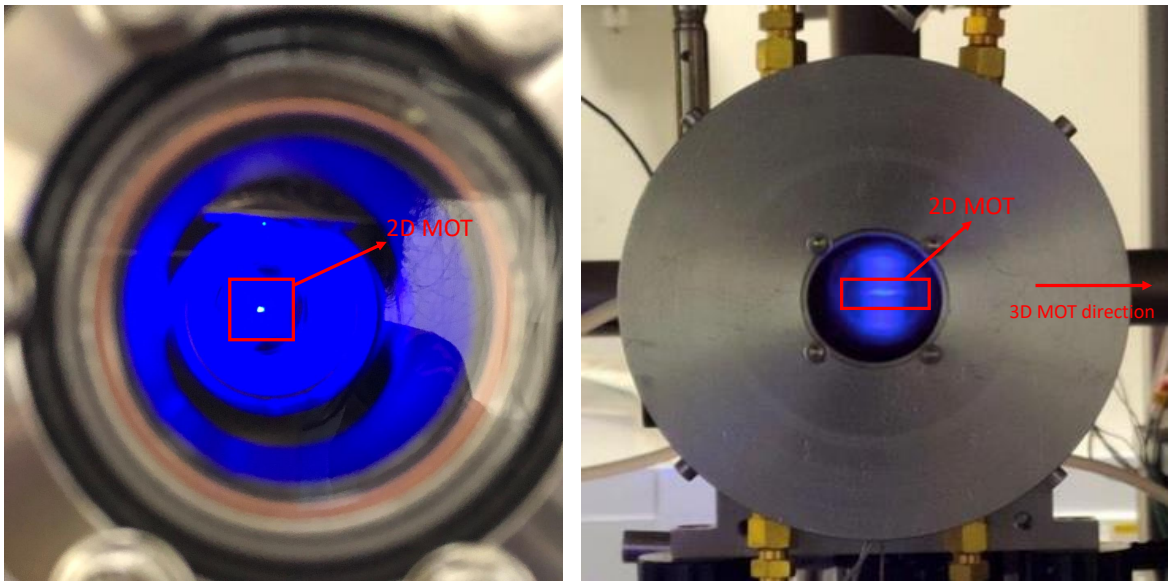

Figure 3.14: 2D atomic beam source seeing from push beam window (left) and atomic beam slower window (right).

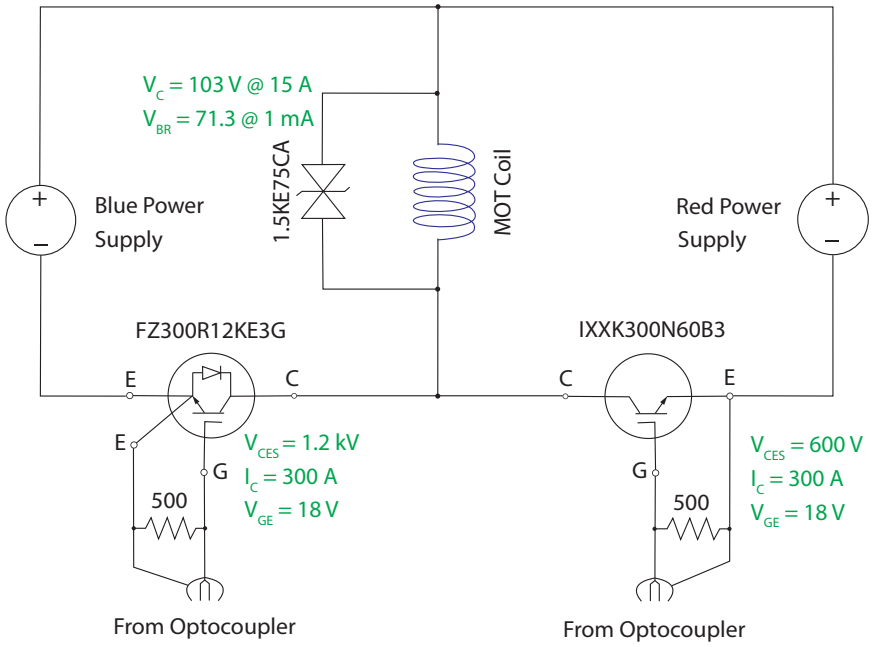

Figure 3.15: Schematic of MOT coil switching circuit. The current of the coils are controlled by IGBTs, and the transient-voltage-suppression diode are used to switching off the magnetic field.

3.4 3D MOTs

After the accomplishment of the 2D cold atomic beam stage, a push beam resonant to $^1S_0$ to $^1P_1$ transition is utilized to push the atoms into the science chamber, In the science chamber, the 3D MOT operates at 461 nm, followed by the MOT operating at 689 nm to prepare the ultra-cold atomic source. This section delves into a comprehensive delineation of this procedure, encompassing the magnetic field generation, laser setup, the experimental sequence governing the MOT, as well as the calibration and optimization strategies crucial for streamlining the process.

3.4.1 MOT coil system

The switching circuit of the MOT coil is shown in Figure 3.15. Both the blue and red MOT magnetic fields are switched by IGBTs, and the specifications of which are shown in the figure. The blue power supply delivers 110 A of current to generate 50 G/cm of magnetic field gradient for 461 nm-MOT. The output of the red power supply is controlled by an analog channel and produces a magnetic field gradient from 0.7 G/cm to 1.5 G/cm for red MOT stage.

The two IGBTs are driven by the CNY65 optocouplers to isolate the ground of the switching circuit. The optocoupler can give a maximum output current of 100 mA. The TTL signal is provided by a digital channel or a MOSFET driven by a digital channel (Using a MOSFET ensures that there is sufficient current to drive the optocoupler). The typical rise and fall time of this optocoupler circuit is ~ 5 μs and ~ 12 μs. The IGBTs and transils are on the water-cool-cooper plate (see Figure 3.16).

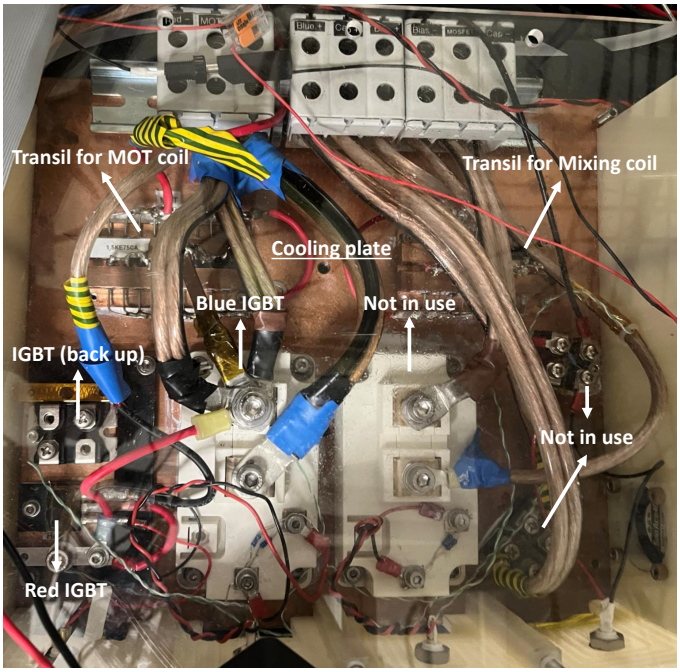

Figure 3.16: Cooling plate of MOT coil and mixing coil switching circuit.

3.4.2 461 nm MOT

After obtaining the cold atomic source at the center of 2D cross, a push beam operating at 461 nm is applied to push the atoms from the source to science chamber. The distance between the 2D MOT and 3D MOT is about 40 cm. In order to optimize the push beam, we collected the fluorescence signals in 3D 461 nm MOT while adjusting either the detuning or power of the push beam. Based on the results shown in Figure 3.17(a), the push beam is set to resonance. In the outcomes revealed in Figure 3.17(b), the number of atoms prepared in 3D 461 nm MOT is initially increasing with the power of push beam, but then decreases after reaching approximately 80 μW. This behavior is attribute to the fact that the atom velocity increases with the power of push beam. Consequently, when the speed exceeds the capture velocity of the MOT, atoms are no longer be cooled and captured, resulting in a reduction in the number of atoms prepared in the MOT. Thus, the beam power is set at 80 μW.

Upon reaching the science chamber, the atoms undergo cooling and trapping through the operation of the 3D MOT, which operates at 461 nm on the transition from $^1S_0$ to $^1P_1$. This is a fast transition with the linewidth of 32 MHz, which can be utilized to capture and cool down the atoms rapidly. The laser schematic of the blue MOT beam is shown in Figure 3.9. After frequency-shifted to -58 MHz, the beam is overlapped with the red lasers (689 nm, 707 nm and 679 nm) and split into six beams by polarizing beam splitter (PBS). Figure 3.6 illustrates the arrangement of the six beams: four of them are aligned at a 45° to gravity, while the remaining two are on the horizontal plane. The diameter of the blue MOT beams is 30 mm, and the power of the total six beams is optimized based on the fluorescence of 461 nm MOT, as shown in Figure 3.18. The number of atoms captured in 461 nm MOT saturates at around 50 mW/cm^2, which closely matches the saturation power of the 461 nm light.

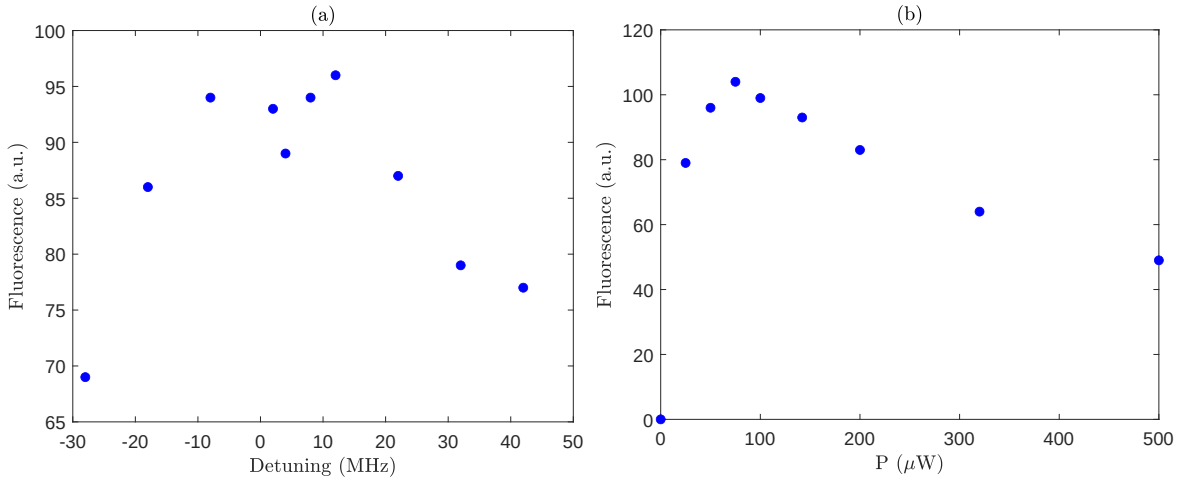

Figure 3.17: Calibration of the push beam power and frequency. The left plot shows the fluorescence of the 461 nm MOT with the scanning of push beam frequency, while the right figure is the fluorescence changing with different power.

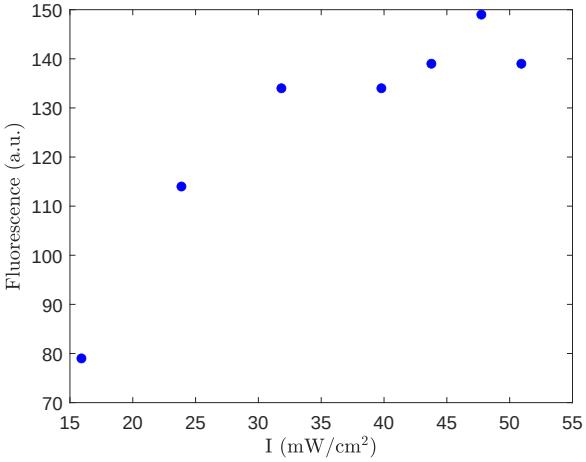

Figure 3.18: Fluorescence of 461 nm MOT versus 3D laser power.

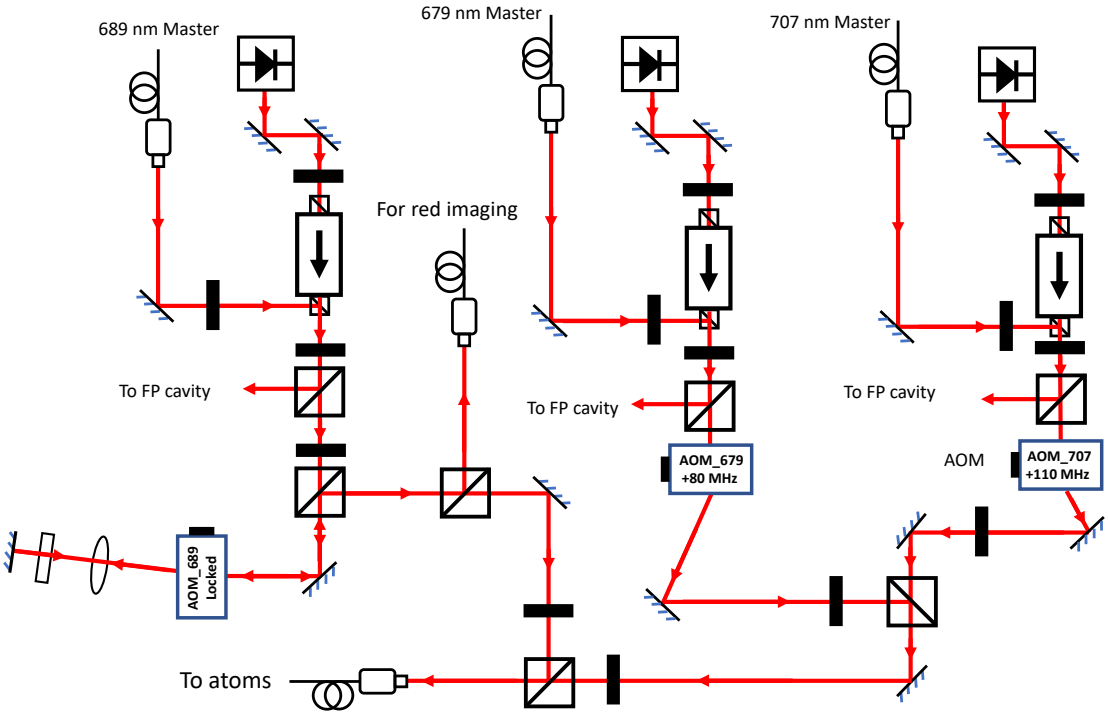

Figure 3.19: Schematics of 689 nm, 707 nm and 679 nm laser system. The diode lasers are injected, frequency shifted, coupled to the same fiber and sent to atoms. The master lasers are obtained from the "Sr I" project in our lab [3]. FP cavity: Fabry-Perot cavity. The symbols are given in Figure 3.8.

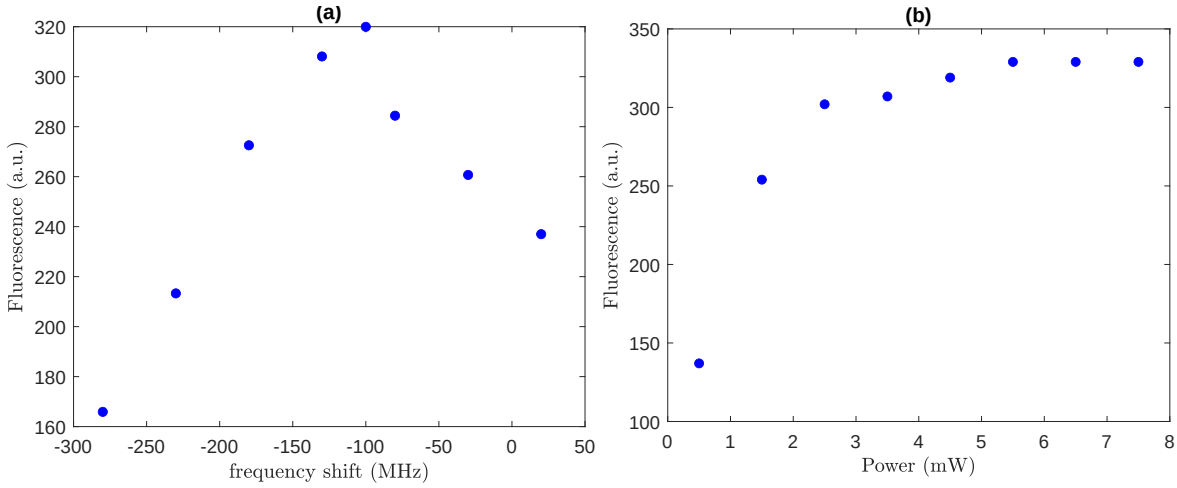

Figure 3.20: Fluorescence of 461 nm MOT changing with frequency shift away from the resonance of strontium-87 (a) and power (b) of 707 nm laser. In figure (a), the data points are taken with the power of 5.5 mW. The data in figure (b) is collected with the optimized frequency shift (∼110 MHz).

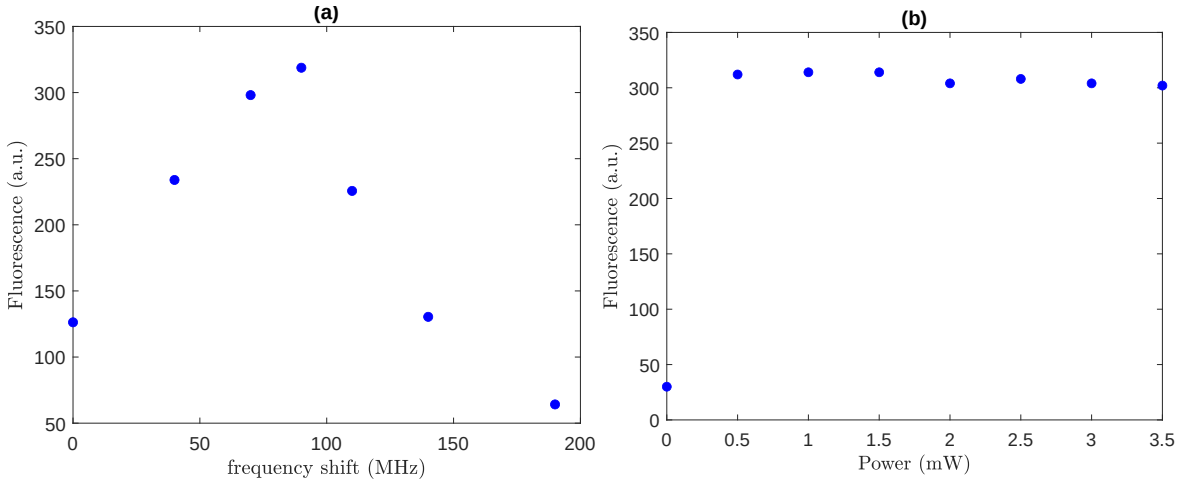

Figure 3.21: Fluorescence of 461 nm MOT changing with frequency shift away from the resonance of strontium-87 (a) and power (b) of 679 nm laser. In figure (a), the data points are taken with the power of 1.8 mW. The data in figure (b) is collected close to the optimized frequency shift (∼80 MHz).

During the operation of the blue MOT, repump lasers operating at 707 nm and 679 nm are utilized to eliminate the shelving in the $^3P_2$ state and bring the atoms back to the ground state $^1S_0$. The schematics of the repump laser system is shown in Figure 3.19. The master lasers for the repumpers have been prepared in another project with ^{87}Sr [3]. After being injected, the beam samples are obtained from the slave lasers by half-wave-plates and PBS's. These beam samples are sent into a Fabry-Perot cavity to monitor the injection. Subsequently, the slave laser beams are directed through AOMs for frequency adjustment to fit ^{88}Sr transitions and are combined with a PBS. In Figure 3.19, the repump lasers are overlapped with the 689 nm beam and coupled to a same fiber, eventually reaching the atoms for the cooling process.

Since the master lasers of the repumpers are from a different experimental setup based on ^{87}Sr, the detunings need to be adjusted to suit the bosonic isotope ^{88}Sr. Figures 3.20 and 3.21 showcase the characterization of the repump frequencies, optimizing their shifts by scrutinizing the fluorescence of the blue MOT while scanning the frequencies. Additionally, the power of the repump beams can also be optimized, as shown in the right panels of Figures 3.20 and 3.21. The specifications of the lasers are outlined in Table 3.1. Notably, despite a power loss due to cross-polarization after combining the two repump lasers, the combined power can still attain saturation levels. The optimization process portrayed in Figures 3.20 (b) and 3.21 (b) is conducted with the other repumper set at the optimal power.

With the combination of the 3D 461 nm MOT and the repumping lasers, the first stage of cooling and trapping takes approximately 1.5 s. Subsequent to this 461nm-MOT, there are approximately 9×10^8 atoms trapped with a temperature of roughly 1 mK.

3.4.3 689 nm MOT

Through the operation of the 461 nm blue MOT, atoms are captured and cooled to the millikelvin (mK) level [87]. To further decrease the temperature of the atomic source, the 689 nm MOT is implemented, which addresses the transition from $^1S_0$ to $^3P_1$. This spin-forbidden transition has a narrow linewidth of 7.5 kHz, which makes it possible to implement an efficient laser cooling and bring the temperature of atomic samples to the microkelvin (μK) level. In this section, I will discuss the details of the 689 nm MOT.

3.4.3.1 Red laser system

The red laser system, including lasers operating at 689 nm, 707 nm, and 679 nm, is relatively straightforward in our system, benefiting from the ready availability of master lasers from a previous lab project [3]. Therefore, the major necessary step is to inject the master laser into slave laser diodes. The laser schematics for these three lasers are presented in Figure 3.19.

The master lasers are brought to our lab via a 10 m fibers and utilized for injection into laser diodes. Since all the master lasers are initially frequency-shifted for ^{87}Sr, AOMs are instrumental in adjusting the frequencies to match the transition of ^{88}Sr in our experiment. The AOMs also serve as beam switches. Following modulation by the AOMs, the red beams with three wavelengths are combined using a polarizing beam splitter (PBS) and then coupled to the same fiber for the cooling stage. On exiting the fiber, the beam is segmented into three utilizing PBS's, then overlapped with the blue MOT beams using dichroic mirrors, before being further divided into six beams to foster the generation of 3D MOTs. The geometric arrangement of the red beams is illustrated in Figure 3.6, and the waist of the red beams is 5 mm when sent onto the atomic cloud.

3.4.3.2 689 nm MOT: ultra-cold atomic source preparation

The experimental sequence for operating the 689 nm MOT is illustrated in Figure 3.22. The atomic source captured in the blue MOT has a temperature of approximately 1 mK, resulting in a Doppler broadening at the level of MHz for the transition $^1S_0 \rightarrow ^3P_1$, significantly larger than its natural linewidth. Therefore, the objective of this sequence is to cultivate a cold, dense atomic sample with efficient transfer from the 461 nm MOT to the 689 nm MOT.

Following 1.5 s of operation in 461 nm MOT, the power of the blue laser is ramping down to 10 mW over 50 ms. This power reduction helps to eliminate the atoms with higher temperatures. The temperature of the atoms in 461 nm MOT is typically in milli-Kelvin level [87]. Unfortunately, we are unable to measure the temperature in our system due to the large size of the blue MOT since it is impractical to conduct a time-of-flight experiment using our imaging system. Following the power reduction of the blue beams, the broadband red MOT stage is initiated. During this stage, the detuning of the 689 nm laser is modulated between -2.2 MHz and -0.2 MHz, while maintaining a saturated power level. This allows for the transfer of a broader range of velocity classes from the

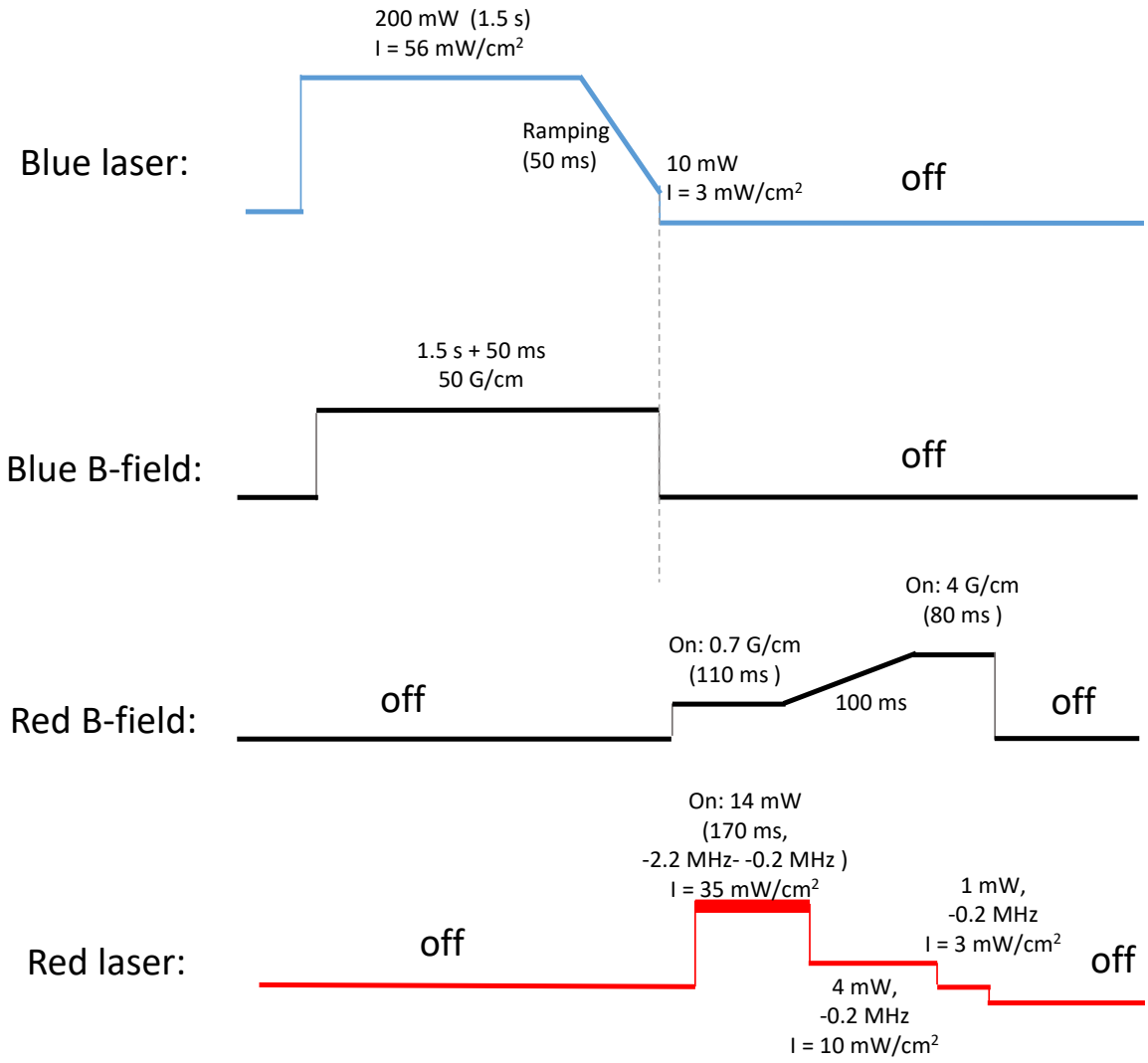

Figure 3.22: Experimental sequence for the generation of 689 nm MOT.

low-power blue MOT to the red MOT. Subsequently, the single-band red MOT stage is executed to further reduce the temperature and compress the size of the atomic sample. In this stage, the red laser is switched to a fixed frequency. To maintain the stability of the position of 689 nm-MOT, three pairs of Helmholtz coils are mounted to compensate the stray magnetic field during the experiment. The detailed information is discussed in Section 3.5.

3.4.4 Characterization of atomic source with Imaging System

To characterize the atomic sample and get the information such as temperature, atomic number as well as the fringes after interferometer, we perform a time-of-flight detection. After the atomic cloud is released, it will expand due to its non-zero temperature. In one dimension, the thermal velocity distribution can be expressed by the Maxwell-Boltzmann distribution:

$$f(v_i) = (\frac{m}{2\pi k_B T_i})^{1/2} \exp(-\frac{m v_i^2}{2k_B T_i}), \tag{3.1}$$

where T_i is the temperature of the atomic ensemble in the dimension $i = x,\ y,\ z$, v_i is the thermal velocity, and k_B is the Boltzmann constant. The position of an atom after time t is given by

$$x_i = x_{i0} + v_i t, \tag{3.2}$$

where x_{i0} is the initial position. Take average over all the atoms,

$$\langle x_i \rangle = \langle x_{i0} \rangle + \langle v_i \rangle t = \langle x_{i0} \rangle \tag{3.3}$$

Here, the averaged velocity $\langle v_i \rangle$ is taken to 0 in thermal motion. Similarly, from the equation $x_i^2 = x_{i0}^2 + v_i^2 t^2 + 2x_{i0} v_i t$, we have

$$\langle x_i^2 \rangle = \langle x_{i0}^2 \rangle + \langle v_i^2 \rangle t^2 \tag{3.4}$$

with $\langle x_{i0} v_i \rangle = 0$.

Thus, the expansion above indicates that the atomic cloud size can be calculated with $\sigma_i(t) = \sigma_i(0) + k_B T_i t^2/m$, which can be used to calibrate the atomic sample by measuring the size of the cloud with a series of expanding time.

$$T_i = \frac{\sigma_i^2 - \sigma_{i0}^2}{t_i^2 - t_{i0}^2} \cdot \frac{k_B}{m} \tag{3.5}$$

One of the examples for the calibration of temperature is shown in Figure 3.23: the atomic cloud is falling down with the expansion. The images are taken with different time-of-flight, and the temperature of the atomic sample can be obtained from the slope of the linear fitting with σ^2 versus t^2. The transition $^1S_0 \rightarrow {}^1P_1$ is used to do the fluorescence detection in our experiment. Notably, the temperature difference between x and y axis can be attribute to the power imbalance of the MOT beams.

The typical number of atoms in red MOT is approximately 10^7, with a temperature of approximately 1 μK, which give a density of 4×10^{10} cm^{-3}. The typical parameters of red MOT are similar to those found in other referenced setups [56] [65].

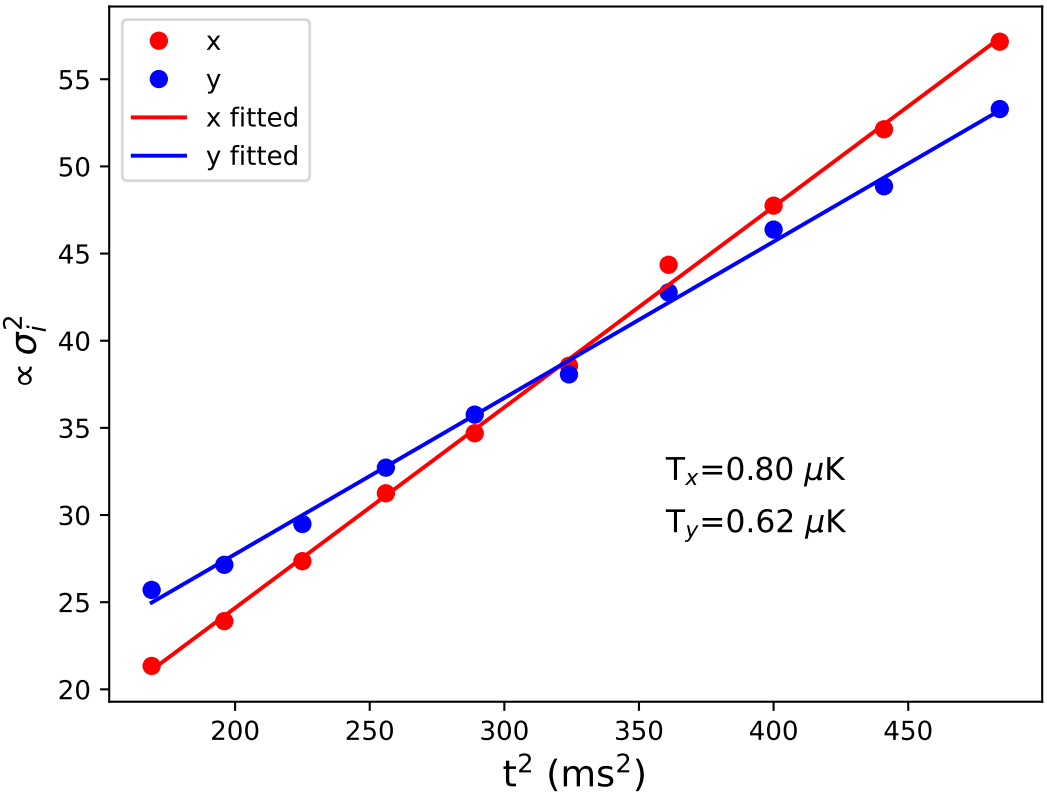

Figure 3.23: Temperature measurement with time-of-flight method.

3.5 Stabilization: magnetic field compensation system

The narrow $^1S_0 \rightarrow {}^3P_1$ intercombination line transition is sensitive to magnetic fields at the mG level [88]. Due to human activities, we observe occasional jumps of the ambient magnetic field on the order of 10 mG. We implement an active control system to compensate the external magnetic field, including the random jumps, other slow varying and DC contributions, as well as the AC 50 Hz line contribution. In the following, we describe the main components of this system. A more extended description can be found in Ref. [84].

Our active control system includes three main components: a probe network consisting of eight 3-axis magnetic-field probes arranged in a cuboid geometry centered at the ultracold atomic cloud position, a personal computer (PC) for digital signal processing, and three pairs of quasi-Helmholtz coils to perform the magnetic-field active compensation in 3D. The probe network and coils are shown in Figure 3.24.

3.5.1 Magnetic probe

Each 3-axis magnetic-field probe comprises one Honeywell 1-axis (HMC1001) sensor and one 2-axis (HMC1002) sensor. These sensors are anisotropic magnetoresistive sensors [89, 90, 91]. Each axis of the HMC sensor contains four permalloy resistive strips arranged in a Wheatstone bridge configuration.

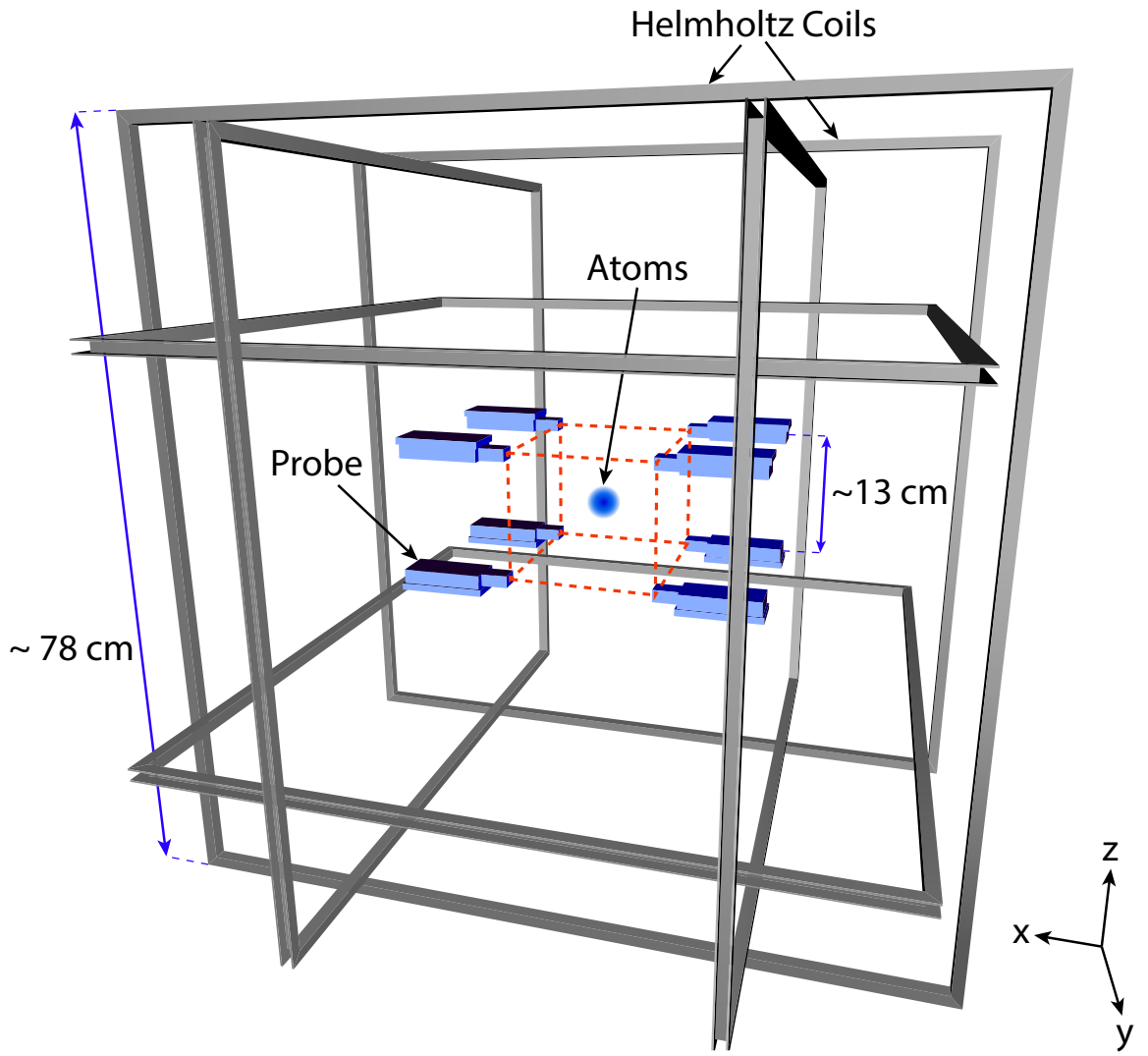

Figure 3.24: Arrangement of the eight magnetic-field probes and the compensation coil system centered around the ultra-cold atomic cloud.

The sensor operates in the linear regime of the magnetoresistive response where the output bridge voltage is a linear function of the magnetic field. The sensitivity of the sensor relies on the alignment of the permalloy magnetization along an easy axis. A strong external magnetic field could disrupt the permalloy magnetization, resulting in a loss of sensitivity. To maintain the sensors' sensitivity, before each measurement we align the resistive strip magnetization by means of a current pulse sent in the set/reset strap of the chip. Furthermore, we reverse the magnetization direction to have it parallel or antiparallel to a chosen axis in successive measurements. Taking the difference of two such measurements removes magnetic-independent offsets and their temperature dependence [91].

To achieve an optimum sensitivity, the bridge output voltage for each axis is amplified with a gain of 200, and digitized with a 16-bit analog-to-digital converter (ADC). We achieve a resolution of around 34 μG per digital level for each axis of the probe, and a full operational range of approximately ± 1 G.

We characterize the noise spectral density of the 3-axis magnetic probes in a zero Gauss chamber (ZGC). The noise spectral density of each probe (shown in Figure 3.24) is typically flat between 100 mHz to 50 Hz, with a value of around 2.7 $\mu\mathrm{G}/\sqrt{\mathrm{Hz}}$. This is consistent with the Johnson noise of an 850 Ω resistor (the typical bridge resistance of the HMC sensors) after taking into account the effect of the op-amp amplification and the ADC. The root-mean-square (rms) noise calculated for a bandwidth up to the Nyquist frequency of 244 Hz is below 38 μG, setting the limit on the measurement resolution.

3.5.2 Probe network

Eight 3-axis probes are arranged in a cuboid configuration around the science chamber with separations of 155 mm, 115 mm, and 123 mm along x, y and z directions, respectively. The readout time of the probes is synchronized across all the eight probes by a microcontroller. The probes take turns to send their readings to the microcontroller through a controller area network (CAN) protocol. A USB-CAN adapter is implemented to send all eight readings to a PC. The eight readings are then averaged to interpolate for the value of the magnetic field at the location of the atoms. The communication protocol limits our maximum sampling frequency for the probe network to 488 Hz. The Nyquist frequency of 244 Hz is sufficient to capture the relevant frequencies of the stray magnetic field.

With the probe network mounted around our experimental setup, we perform a measurement of the Cartesian components of the magnetic field homogeneous contribution, by averaging the reading of the eight sensors. The power spectral density (PSD) of the measurement corresponds to the blue trace in Figure 3.25. For comparison, the yellow trace is the averaged noise density of the readings from the eight probes measured independently in the ZGC. In this uncorrelated noise condition, we find a noise floor of $\sim 1\ \mu\mathrm{G}/\sqrt{\mathrm{Hz}}$. When installed in the lab the noise level at frequency $\gtrsim 5$ Hz is higher than the uncorrelated noise floor, possibly due to common mode noise from sharing the same power supply. On top of this, the probe network picks up stray magnetic field contributions at frequency $\lesssim 5$ Hz, and AC noise component mainly at 50 Hz. More precisely, we find an *rms* magnetic field noise of 150 μG at low frequency (0.001 Hz to 5 Hz) and 510 μG between 10 and 100 Hz, dominated by the AC-line

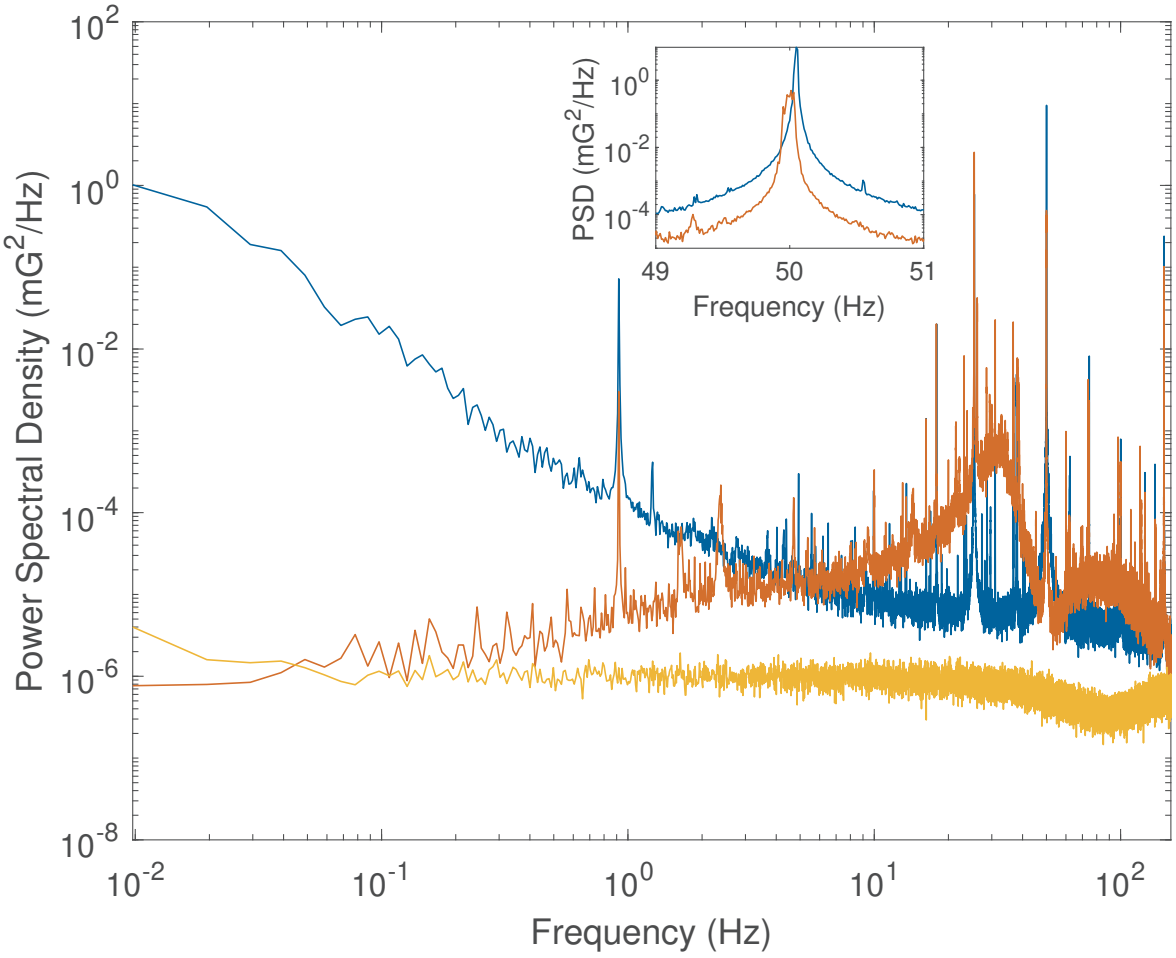

Figure 3.25: PSD of the magnetic field measurement along the z direction. The blue (red) trace is without (with) active feedback control. The yellow trace is the spectrum of the average readings from all eight probes measured independently in the ZGC. The inset shows a zoom of the PSD around 50 Hz.

contribution.

3.5.3 Feedback control

We use three pairs of square coils in quasi-Helmholtz configuration along the three orthogonal directions (x, y, z) to correct the stray magnetic field. Each coil consists of 18 turns and is wound on a square aluminum frame with a side of about 78 cm. Compared to the size of the probe network, this gives a sufficiently good field uniformity for the probe network to accurately interpolate the magnetic field. Each pair of the compensation coils is connected to a low noise current source, and generates a magnetic field of around 370 mG/A.

We implement digital filters, and generate an error signal to perform a proportional-integral-derivative (PID) feedback control of the stray magnetic field. For the compensation of the frequency noise below 5 Hz, a low pass filter with cutoff frequency 10 Hz is implemented on the averaged probe readings before the PID is applied.

To cancel the 50 Hz noise component, we first extract the quadrature amplitudes of the 50 Hz signal by mixing the probe reading with a 50 Hz signal, and then perform a low pass filtering with a cut-off frequency of 5 Hz. We then perform a PID control on the quadrature amplitudes before regenerating the feedback signal at 50 Hz. We allow for the 50 Hz phase of the feedback on the x, y and z components to be varied independently. We finally sum up both the low frequency and 50 Hz feedback signals.

3.5.4 Performance of the active control system

Beforehand, the performance of the active control system is evaluated when the experimental sequence is not running. The PSD is shown in Fig. 3.25 as the red trace. Compared to the blue trace we see that the PID feedback control is able to substantially reduce the low frequency components of the magnetic field noise up to 5 Hz. We observe a reduction in the PSD by more than five orders of magnitude close to DC, and one order of magnitude at 50 Hz (see inset of Fig. 3.25). We note that the 50 Hz feedback loop leads to a small shift and broadening of the 50 Hz peak, which we could not explained. An increase in the PSD due to the control of the 50 Hz component is also observed for frequencies above 10 Hz, with respect to the blue curve reducing the performance of the feedback loop. With the active control system, we find a typical *rms* magnetic field noise of 10 μG at low frequency (0.001 to 5 Hz) and 370 μG between 10 and 100 Hz. In both frequency range we observe a reduction of the noise compared to the open-loop values (see Sec. 3.5.2 B).

The operational range of the probes means that their readings become saturated whenever a magnetic field larger than 1 G is applied, which occurs for instance during the MOT stages. We apply a pause-and-hold strategy to compensate for the stray field during these stages, by retaining the feedback values before the application of the magnetic field. An example of the typical magnetic field reading during an experimental sequence is shown in Fig. 3.26. Here, the initial magnetic field offset

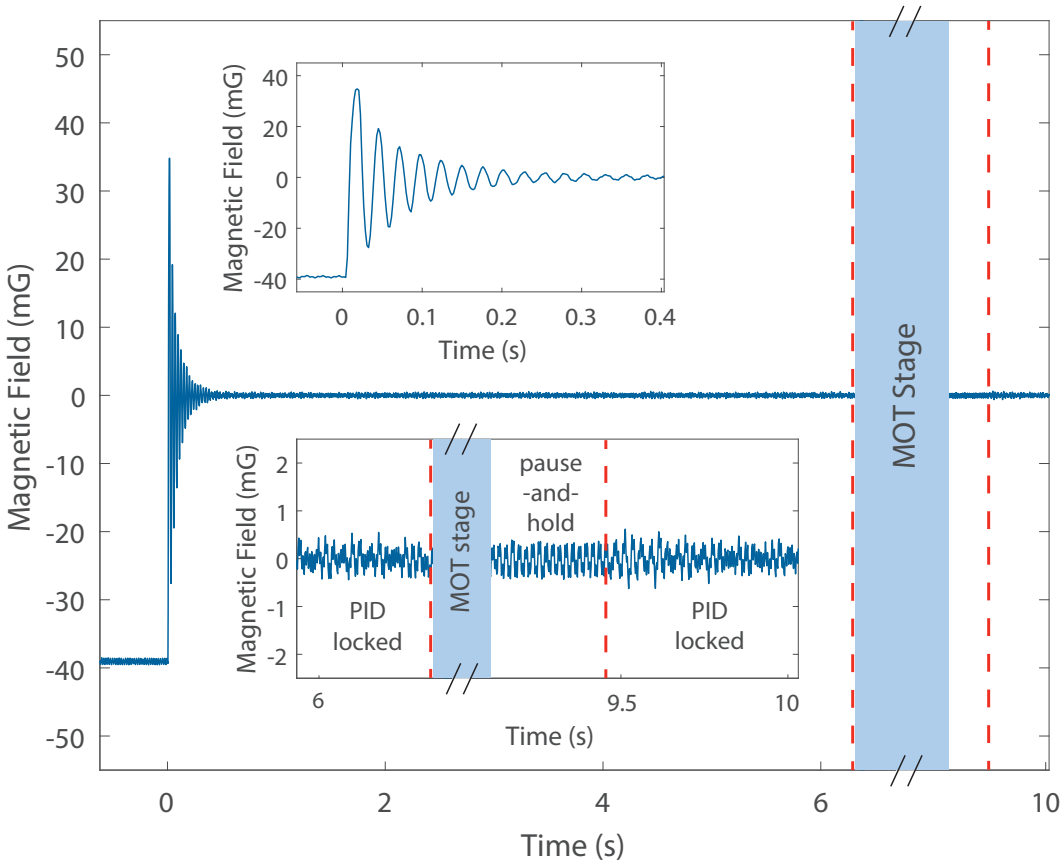

Figure 3.26: Magnetic field measurement during the experimental sequence. The top inset zooms into the magnetic field when the compensation is applied. The bottom inset zooms into the magnetic field during different stages of the experimental sequence. The pause-and-hold stage occurs between the two vertical red dashed lines.

of 40 mG is larger than typical jumps experienced in the lab. The $1/e$ settling time, as shown in the upper inset, is about 100 ms. Thus, a time interval larger than 100 ms is required between each pause-and-hold stage to ensure that the magnetic field compensation is correctly applied. During the typical pause-and-hold stage, the magnetic field fluctuations remain less than $\pm 500\,\mu$G, with an rms value of 210 μG over the measurement bandwidth.

The green open triangles in Fig. 3.27 show the typical magnetic field fluctuations measured in the lab within 24 h. From 9 a.m. to 7 p.m., we observe larger fluctuations due to nearby human activities. The magnetic field values are extracted from the sensors reading with an open feedback loop. Once the feedback loop is closed the magnetic field reading goes to zero (dashed lines) with fluctuations not visible for the range used in Fig. 3.27. We perform a measurements of the magnetic field using Faraday rotation on the cold atomic gas. At low laser intensity, the Faraday rotation angle θ depends linearly of the magnetic field, with a slope of $\Delta\theta/\Delta B \sim b_0 \times 0.28\,\mathrm{rad/mG}$, if the measurement is performed on the intercombination line [88]. b_0 is the optical thickness measured at resonance and at zero temperature [92].

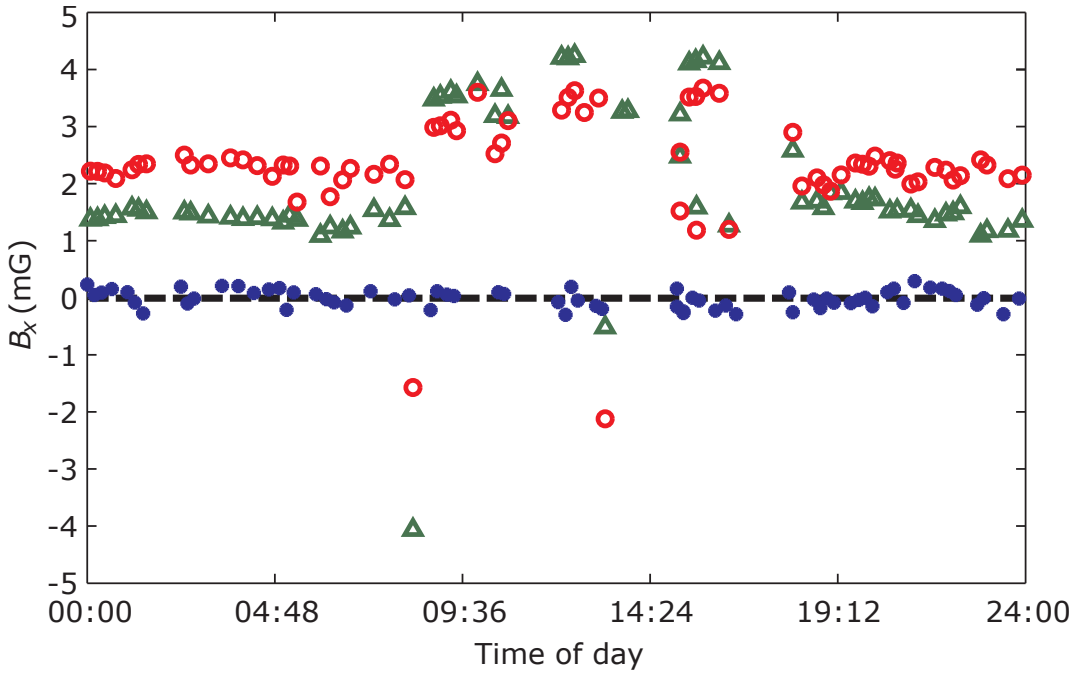

Figure 3.27: Measurement of the magnetic field variation in the course of 24 h. The green open triangles correspond to the sensors reading of the magnetic field along the x-axis. The red open circles and the blue circles are the reconstructed values of the magnetic field thanks to Faraday rotation measurement for unlocked case and locked to zero magnetic field (dashed line) case, respectively.

The Faraday measurement is performed by sending a resonant probe on the intercombination line along the x-axis with a polarization at $\pi/4$ angle with respect to the z-axis. The polarization rotation is analyzed thanks to a polarizing cube with s and p channels along the z- and the y-axis, respectively. The channel imbalance is recorded on a CCD camera (see Ref. [88] for more details). The red open circles and the blue circles in Fig. 3.27 correspond to the magnetic field extracted from the Faraday angle measurements in the unlocked and locked situation, respectively. For the unlocked case, we observe a qualitative agreement with the sensors reading. Mismatches are likely due to calibration bias of the Faraday response slope and overlooked nonlinear responses. Importantly, we extract a magnetic field value of $B_x = 10(150)\,\mu$G when the feedback loop is closed, in quantitative agreement with the expected null value.

As a final test of the performance of the active control system, we measured the position of the ultracold cloud in the 689 nm MOT along the z-direction with the PID feedback loop open or closed. The 689 nm MOT is produced following Ref. [86]. We apply random magnetic field jumps of 7.5 mG peak-to-peak to mimic the random magnetic field jumps due to human activities. Due to gravity, the z-position of the 689 nm MOT is shifted by 16 μm/mG. For each experimental run we apply a fix random value during the stage when the loop is closed, in contrast to the reality where magnetic field jumps can occur anytime. When a magnetic field jump occurs during the pause-and-hold stage, the active control system will compensate for it in the next PID locked stage. A comparison of the position

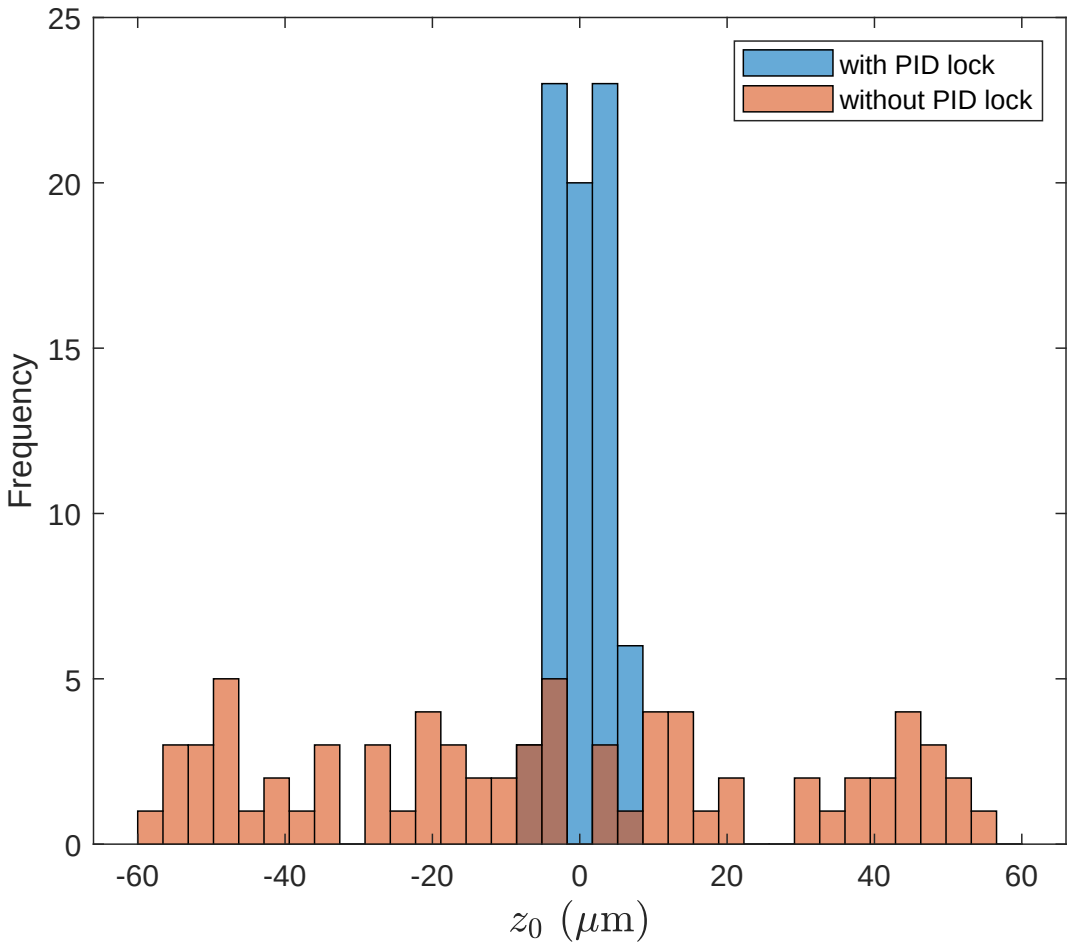

Figure 3.28: A histogram of the 689 nm MOT positions, z_0, along the vertical direction that is measured using fluorescence imaging, where blue (orange) bars shows the distribution of z_0 with the PID feedback loop activated (deactivated). For each of the two sets the measurement has been repeated 70 times.

of the 689 nm MOT subjected to this magnetic field fluctuation is shown in Fig. 3.28. We perform two experiments, one in open loop (orange bars) and another one in closed loop (blue bars). Without feedback, the random magnetic field modulation leads to a peak-to-peak variation in the MOT position of ± 60 μm. The active control system is successful in reducing this variation to less than ± 7 μm, a level that is consistent with the magnetic field fluctuations of less than ± 0.5 mG observed during the pause-and-hold stage in Fig. 3.25. This leads to a more consistent preparation of the cold atomic cloud.

3.5.5 Addressing magnetic field gradients

As discussed in Sec. 3.3, the bi-color slowing scheme and the 2D-MOT are generated thanks to permanent magnets. The contribution of those magnets at the level of the 3D-MOT consists of two gradient terms $\partial B_{x,z}/\partial z, x$, with an amplitude in the mG/cm range. Those gradients are too weak to disturb the cold gas in the MOT operating on the intercombination line, but can be a limitation for sensing applications requiring interferometers with spatially-extended surface area [93].

The sensor network measures the three Cartesian components of the magnetic field at eight positions around the MOT. Thus, we can extract the full magnetic field Jacobian matrix at the atomic cloud position, if the source is far enough from the sensors location to provide a good linear expansion of the magnetic field. This is indeed the case for permanent magnets of the bi-color slowing scheme and the 2D-MOT.

The compensation of the off-diagonal components of the magnetic field Jacobian matrix can be done using Golay coils as developed for magnetic resonance imaging devices [94]. We note that since the magnetic field gradients should be stationary, no active compensation is necessary here.

3.5.6 Conclusion

To conclude, in this chapter, I discussed in detail about the preparation of the ultra-cold atomic sample in our experimental system. Firstly, the overview of the experimental setup is illustrated, including the design of vacuum chamber, mounting of the breadboards, magnetic coils and the parameters for lasers and magnetic fields. The vacuum chamber composites of a cold atomic beam production stage and an UHV science chamber. Three magnetic coil systems are prepared around the atomic samples: MOT, mixing and compensation coils. Additionally, an optical enclosure and HEPA filter with temperature stabilization system are constructed to prevent the system from stray light and dust.

There are two main stages for the preparation of ultra-cold strontium atomic sample: the cold atomic beam stage and 3D MOTs. In the cold atomic beam stage, we design and implement a hybrid bi-color atomic beam slower to enhance the efficiency of atomic beam flux. The magnetic fields for 2D MOT and atomic beam slower are provided by permanent magnets. We achieve a factor of ten enhancement in terms of the number of atoms prepared in 3D 461 nm-MOT. The atomic beam is pushed into the science chamber via a push beam. Inside the chamber, the 461 nm-MOT and 689 nm-MOT are implemented. After the 3D MOTs stage, we obtain an ultra-cold strontium atomic sample at a temperature of 1 μK, and the number of atoms prepared in the 689 nm-MOT is about 10^7. We also implement an active feedback to compensate the stray magnetic field down to 1 mG during the experiment.

Based on this, in the next chapter, I will discuss several necessary manipulations of the ultra-cold atomic sample before the quantum sensing experiment, including loading the atoms into optical lattice, the clock transition for bosonic strontium-88 atoms, as well as the calibration of Bragg diffraction.

Chapter 4

Preparation for Quantum Sensing Stage

4.1 Introduction

After generating the ultracold atomic sample, we proceed with several preparation stages with the system for the quantum sensing. These steps encompass loading the atoms into an optical lattice operating at 813.427 nm and implementing magnetically-induced-spectroscopy of the clock transition in bosonic ^{88}Sr, as detailed in Section 4.2 and Section 4.3 respectively. Prior to the atom interferometer stage, a velocity selection stage is necessary, acknowledging the impact of atomic sample temperature on the Bragg diffraction process. In Section 4.4, an exploration into the utilization of a moving lattice for Bragg diffraction pulses is delved into, serving the purposes of velocity selection and the subsequent atom interferometer stage.

4.2 Loading into optical lattice

4.2.1 Preparation of lattice beam

In our experimental setup, an optical lattice is essential for holding atoms during specific stages of the sequence, such as reducing Doppler broadening during clock interrogation and stabilization periods for the mixing field. Within our system, there are three standing waves operating at the magic wavelength of 813.427 nm. The magic wavelength alleviates the systematic ac Stark shift from the trap. By trapping the atomic in a magic wavelength lattice, the clock transition frequency is independent of lattice beam power and remains unchanged. These standing waves are aligned both horizontally and vertically, being perpendicular to each other to form a three-dimensional lattice. The two horizontal beams are focused at the atomic position and retro-reflected by concave mirrors to form a standing wave and produce a periodic potential for the trapping. The schematic of the lattice beam is illustrated

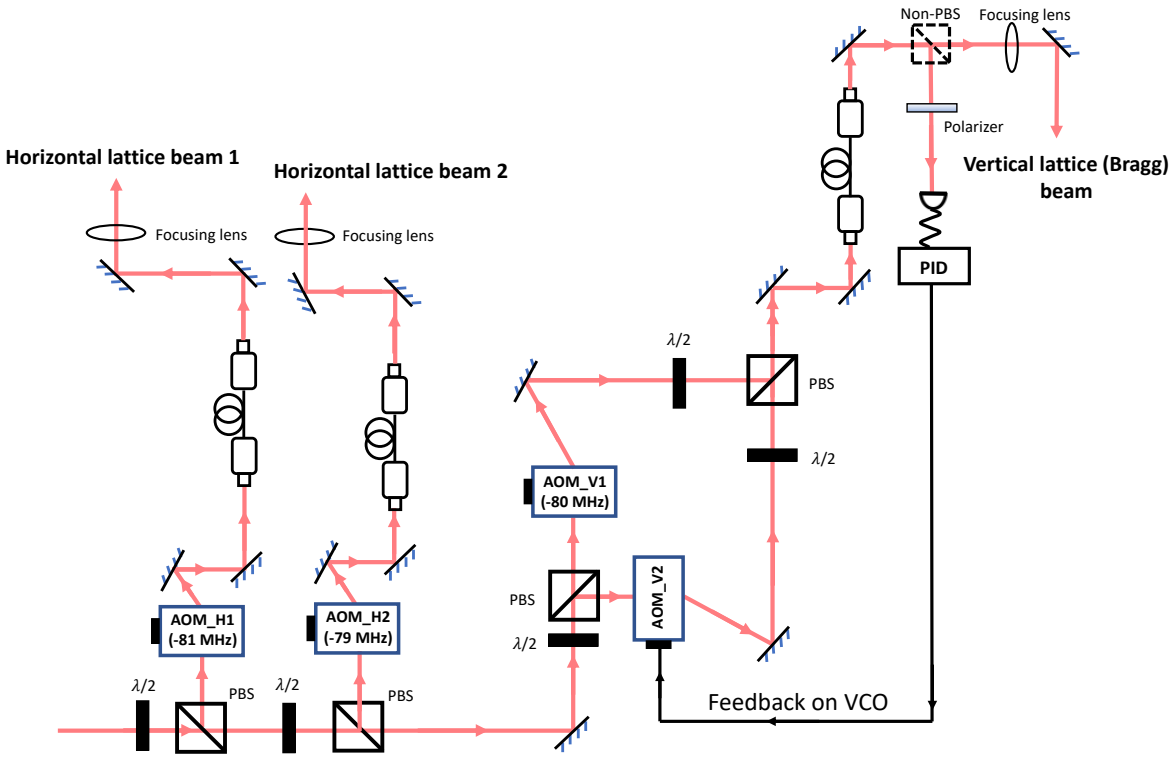

Figure 4.1: Lattice and Bragg beam layout. Three retro-reflected beams operate at 813.427 nm, the magic-wavelength for the clock transition, with two in the horizontal plane and one along the vertical axis. These beams are perpendicular to each other as depicted in Figure 3.6. Along the vertical axis, the optical lattice and Bragg lasers are formed by the same beams, which is switched by changing the RF source of the AOM (AOMV2).

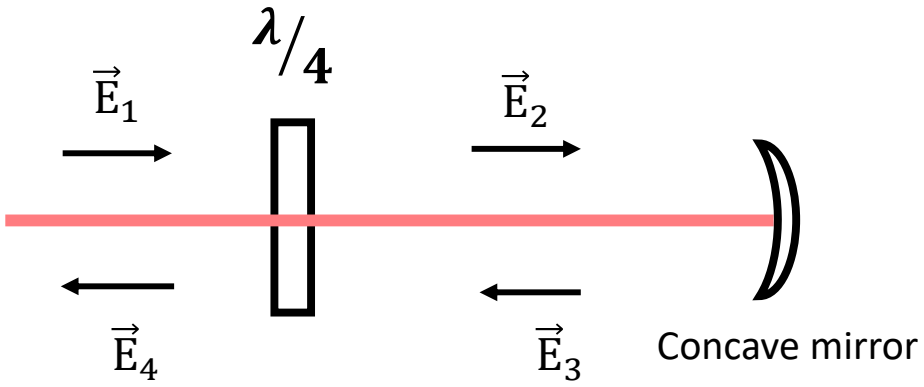

Figure 4.2: Laser schematics along the vertical axis.

in Figure 4.1. One of the horizontal lattices is overlapped with the clock laser via a dichroic concave mirror.

The vertical lattice is formed by two beams with cross-polarization. These beams are focused and retro-reflected, serving dual purposes for both the lattice and the Bragg pulses. A quarter-wave plate is strategically placed before the concave mirror to rotate the polarization of each beam by 90 degrees, allowing for the creation of either the stationary lattice for trapping or the moving lattice for the Bragg pulses.

Ensuring a stable lattice requires locking the phase difference between the two beams. The brief schematics of the vertical beam is illustrated in Figure 4.2, where $\vec{E}_1$ is the total incident field composed by the two beams with cross polarization, $\vec{E}_2$ is the field after the quarter-wave plate, $\vec{E}_3$ and $\vec{E}_4$ are the reflected light field before and after passing through the quarter-wave plate. An arbitrary incident field with a phase difference ϕ is given by

$$\vec{E}_1 = E_0 e^{i(kz-\omega t)} \left[\cos\frac{\theta}{2}\hat{x} + \sin\frac{\theta}{2}\, e^{i\phi}\, \hat{y}\right] \tag{4.1}$$

where $\cos\frac{\theta}{2}$ and $\sin\frac{\theta}{2}$ denote relative amplitude with respect to E_0, the total amplitude of the two beams. We rotate the axes from ($\hat{x}$, $\hat{y}$) to ($\hat{x}'$, $\hat{y}'$), with x' and y' along the plate axis at 45°:

$$\begin{aligned} \hat{x}' &= \frac{1}{\sqrt{2}}(\hat{x}+\hat{y}) \\ \hat{y}' &= \frac{1}{\sqrt{2}}(\hat{x}-\hat{y}) \end{aligned} \tag{4.2}$$

Then the incident field can be rewritten as

$$\vec{E}_1 = \frac{E_0}{\sqrt{2}} e^{i(kz-\omega t)} \left[\left(\cos\frac{\theta}{2} + \sin\frac{\theta}{2}\, e^{i\phi}\right)\hat{x}' + \left(\cos\frac{\theta}{2} - \sin\frac{\theta}{2}\, e^{i\phi}\right)\hat{y}'\right] \tag{4.3}$$

Suppose that the fast axis of quarter-wave plate is along $\hat{x}'$. After the plate, the field is expressed by

$$\vec{E}_2 = \frac{E_0}{\sqrt{2}} e^{i(kz-\omega t)} \left[\left(\cos\frac{\theta}{2} + \sin\frac{\theta}{2}\, e^{i\phi}\right) e^{i\frac{\pi}{2}}\hat{x}' + \left(\cos\frac{\theta}{2} - \sin\frac{\theta}{2}\, e^{i\phi}\right)\hat{y}'\right] \tag{4.4}$$

With this, we obtain the laser field after reflected by the mirror:

$$\vec{E}_3 = -\frac{E_0}{\sqrt{2}} e^{-i(k(z-2z_0)+\omega t)} \left[i\left(\cos\frac{\theta}{2} + \sin\frac{\theta}{2}\, e^{i\phi}\right)\hat{x}' + \left(\cos\frac{\theta}{2} - \sin\frac{\theta}{2}\, e^{i\phi}\right)\hat{y}'\right] \tag{4.5}$$

where z_0 is the nominal position of the reflecting mirror. After passing through the quarter-wave plate and sending back to the atoms, the field is given by

$$\vec{E}_4 = -\frac{E_0}{\sqrt{2}} e^{-i(k(z-2z_0)+\omega t)} \left[-\left(\cos\frac{\theta}{2} + \sin\frac{\theta}{2}\, e^{i\phi}\right)\hat{x}' + \left(\cos\frac{\theta}{2} - \sin\frac{\theta}{2}\, e^{i\phi}\right)\hat{y}'\right] \tag{4.6}$$

Thus, the total intensity of the laser experienced by the atomic cloud is

$$I = |\vec{E}_1 + \vec{E}_4|^2 = I_0\left(4 + 4\sin\theta\cos\phi\cos(2k(z-z_0))\right),\ I_0 = E_0^2 \tag{4.7}$$

Taking $\theta = \pi/2$, the intensity of the standing wave is significantly influenced by the phase difference. Fine-tuning the phase difference ϕ towards a value close to 0 or π is crucial for generating a stable

stationary lattice with high intensity. Therefore, a PID lock system becomes essential to uphold the required phase relationship between the beams.

The vertical beam serves dual purposes as both the lattice beam and the beam for Bragg diffraction. As shown in Figure 4.1, one of the AOMs ("AOM-V1") is driven by a fixed 80 MHz oscillator, whereas the other ("AOM-V2") can be controlled by a voltage-controlled oscillator (VCO) during lattice mode or a direct digital synthesis (DDS) during the Bragg pulse. During the lattice mode, the VCO supplies the RF source for AOM-V2, facilitating the phase locking feedback mechanism between the two beams. The two lattice beams, operating at a wavelength of 813.427 nm, are combined using a polarizing beam splitter (PBS) after passing through the AOMs and are then coupled to a fiber. A non-PBS (R:T=10:90) is positioned after the fiber output to extract a sample of the combined beam for phase locking. After passing through a 45° polarizer, this sample is led to a photodetector, and the beating signal between the beams is sent to the PID module, functioning as feedback on the VCO to maintain the phase locking point close to ϕ=0 for optimal lattice intensity and stability amidst operational vibrations.

The performance of the lock is evaluated by examining the optical signal of the mixed beam with and without the lock, as illustrated in Figure 4.3. The upper panel of Figure 4.3 depicts the optical setup for collecting the optical signal, which is used for the performance test. To evaluate the polarization fluctuation of the mixed beam, a polarizer is positioned before the photodetector in the path directed toward the atomic sample. The lower panel in Figure 4.3 displays the optical signal recorded by the photodetector, revealing a noticeable enhancement in the stability of the polarization. We see that the range of the phase fluctuation without lock is 2π within several tens of seconds, which corresponding to the voltage fluctuation $\Delta V = V_{max} - V_{min}$. The phase noise after lock can be determined as

$$\sigma_\phi = 2\pi \frac{\sigma_V}{\Delta V}, \tag{4.8}$$

where σ_ϕ is the phase noise range of the lattice beam with the PID lock; σ_V is the rms of the voltage obtained from the optical signal; ΔV is the full voltage range corresponding to phase fluctuation of 2π. With the data shown in Figure 4.3, the σ_ϕ is calculated to be 0.02π.

The calibration of the lattice beam such as the trapping frequency is obtained from the sideband of the clock transition spectroscopy. This is described in Section 4.3.

4.2.2 The loading of optical lattice

The atoms are loaded into the optical lattice after being prepared in the red MOT. Approximately 10^7 atoms are cooled and prepared in red MOT, with dimensions of 300 μm×700 μm×700 μm. Subsequently, 10^5 atoms are trapped into the optical lattice with the cloud waist of 50 μm. The loading performance, in terms of the atomic number in the vertical lattice, is illustrated in Figure 4.4. The green histogram represents the number of atoms loaded into the vertical lattice with the phase difference between the two vertical beams locked, while the black histogram represents the unlocked case.

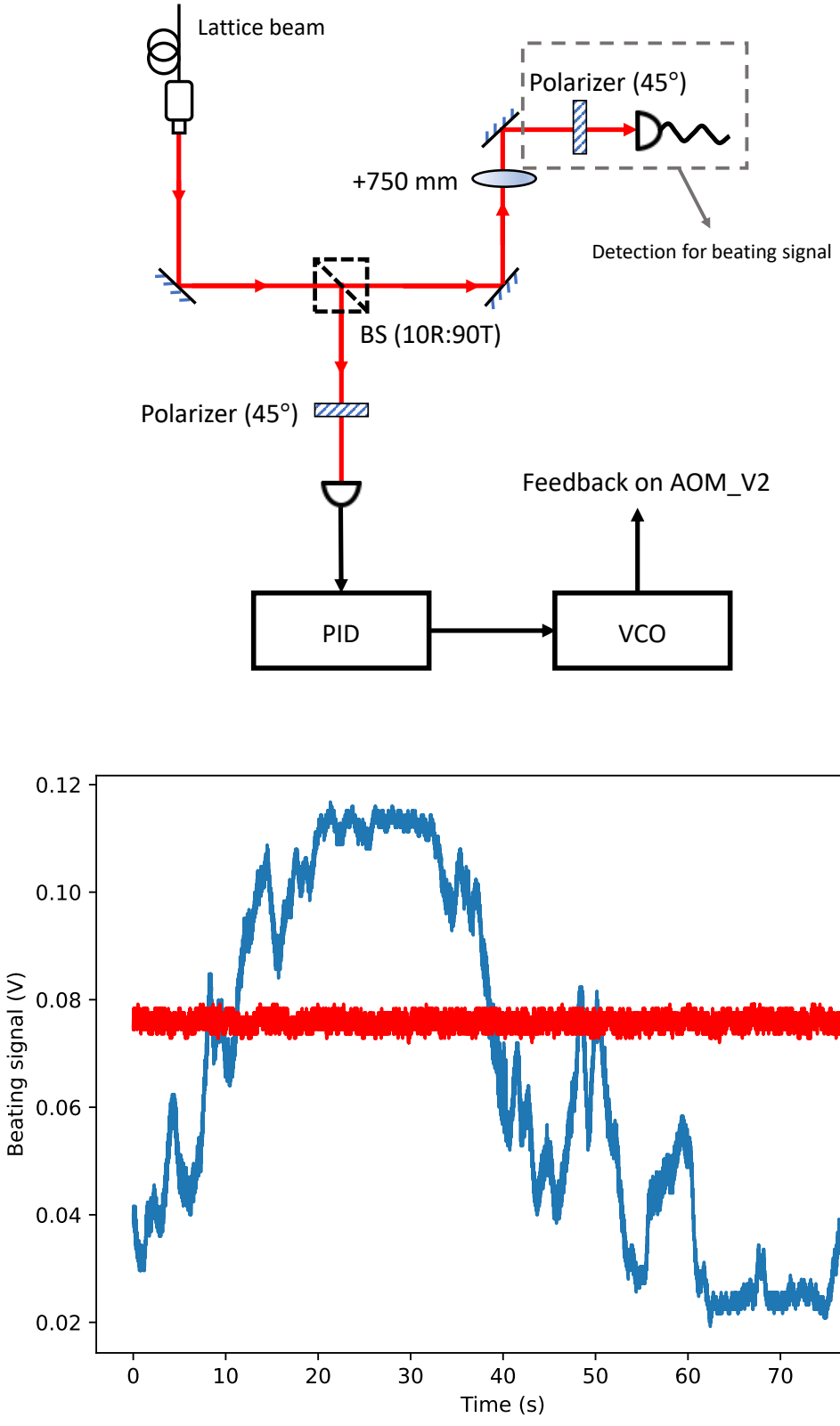

Figure 4.3: Top: The schematics to check the performance of the phase lock between two lattice beams. Bottom: The optical signal detected by the photodetector in 80 s with and without lock.

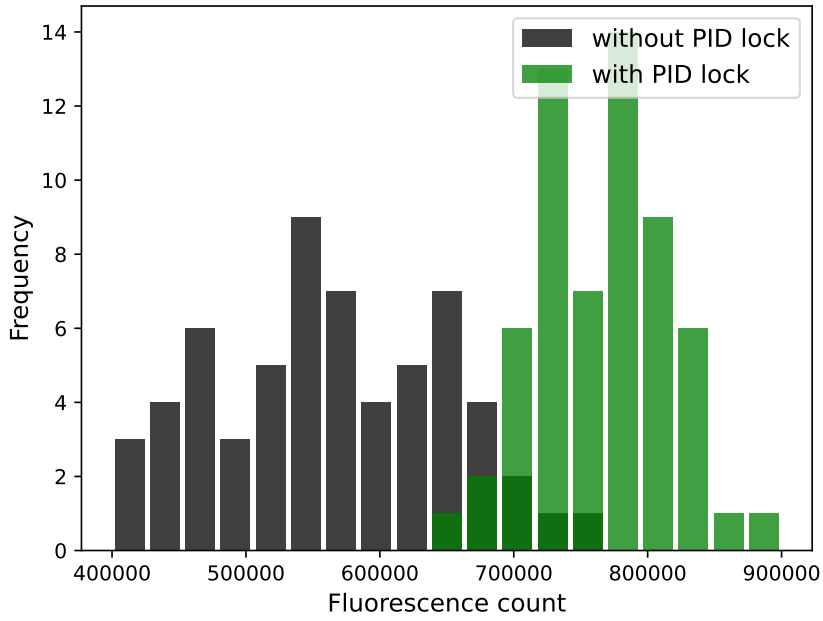

Figure 4.4: The histogram of the fluorescence count proportional to the number of atoms loaded into vertical optical lattice with (green) and without (black) the lock of phase difference between the two beams.

In the unlocked case, the AOMs for both beams are fed by a fixed RF source. From the results shown in Figure 4.4, an increase in number of atoms as well as an improvement of stability are observed.

4.3 Clock transition with strontium-88

4.3.1 Clock laser

The 698 nm clock laser is employed to excite the clock transition of the bosonic strontium-88. The source of clock laser is a commercial Optical Reference System (ORS) from MenloSystems. This system comprises a MOGLabs Cateye diode laser and a Fabry-Perot cavity constructed with ultra-low expansion glass (ULE) that has a finesse of approximately 210,000. The clock laser produced by this system exhibits a linewidth of approximately 17 Hz (discussed in section 4.3.1.2) and a power output of 7 mW. To increase the power of the clock laser, we inject the master laser into a slave, a laser diode. Given the clock laser's narrow linewidth in the Hertz range, thermal fluctuations in the fiber introduce phase disturbances that could potentially broaden the laser's linewidth. To address this, our clock laser setup incorporates two Doppler noise cancellation systems, as discussed in section 4.3.1.3, effectively eliminating phase noise for both the fiber from the master laser to the slave laser and the fiber transporting the slave laser to the experiment [95].

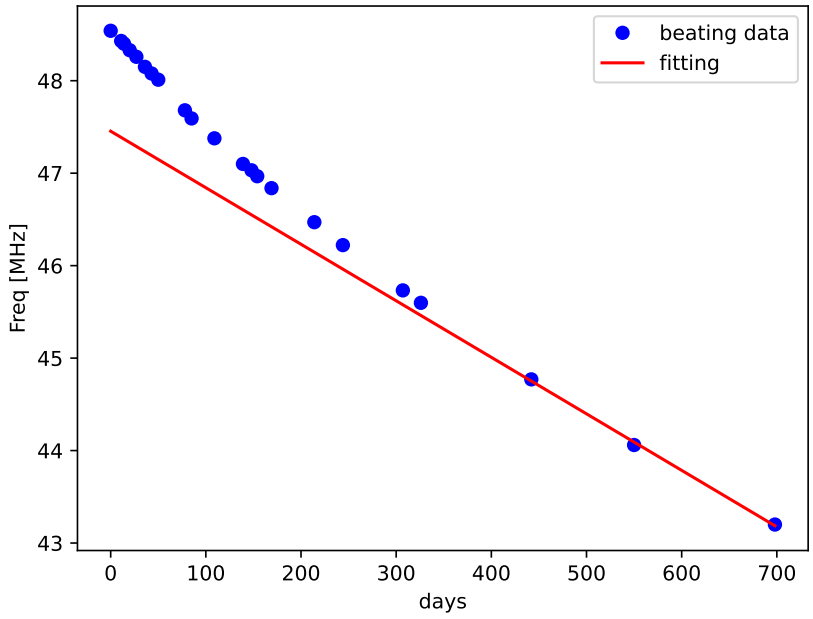

Figure 4.5: The beating frequency between frequency comb and the clock laser, which indicates the cavity drift of the master laser. The red curve is the linear fitting of beating frequency within the last 250 days, and this is used to obtain the drift rate of the system to compensate during the experiment.

4.3.1.1 Determination of the Clock Laser Frequency

To excited the clock transition, it is crucial to determine the clock laser frequency and tune it to the resonance value. The absolute frequency of the clock transition in the bosonic isotope of strontium-88 is measured as [69]

$$f_{^{88}Sr} = 429,228,066,418,008.3(1.9)_{\text{syst}}(0.9)_{\text{stat}}\ \text{Hz} \tag{4.9}$$

To prepare the clock laser, we first find a cavity mode close to the clock transition frequency. The frequency of the mode read from a lambda-mater with a 40 MHz precision is

$$f_{wvm} = 429.22829(4)\ \text{THz} \tag{4.10}$$

With this, the frequency of the clock laser can be more precisely determined by performing a beating between the clock laser and the frequency comb. The frequency comb has a repetition rate of 250 MHz and an offset frequency of +40.0(1) after frequency doubling. The comb tooth used for this beating can be calculated as (n×250 MHz) + 40.0(1) MHz, which gives n=1716913 according to the value of f_{wvm}. Consequently, the frequency of the clock laser can be determined by subtracting the beat frequency f_b from the frequency of the nth comb tooth.

$$f_c = f_{comb} \pm f_b \tag{4.11}$$

where the plus-minus sign indicates that the frequency difference we subtract from the beating can be on either positive or negative side of the comb line. The sign is determined by the measurement from

lambda-meter. The frequency of the clock laser is fine-tuned to the value $f_{^{88}Sr}$ by a double-pass AOM shown in Figure 4.6 and then determined from the atomic sample.

By measuring the beating frequency between the frequency comb and clock laser on different days, we are able to monitor and compensate the cavity drift for each experimental run. Figure 4.5 illustrates the change in beating frequency over time, revealing a decreasing drift rate over the past three years (decreasing from (-8.91±0.18) kHz/day to (-6.11±0.22) kHz/day).

To compensate for this drift, we perform a linear fitting with the beating frequency data collected over approximately 250 days to determine the drift rate γ (shown in the red curve in Figure 4.5). This rate is then employed to calculate the frequency change in our laboratory control system before activating the clock laser in the experimental sequence. We first implement the clock transition spectroscopy to record the resonant frequency f_0. With this, the system will automatically calculate the frequency considering the drift when switching on the clock laser in experimental sequence:

$$f = f_0 + \gamma \times t \tag{4.12}$$

where f is adjusted thank to a RF frequency sent to the double-pass AOM shown in Figure 4.6 to compensate the cavity drift of master laser. The precision of time t in Eq (4.12) during the compensation process is down to millisecond-level. Since we use the drift calculated from the frequencies over 250 days, which indicates that the changing of drift rate during this time will lead to an error. The maximum error is $\Delta\gamma$ =1 kHz/day. We usually calibrate the clock transition every three hours to reduce this drift change. Therefore, the maximum error for the compensation process is about 125 Hz. Compared to the Rabi frequency of the clock transition is 360 Hz during the sequence, this error is sufficient low for the experiment,

4.3.1.2 Linewidth of the clock laser

The linewidth of the laser can be estimated by the power spectral density (PSD) of the Pound-Drever-Hall (PDH) error signal. This PSD of the error signal is read from the oscilloscope and can be converted to the PSD of frequency fluctuation. In the following sections, the linewidth of the laser is estimated [96].

A monochromatic beam incident into a Fabry-Perot cavity can be written as

$$E_{inc} = E_0 e^{i\Omega t}, \tag{4.13}$$

where Ω is the laser frequency. The reflected beam consists of a promptly reflected beam and a set of leakage beams, which have the phase shift of π and $2nL\Omega/c$ respectively. The reflected wave can be expressed as

$$\begin{aligned} E_{ref} &= E_0 \left(re^{i(\Omega t+\pi)} + trte^{i(\Omega t-2L\Omega/c)} + tr^3te^{i(\Omega t-4L\Omega/c)} + ... \right) \\ &= -E_0 re^{i\Omega t} + (1-r^2)E_0 e^{i\Omega t} \frac{re^{-i\Omega/\Delta\nu_{FSR}}}{1-r^2e^{-i\Omega/\Delta\nu_{FSR}}}, \end{aligned} \tag{4.14}$$

where r and t are the reflection and transmission coefficient of the mirror, and $\Delta\nu_{FSR} = c/(2L)$ is the free spectral range of the cavity. The relationship between the cavity spectral range $\Delta\nu_{FSR}$ and the

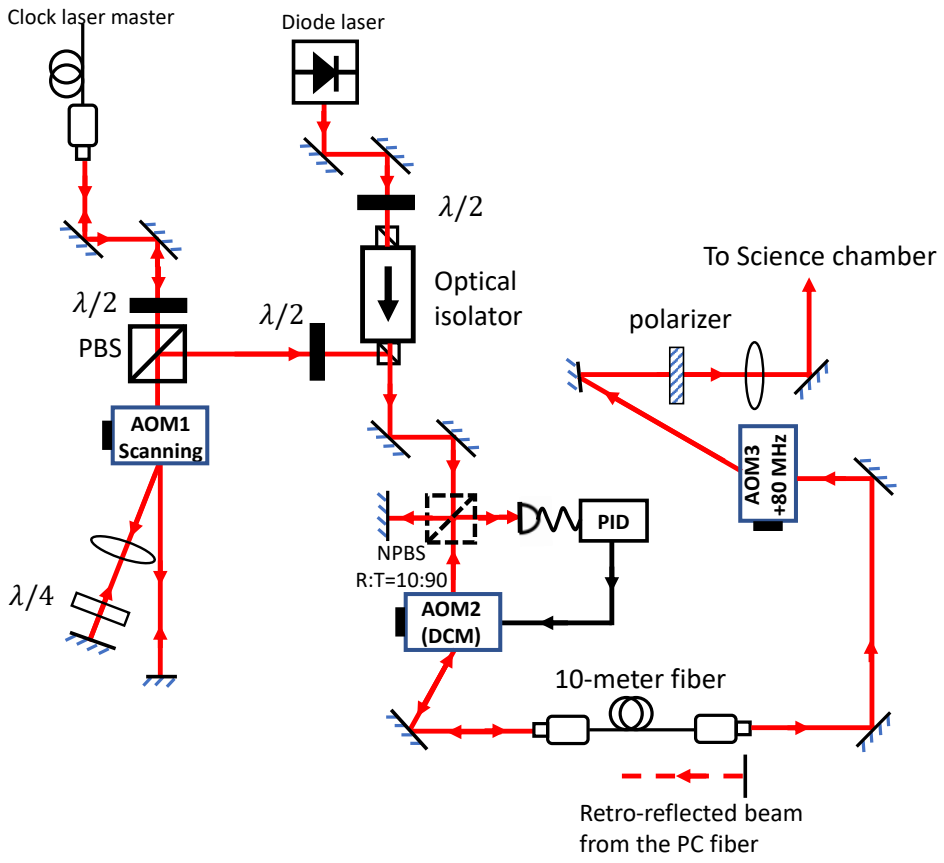

Figure 4.6: Clock diode laser layout. The master of clock laser is led through "AOM1" with double-pass, which is used for shifting the laser to the resonance of clock transition. "AOM2" is driven by VCO for Doppler noise cancellation of the fiber transporting the slave laser to the experiment table, and "AOM3" shifts the laser at the opposite direction of "AOM2" for switching as well as compensating the detunning from "AOM2".

linewidth of the cavity $\Delta\nu$ is given by

$$\begin{aligned} 2\pi\Delta\nu = \Delta\omega_c = \frac{\Delta\omega_{FSR}}{\mathcal{F}} = \frac{2\pi\Delta\nu_{FSR}}{\mathcal{F}} \\ \Delta\nu_{FSR} = \frac{\mathcal{F}\Delta\omega_c}{2\pi}, \end{aligned} \tag{4.15}$$

where $\mathcal{F} = \frac{\pi r}{1-r^2}$ is defined as the finesse of the cavity.

The reflection coefficient of the Fabry-Perot cavity can be expressed as

$$\hat{r}_c(\Omega) = \frac{E_{ref}}{E_{inc}} = \frac{r\left(e^{-i\Omega/\Delta\nu_{FSR}} - 1\right)}{1 - r^2 e^{-i\Omega/\Delta\nu_{FSR}}} \tag{4.16}$$

We consider the laser frequency Ω is close to a resonance of the cavity (i.e. $\omega_0/\Delta\nu_{FSR} = 2n\pi$ where n is an integer) and suppose that the reflection coefficient of the cavity mirror is close to 1. We can perform the Taylor expansion of the exponential around $\Omega = \omega_0$:

$$\begin{aligned} e^{-i\Omega/\Delta\nu_{FSR}} &\approx e^{-i\omega_0/\Delta\nu_{FSR}} - \frac{i}{\Delta\nu_{FSR}}(\Omega - \omega_0) \\ &= 1 - i\frac{1-r^2}{r}\frac{2(\Omega-\omega_0)}{\Delta\omega_c} \end{aligned} \tag{4.17}$$

With this approximation, the reflection coefficient can be rewritten as

$$\hat{r}_c(\Omega) = \frac{-i\frac{2(\Omega-\omega_0)}{\Delta\omega_c}}{1 + i\frac{2(\Omega-\omega_0)}{\Delta\omega_c}} \tag{4.18}$$

Now we consider a non-monochromatic beam with an average frequency of ω_L and a phase noise modelled by a function $\varphi(t)$ with $\langle\varphi\rangle = 0$. After a phase modulation by an electro-optic modulator (EOM), the incident beam can be expressed by [96]

$$\begin{aligned} E_{inc}(t) &= E_0 e^{i(\omega_L t + \varphi(t) + \beta\sin(\omega_m t)} \\ &\approx E_0 e^{i(\omega_L t + \varphi(t))}\left[J_0(\beta) + 2iJ_1(\beta)\sin(\omega_m t)\right] \\ &= E_0 e^{i(\omega_L t + \varphi(t))}\left[J_0(\beta) + J_1(\beta)e^{i\omega_m t} - J_1(\beta)e^{-i\omega_m t}\right], \end{aligned} \tag{4.19}$$

where J_i is the i-th order of the Bessel function. The expression above indicates that the incident beam in the cavity consists of a carrier with an average frequency of ω_L and two sidebands with an average frequency of $\omega_L \pm \omega_m$. If the carrier frequency is close to resonance and the modulation frequency $\omega_m \gg 2\pi\Delta\nu_{FSR}$, we can assume that the sidebands are completely reflected. Then the reflected beam can be written in the form of a convolution product as follows [96]:

$$E_{ref}(t) = E_0 e^{i(\omega_L t + \varphi(t))}\left(J_0(\beta)\epsilon(t) + J_1(\beta)e^{i\omega_m t} - J_1(\beta)e^{-i\omega_m t}\right), \tag{4.20}$$

where $\epsilon(t) = \int r_c(t')e^{-i\omega_L t'}e^{-i(\varphi(t)-\varphi(t-t')}\mathrm{d}t'$. The intensity of the reflected beam is given by

$$\begin{aligned} I_{ref}(t) &= |E_{ref}(t)|^2 \\ &= E_0^2\left(J_0^2(\beta)\,|\epsilon(t)|^2 + 2J_1^2(\beta)\right) + 4E_0^2 J_0(\beta)\mathscr{F}(\epsilon(t))\sin(\omega_m t) + \mathcal{O}(2\omega_m), \end{aligned} \tag{4.21}$$

where $\mathscr{F}(\epsilon(t)) = i(\overline{\epsilon(t)} - \epsilon(t))/2$. In the equation above, we are interested in the oscillation term, which can be isolated experimentally via a mixer and a low pass filer. If we feed the reflected electric

field intensity signal I_{ref} (which is modulated at ω_m) into the input of the mixer and another signal at ω'_m into the other input of the mixer, then the output signal will contain the modulations at $\omega_m - \omega'_m$ and $\omega_m + \omega'_m$. By setting $\omega_m = \omega'_m$ and remove the DC term, the error signal can be rewritten as

$$s(t) = 2E_0^2 J_0(\beta) J_1(\beta) \mathscr{F}(\epsilon(t)) \tag{4.22}$$

Now we suppose that the spectral width of the laser $\Delta\omega_L$ is much smaller than $\Delta\omega_c$. In this case, the phase fluctuation is small over the lifetime of the cavity. We can perform the approximation to $\epsilon(t)$ and the error signal can be written as

$$s(t) = 2E_0^2 J_0(\beta) J_1(\beta) \int \varphi(t-t') \frac{r_c(t') e^{-i\omega_L t'} + \overline{r_c(t')} e^{i\omega_L t'}}{2} \mathrm{d}t' \tag{4.23}$$

We also assume the average laser frequency ω_L is close to the resonance frequency of the cavity ω_0. Inserting the expression in Equation 4.3.1, the Fourier transform of the error signal is given by

$$\hat{s}(\Omega) = -2E_0^2 J_0(\beta) J_1(\beta) \frac{2}{\Delta\omega_c} \frac{1}{1 + i\frac{2\Omega}{\Delta\omega_c}} \hat{\omega}(\Omega) \tag{4.24}$$

The power spectral density of the intensity fluctuations of the error signal can be written as

$$S_s(\Omega) = 4E_0^2 J_0^2(\beta) J_1^2(\beta) \frac{4}{\Delta\omega_c^2} \frac{1}{1 + \left(\frac{2\Omega}{\Delta\omega_c}\right)^2} S_\omega(\Omega) \tag{4.25}$$

Here, $S_s(\Omega)$ has the units of $\mathrm{mW}^{-2}/\mathrm{Hz}$ while the error signal measured from oscilloscope has the units of Volt. Therefore, we need to find the relationship between $S_s(\Omega)$ and $S_v(\Omega)$, which is the power spectral density of the intensity fluctuation of the error signal experssed in the units of V^2/Hz.

Let R and G be the responsitivity and gain of the detector, which have the units of Ampere/Watt and Volt/Ampere respectively. With this, the quantity RG converts the units of optical intensity to Volt. The power spectral density of the intensity fluctuations of the error signal in units of V^2/Hz can be expressed as

$$S_v(\Omega) = 4(RGA)^2 E_0^2 J_0^2(\beta) J_1^2(\beta) \frac{4}{\Delta\omega_c^2} \frac{1}{1 + \left(\frac{2\Omega}{\Delta\omega_c}\right)^2} S_\omega(\Omega), \tag{4.26}$$

where A is the surface area of the detector.

Let us suppose that the beam incident on the cavity is monochromatic with frequency ω_L. The expression of error signal is reduced to

$$\hat{s}(\Omega) = -2E_0^2 J_0(\beta) J_1(\beta) \frac{\frac{2(\omega_L - \omega_0)}{\Delta\omega_c}}{1 + \left(\frac{2(\omega_L - \omega_0)}{\Delta\omega_c}\right)^2} \tag{4.27}$$

The error signal in the units of Volt can be written as

$$\hat{v}(\Omega) = -2RGAE_0^2 J_0(\beta) J_1(\beta) \frac{\frac{2(\omega_L - \omega_0)}{\Delta\omega_c}}{1 + \left(\frac{2(\omega_L - \omega_0)}{\Delta\omega_c}\right)^2} \tag{4.28}$$

The equation above has a maximum value V_{max} when $\omega_L - \omega_0 = -\Delta\omega_c/2$ and a minimum value V_{min} when $\omega_L - \omega_0 = \Delta\omega_c/2$. The maximum and minimum values are given by

$$\begin{aligned} V_{max} &= RGAE_0^2 J_0(\beta) J_1(\beta) \\ V_{min} &= -RGAE_0^2 J_0(\beta) J_1(\beta) \end{aligned} \tag{4.29}$$

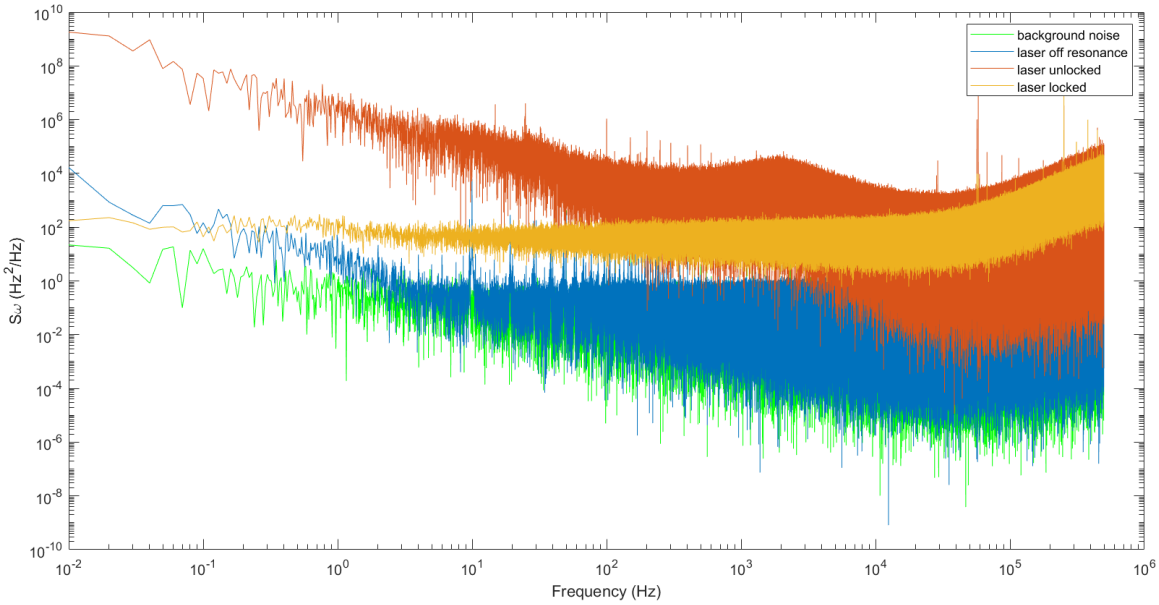

Figure 4.7: Power spectral density of the frequency fuctuations when the laser is locked (yellow trace), unlocked (red trace), and out of resonance (blue trace).

Therefore, the equation in 4.3.1 can be rewritten as

$$S_v(\Omega) = (V_{max} - V_{min})^2 \frac{4}{\Delta\omega_c^2} \frac{1}{1 + \left(\frac{2\Omega}{\Delta\omega_c}\right)^2} S_\omega(\Omega) \tag{4.30}$$

Here, $V_{max} - V_{min}$ is measured to be approximately 0.1285 V, and $\Delta\omega_c = 2\pi \times 14$ kHz. Figure 4.7 shows the power spectral density of the frequency fluctuations when the laser is locked, unlocked and out of resonance. To obtain the linewidth of the clock laser, we take the case where the deviation of the noise in frequency is small compared to the bandwidth of the noise ($\Omega \sim 0$), where the S_ω is independent of the frequency Ω. The width at half maximum of the Lorentzian optical spectrum $\Delta\omega$ is equal to the power spectral density of the frequency fluctuations S_ω^0, which is determined by taking the average of S_ω in low frequency region (0.01 Hz to 0.1 Hz). Since $\Delta\omega = 2\pi\Delta\nu$, in the frequency unit (Hz), we obtain $\Delta\nu = S_\omega/(2\pi)$. Therefore, the linewidth of our clock laser is estimated to be 17 Hz.

4.3.1.3 Fiber Doppler Noise Cancellation

When an optical signal with narrow linewidth, such as clock laser, passing through an optical fiber, it introduces a broadening to the linewidth of the laser. This is because the fiber's insertion phase is sensitive to the environmental perturbation, such as vibration and temperature. For instance, the linewidth of a Hz-level clock laser can be broadened to hundreds of Hertz when travelling through a 25 m fiber [95]. In this case, a Doppler noise cancellation system is necessary to address this problem. In our clock laser system, two Doppler noise cancellation systems are required: one for the fiber that

connects the master laser to the slave laser and the other for the fiber linking the slave laser to the experimental setup.

The Doppler Cancellation Module (DCM) for the master laser is a commercial module that takes the optical beating signal between the reference and the beam passing back and forth in the fiber to generate an error signal. The optical path generating the beat signal is depicted in Figure 4.8. The yellow path represents the optical layout for both the incoming and back-reflected beams. In the incoming path, the optical signal passes through a Faraday Rotator and an AOM (+40 MHz) before entering a 10-meter fiber. The Faraday Rotator rotates the polarization of the retro-reflected beam by 90° before it joins the referenced beam at the fiber coupler for Doppler cancellation. A double-pass AOM after the fiber output, labeled as "AOM1" in Figure 4.6, is employed to appropriately shift the frequency of the master laser for the clock transition. The zero-order of after modulation is reflected back to create the beat signal with the reference beam for locking purposes. The reference beam for beating is depicted in green. After amplification, the optical beat signal obtained by photodetector is mixed with an 80 MHz radio frequency generated by a direct digital synthesizer (DDS) referenced by a 10 MHz RF from the Rubidium (Rb) clock. This error signal is fed into the PID module and feedback on the 40 MHz AOM to cancel out the fiber noise. The comparison of the beating signal with and without Doppler noise cancellation is depicted in Figure 4.9. The blue curve is the beating signal without the Doppler cancellation lock, which gives a linewidth of (1.9±0.1) kHz. In comparison, the beating signal with the lock gives a linewidth lower than 10 Hz, and this value is limited by the reading bandwidth of our spectrum analyzer.

The optical layout for the fiber transporting the slave laser to experimental table is illustrated in Figure 4.6. After being frequency-shifted to the resonance of clock transition, the master laser is employed to inject into a diode laser, providing a higher power clock laser for the experiment. This laser is then directed to the main setup by another 10-meter-fiber, indicating that a fiber noise cancellation is also required. The AOM1 shown in Figure 4.6 is utilized to fine-tune the frequency of clock laser to match the clock transition frequency. After injected by the master laser, the main beam is directed through AOM2, which is driven by a voltage-controlled oscillator (VCO), employed for the feedback of Doppler noise cancellation. To generate the beating signal, a non-PBS (R:T=10:90) is positioned before AOM2. One of the beat branches traverses the AOM and fiber, reflects off the polarization-maintaining (PC) fiber, retraces the same path, and combines with the reference beam. The reference beam is obtained from the reflection of the non-PBS and a mirror. This beating signal is then fed into the PID module, with its output linked to the VCO of AOM2 for implementing fiber Doppler noise cancellation. An additional AOM3 is placed after the fiber output to shift the clock laser frequency in the opposite order compared to AOM2. This serves a dual purpose of clock laser switching and compensating for detuning introduced by AOM2 during the Doppler lock process.

The performance of the Doppler lock for the path from slave laser to experimental table is illustrated in Figure 4.6. The blue curve represents the beat signal without lock, where the AOM is fed by a VCO with a fixed value, while the red curve is the beat signal with Doppler lock. The RF signal without

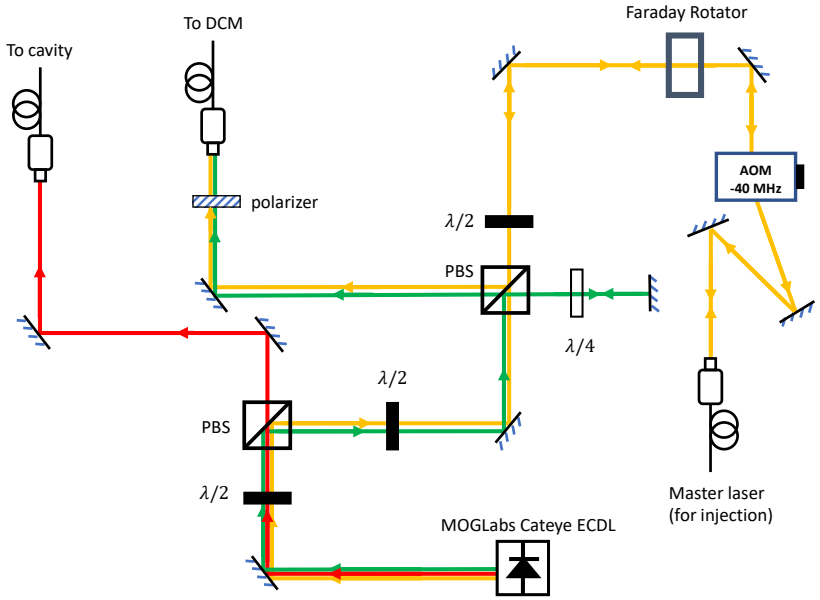

Figure 4.8: Optical schematic of Doppler noise cancellation for the fiber bringing master to slave laser table. The yellow lines show the incoming and back-reflection path for the beating, and the reference path is shown in green. The reference beam and back-reflection beam are sent to the Doppler cancellation module to generate the beating signal for the fiber noise cancellation. The red path is the beam for the cavity lock.

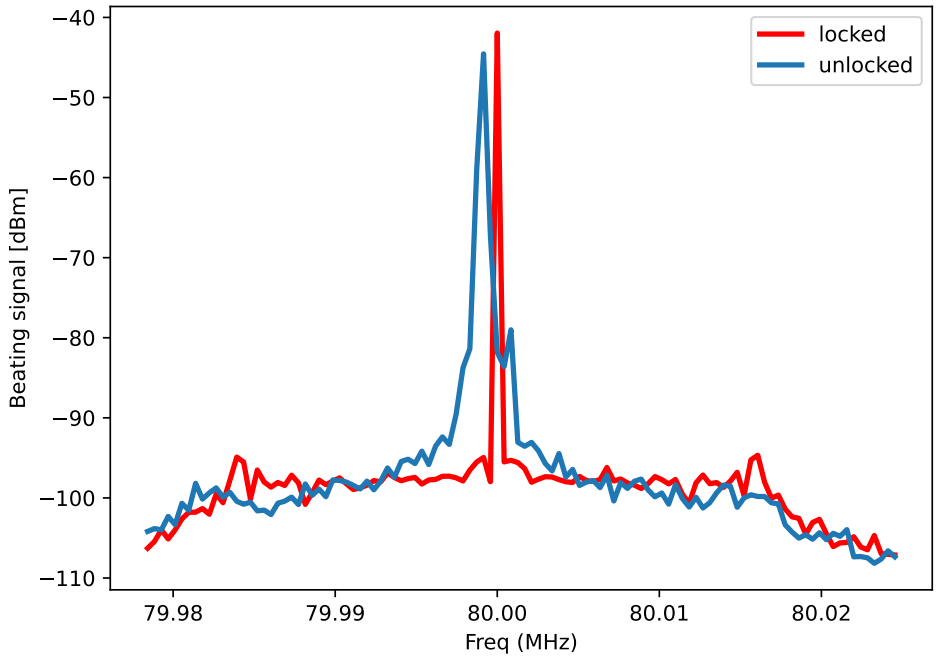

Figure 4.9: Beating signal comparison between with and without Doppler cancellation lock for the fiber bringing master laser to slave laser.

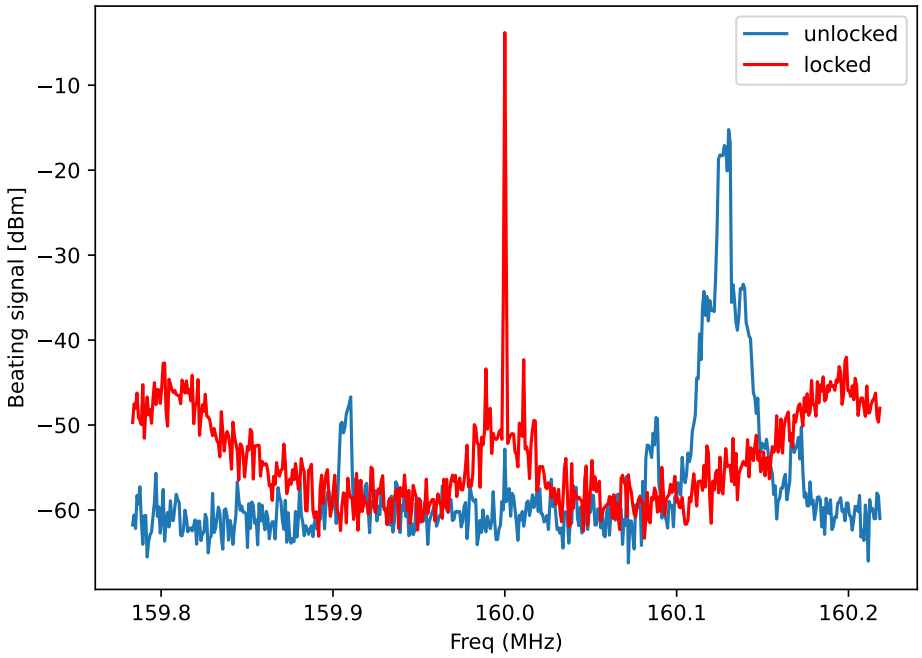

Figure 4.10: Beating signal comparison between with and without Doppler cancellation lock from slave laser to the experimental table.

lock is given by the VCO with a fixed value, which is not exactly at 80 MHz, so the beating signal without lock is not centered at 160 MHz. Compared to the (22.9±0.8) kHz for the linewidth of the unlocked case, we obtain a linewidth below 10 Hz of the linewidth with the Doppler cancellation lock, constrained by the data collection bandwidth.

4.3.2 Mixing magnetic field

In ^{87}Sr, the clock transition is allowed because of the hyperfine mixing, due to the zero nuclear spin [71]. Conversely, in bosonic strontium-88 the clock transition is forbidden. To enable the clock transition in ^{88}Sr, a magnetic field is applied to induce coupling between ^{3}P0 and ^{3}P1 ([47, 65]). The switching of the mixing coil, similar to the MOT coil switching discussed in Section 3.4.1, is accomplished using IGBTs. The power supply for the mixing coil typically provides a current of 105 A, providing in a magnetic field of approximately 80 G at the position of the atomic samples. CNY65 optocouplers are used to drive the IGBTs. Additionally, a diode (part no. DSEI2X101-12A) is incorporated to prevent reverse current flow. To dissipate the magnetic field energy effectively during switch-off, a transient-voltage-suppression (TVS) diode (part no. 1.5KE480CA) is incorporated. The "spectroscopy PSU" part shown in Figure 4.11 depicts the circuit with low current to generate the bias field for the red spectroscopy check. The IGBT and TVS diode for the mixing coil switching circuit are also placed at the cooling plate, as depicted in Figure 3.16.

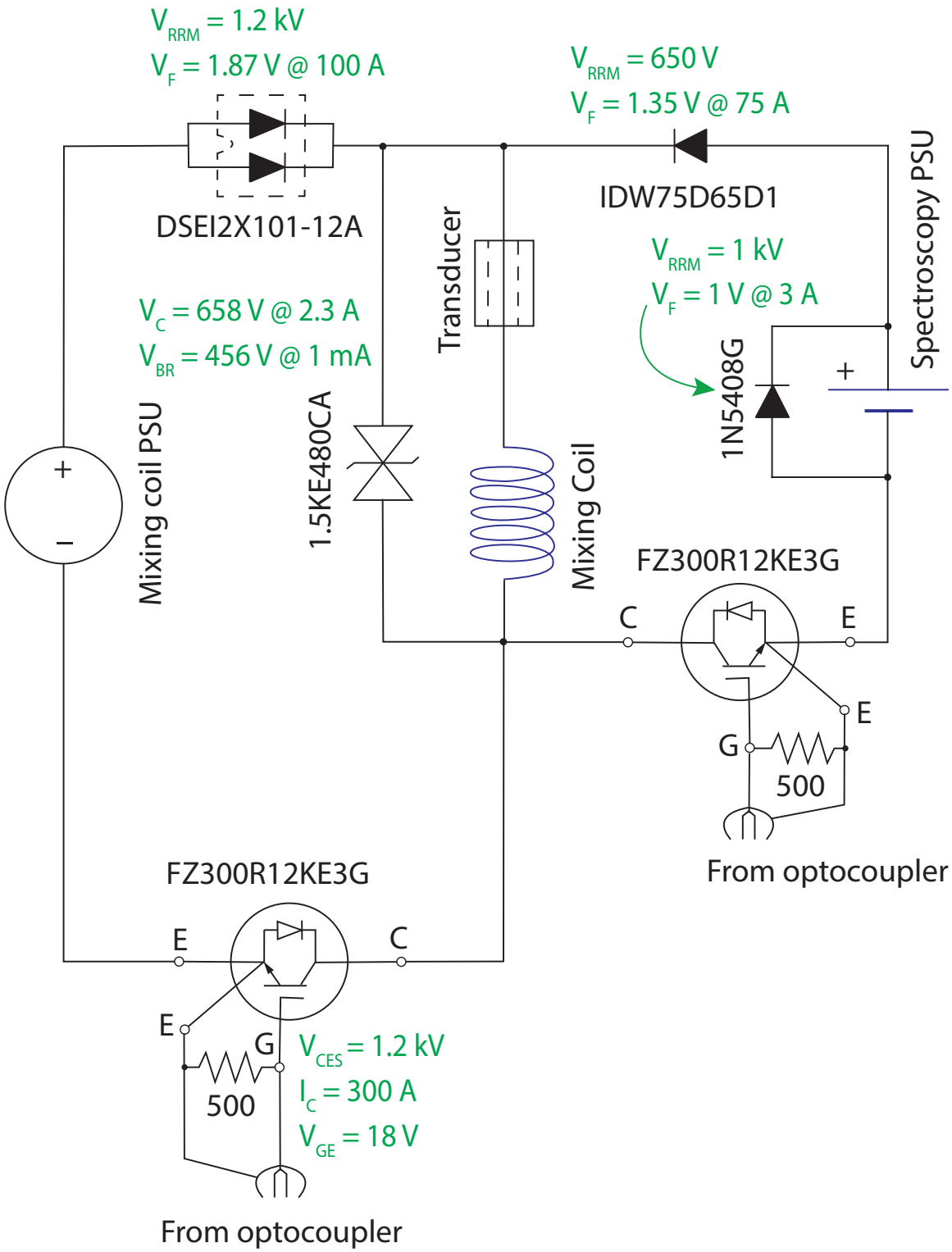

Figure 4.11: Schematic of mixing coil switching circuit. The current is switched by the IGBT, and the IGBT is driven by the optocoupler. The diodes are added to prevent the reverse direction current. The spectroscopy circuit is used to apply the low current (about 1 A) on the coils to calibrate the spectroscopy on $^1S_0$ to $^3P_1$.

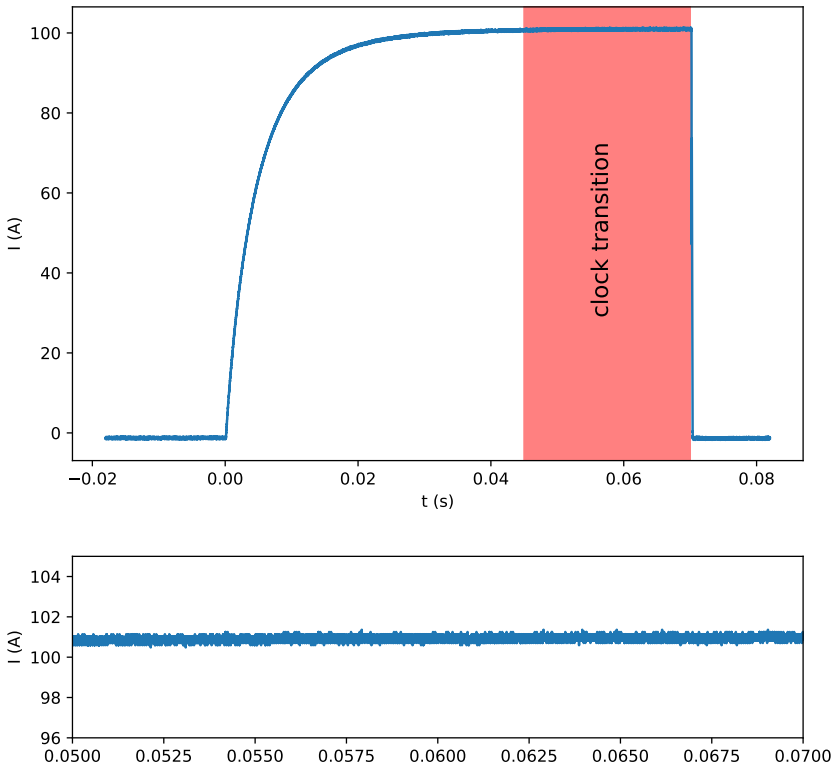

Figure 4.12: The switching behavior of the mixing coil monitored by the transducer during the interrogation of clock transition. The current in the mixing coil stabilizes after 45 milliseconds, with a peak-to-peak fluctuation of approximately 0.8 amperes. Once the current stabilizes, the clock transition, highlighted in red, is initiated. The bottom figure is zoomed on the current during the clock transition stage.

Moreover, a transducer is added to monitor the current flowing in the coils. The switching behavior during the clock transition of the mixing coils is depicted in Figure 4.12. The current flowing in the mixing coils stabilizes after 45 ms, after which the peak-to-peak fluctuation in the coils is down to 0.8 A. Further details regarding the clock transition sequence with this switching behavior are discussed in section 4.3.3.

4.3.3 Spectroscopy on clock transition

The clock transition in strontium-88 is strictly forbidden due to the zero nuclear spin. Although other approaches such as using twisted-light, two-photon and three-photon processes have been proposed and studied [49, 51, 97, 98, 99], the only known achieved strategy to enable the clock transition in bosonic strontium-88 so far is the so-called magnetically-induced spectroscopy [47, 65]. In this technique, a mixing field is applied to mix the states $^3P_0$ and $^3P_1$ and enable the transition. This process can be derived using perturbation theory. The Hamiltonian of an atom in a static magnetic field is given by

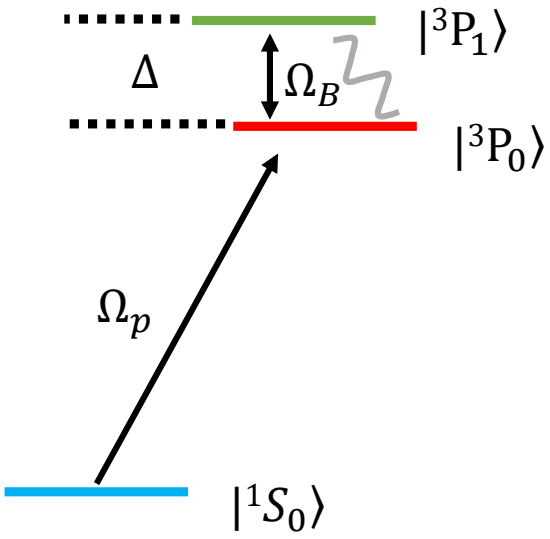

Figure 4.13: Magnetically-induced spectroscopy scheme. An extra magnetic field is applied to induce the coupling Ω_B between the state $^3\mathrm{P}_0$ and $^3\mathrm{P}_1$, which enables the transition from $^1\mathrm{S}_0$ to $^3\mathrm{P}_0$. Δ is the frequency splitting between $^3\mathrm{P}_0$ and $^3\mathrm{P}_1$, and Ω_P is the single photon Rabi frequency.

$$H = H_a - \vec{\mu} \cdot \vec{B} \tag{4.31}$$

where H_a is the unperturbed Hamiltonian, and $\vec{\mu} = \mu_B(g_l\vec{L} + g_s\vec{S})$ with $g_l = 1$ and $g_s \approx 2$. According to the perturbation theory, the state with the first order correction is given by

$$|^3P_0'\rangle = |^3P_0\rangle + \sum_{\psi} \frac{\langle\psi|\vec{\mu}\cdot\vec{B}|^3P_0\rangle}{\hbar\Delta_\psi} \tag{4.32}$$

The sum is over all possible states ψ, which is dominated by $|^3P_1, m_j = 0\rangle$ in the same fine triplet; Δ_ψ is the frequency splitting between ψ and $^3P_0$. Decompose the states $^3P_1$ and $^3P_0$ into eigenstates of $\vec{L} = 1$ and $\vec{S} = 1$ [100]:

$$\begin{aligned} |^3P_1,\ m_j = 0\rangle &= \sqrt{\frac{1}{2}}|1,-1\rangle_{m_s,\ m_l} - \sqrt{\frac{1}{2}}|-1,1\rangle_{m_s,\ m_l} \\ |^3P_0,\ m_j = 0\rangle &= \sqrt{\frac{1}{3}}|1,-1\rangle_{m_s,\ m_l} - \sqrt{\frac{1}{3}}|0,0\rangle_{m_s,\ m_l} + \sqrt{\frac{1}{3}}|-1,1\rangle_{m_s,\ m_l} \end{aligned} \tag{4.33}$$

Then second term is calculated to be

$$\langle^3P_1|\vec{\mu}\cdot\vec{B}|^3P_0\rangle \approx \sqrt{\frac{2}{3}}\mu_B|\vec{B}| = \hbar\Omega_B \tag{4.34}$$

The state with the presence of the static magnetic field can be expressed by [47]

$$|^3P_0'\rangle = |^3P_0\rangle + \frac{\Omega_B}{\Delta}|^3P_1\rangle \tag{4.35}$$

where Δ is the frequency splitting between $|^3P_1\rangle$ and $|^3P_0\rangle$. To address the clock transition with the presence of mixing field, a resonant probe beam is applied with the polarization parallel to the

magnetic field. The Rabi frequency can be calculated with

$$\Omega_{clock}/2\pi \approx \frac{\Omega_B \Omega_p}{2\pi\Delta} = \alpha|\vec{B}|\sqrt{I_p} \tag{4.36}$$

where $\vec{B}$ and I_p are the mixing field and probe laser intensity respectively; Ω_p is the single photon Rabi frequency; $\alpha = \sqrt{\frac{2}{3}}\frac{d\mu_B\sqrt{\epsilon_0 c}}{2\pi\Delta\hbar^2} \propto (\Gamma_{^1S_0\rightarrow{}^3P_1})^{1/2}$ (d is the dipole moment, and Δ is the single-photon detuning) is the factor gathering the constants, with α=6.26 Hz/(mT$\sqrt{\mathrm{W}\cdot\mathrm{cm}^{-2}}$) [101].

In the implementation of magnetically-induced-spectroscopy, atoms are initially loaded into the 1D optical lattice operating at 813.427 nm for a duration of 20 ms to clear out the unloaded atoms from the red MOT. Subsequently, the mixing field is turned on, taking approximately 45 ms to stabilize, as shown in Figure 4.12. Once the mixing field stabilizes, the clock laser is turned on to address the clock transition. The clock transition is addressed with a mixing field of 80 G and a probe beam intensity of 50 W/cm^2. The magnetic field and laser intensity theoretically provides a peak Rabi frequency of 360 Hz. During the interrogation of clock transition, the peak to peak fluctuation of current flowing on mixing coils measured by the tranducer is about 0.8 A. This gives a magnetic field fluctuation of 0.6 G and a Rabi frequency fluctuation of 2.4 Hz, which is adequately stable for our experiment when compared to the targeted Rabi frequency of 360 Hz.

For the detection stage, an on-resonance probe beam operating at 461 nm is applied to the atomic sample and retro-reflected to capture the fluorescence signal from the ground state ^{1}S$_0$ while simultaneously pushing away the ground state atoms. Following this step, the repump beams are employed to bring the atoms in excited clock state from ^{3}P$_0$ back to ^{1}S$_0$. Subsequently, another detection with the blue probe is performed to determine the number of atoms in the ^{3}P$_0$ state.

The existence of the mixing magnetic field and clock laser induce the second-order Zeeman effect and ac Stark shift of clock transition, which is given by [47][102]

$$\begin{aligned}\hbar\Delta\nu_B^{(2)} &= \sum_{\psi}\frac{\left|\langle\psi|\vec{\mu}\cdot\vec{B}|^3P_0\rangle\right|^2}{\hbar\Delta_\psi}\\ \hbar\Delta\nu_p &= \frac{1}{2}\Delta\alpha E^2,\end{aligned} \tag{4.37}$$

where $\Delta\alpha$ is the differential polarizability between ground and excited states. Inserting the parameters for clock transition in strontium-88, the shifts are rewritten as[101]:

$$\begin{aligned}\Delta\nu_B^{(2)}/\nu_0 &= \left(\frac{B}{1\ \mathrm{mT}}\right)^2 \times \left(-5.47(5)\times10^{-14}\right)\\ \Delta\nu_p/\nu_0 &= \left(\frac{I_p}{1\ \mathrm{W/cm^2}}\right) \times \left(-6.6\times10^{-14}\right)\end{aligned} \tag{4.38}$$

The population distribution between the ground and excited states during the clock transition can be adjusted by modifying the pulse duration. The Rabi oscillation between the ^{1}S$_0$ and ^{3}P$_0$ states is depicted by the blue dots in Figure 4.14. As we will elaborate in Section 4.3.4, the damping observed in the oscillation is primarily due to the power broadening of the clock laser, which results in a range of Rabi frequencies within the atomic sample. The simulation with this effect is illustrated by the orange curve in Figure 4.14.

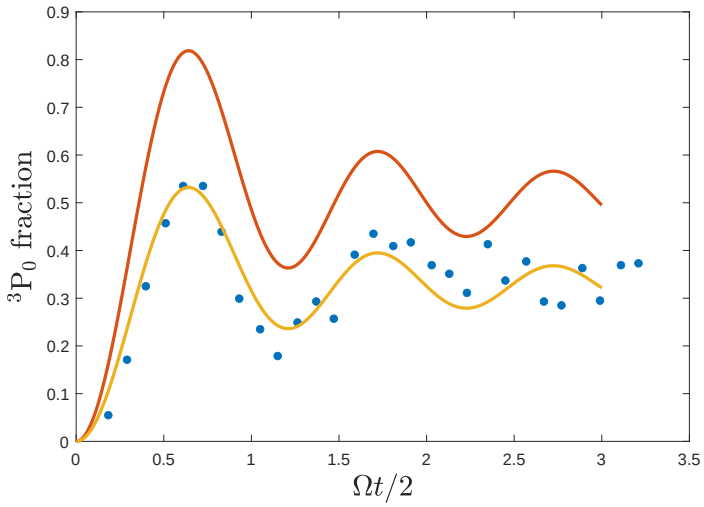

Figure 4.14: Comparison between simulation and experimental data: the orange curve is the simulation result considering that the Gaussian profile of the clock laser gives the inhomogeniety of the Rabi frequency in the cloud. The blue dots show the experimental data. The parameters in the simulation are taken according to the experiment: Rabi frequency $\Omega = 360$ Hz, atomic cloud waist is 50 μm, clock laser waist $\omega_0 = 100$ μm. The yellow curve is the simulation result multiplied by a constant $a = 0.65$.

4.3.4 Damping of the Rabi oscillation

In this section, I will model the primary factors contributing to the damping of the Rabi oscillation. The beam size of the clock laser being comparable to the size of the atoms can result in a Rabi frequency distribution due to the intensity distribution of the beam over the atomic cloud. It's worth noting that in this analysis, the finite temperature of the atoms is not taken into account since they are trapped in the Lamb-Dicke regime where Doppler shifts are insignificant. Additionally, as the excited clock state is metastable state with a significantly longer lifetime compared to the interrogation time, any decay in this process is considered negligible.

In our experimental system, the clock laser is propagating at the same direction as one of the horizontal lattices (y-axis). The atomic sample has a size which is much smaller than the Rayleigh length of the clock laser and should be well located at the focus of the clock laser. In this case, the intensity of the clock laser experienced by the atom at the position (x, z) is given by

$$I(x, z) = I_0 \exp\left[-\frac{2(x^2 + y^2)}{\omega_0^2}\right] \tag{4.39}$$

where I_0 and ω_0 are the peak intensity and waist of the clock laser. Since the Rabi frequency is proportional to the square-root of the clock laser intensity, we have

$$\Omega(x, z) = \Omega_0 \exp\left[-\frac{(x^2 + z^2)}{\omega_0^2}\right] \tag{4.40}$$

where Ω_0 is the peak Rabi frequency. We consider that the atomic ensemble with a total number of

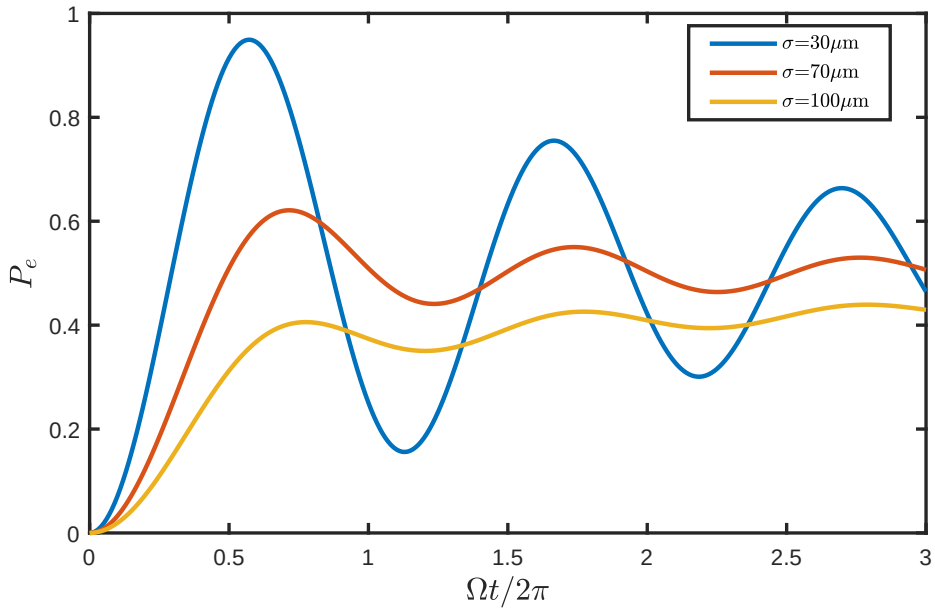

Figure 4.15: Comparison of the averaged Rabi flopping signal for different values of cloud size with a clock beam waist of 100 μm.

atoms N has a Gaussian density distribution

$$\rho(x,y,z) = \frac{N}{(2\pi\sigma^2)^{3/2}} \exp\left[-\frac{(x^2+y^2+z^2)}{2\sigma^2}\right] \tag{4.41}$$

where σ is the RMS size of the atomic sample. As discussed in Section 2, the excited state population can be expressed by

$$P_e = \left(\frac{\Omega}{\bar{\Omega}}\right)^2 \sin^2\left(\frac{\bar{\Omega}t}{2}\right) \tag{4.42}$$

where $\bar{\Omega} = \sqrt{\Omega^2+\delta^2}$ is the generalized Rabi frequency, and δ is the detuning of the clock laser. Due to the Gaussian profile of the clock transition, we need to average over the atomic spatial distribution:

$$P_e(t) = \frac{1}{N}\int\int\int \rho(x,y,z)\left[\frac{\Omega(x,z)}{\bar{\Omega}(x,z)}\right]^2 \sin^2\left[\frac{\bar{\Omega}(x,z)t}{2}\right] \mathrm{d}x\mathrm{d}y\mathrm{d}z \tag{4.43}$$

Integrating along the clock beam propagation axis y with a range $\sigma \ll y_R$:

$$P_e(t) \approx \frac{1}{2\pi\sigma^2}\int\int \exp\left[-\frac{(x^2+z^2)}{2\sigma^2}\right]\left[\frac{\Omega(x,z)}{\bar{\Omega}(x,z)}\right]^2 \sin^2\left[\frac{\bar{\Omega}(x,z)t}{2}\right] \mathrm{d}x\mathrm{d}z \tag{4.44}$$

Here, we consider the resonant case, this expression can be reduced to:

$$P_e(t) = \frac{1}{2\pi}\int\int \exp\left[-\frac{(\tilde{x}^2+\tilde{z}^2)}{2}\right] \sin^2\left[\frac{\tilde{\Omega}(\tilde{x},\tilde{z})t}{2}\right] \mathrm{d}\tilde{x}\mathrm{d}\tilde{z} \tag{4.45}$$

where $\tilde{x} = x/\sigma$, $\tilde{x} = x/\sigma$ and $\tilde{\omega_0} = \omega_0/\sigma$. The Rabi frequency can be written as

$$\tilde{\Omega}(\tilde{x},\tilde{z}) = \Omega_0 \exp\left[-\frac{(\tilde{x}^2+\tilde{z}^2)}{\tilde{\omega_0}}\right] \tag{4.46}$$

Figure 4.15 shows the simulation for averaged Rabi oscillation with different values of the cloud size, where we can observe a more severe damping with larger cloud size. The clock laser beam waist is fixed at 100 μm in this simulation.

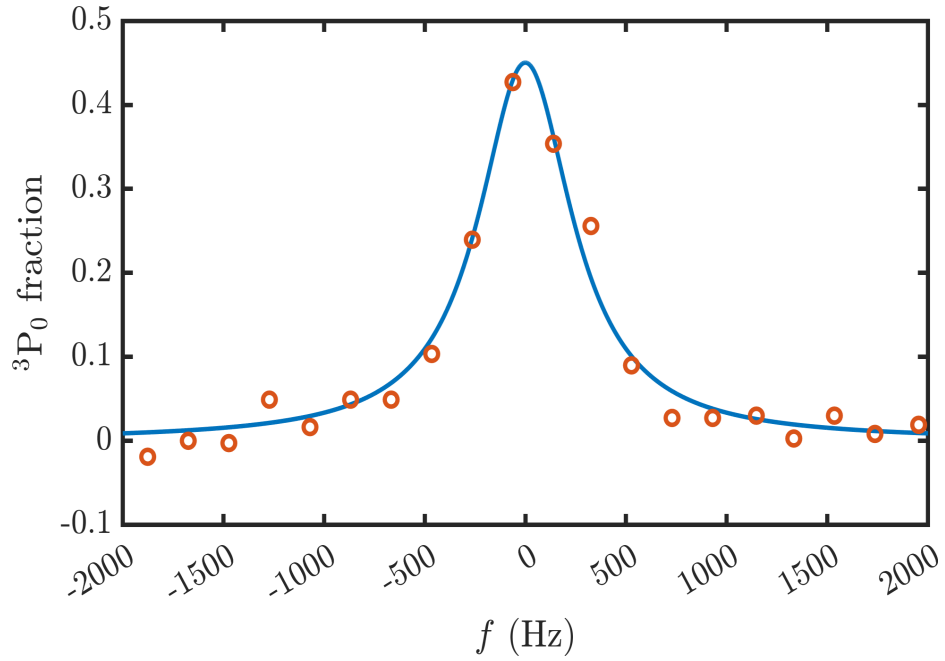

Figure 4.16: Magnetically-induced spectroscopy of clock transition. The experimental data is shown in orange circle, and the blue curve is the Lorentzian fitting, where a width of Γ=(607.8±25.6) Hz is observed.

The comparison between the experimental data and simulation result is shown in Figure 4.14. In the simulation, the peak Rabi frequency is set at 360 Hz, determined by the magnetic field and beam power applied in the system. The waist of atomic cloud and clock laser are measured experimentally as 50 μm and 100 μm respectively. However, the amplitude of the experimental data appears smaller compared to the simulation curve. This might be attributed to the time gap between the detection of ground and excited states, , where the loss of excited state atoms could contribute to this difference. Therefore, the yellow curve in Figure 4.14 shows the simulation result multiplied by a constant value $a = 0.65$. From the results illustrated in Figure 4.14, we can observe a good agreement of the damping and the period of the oscillation between the simulation and experiment. It indicates that the inhomogeneous broadening due to the beam size might be the main mechanism at decay.

4.3.5 Clock transition spectrum

The temperature of the atomic source in red MOT is approximately 1 μK, resulting in a Doppler broadening of 60 kHz. This is much larger than the linewidth of the clock transition. In order to eliminate this Doppler broadening during the clock transition, the atoms are loaded into an one-dimensional optical lattice operating at the magic-wavelength after cooled and captured in red MOT. The clock laser is overlapped with one of the horizontal lattice beams via a dichroic concave mirror.

The spectroscopy of the clock transition is presented in Figure 4.16. The interrogation time set for the clock transition is 30 ms, after which the atoms are prepared in a statistical mixture of ground and

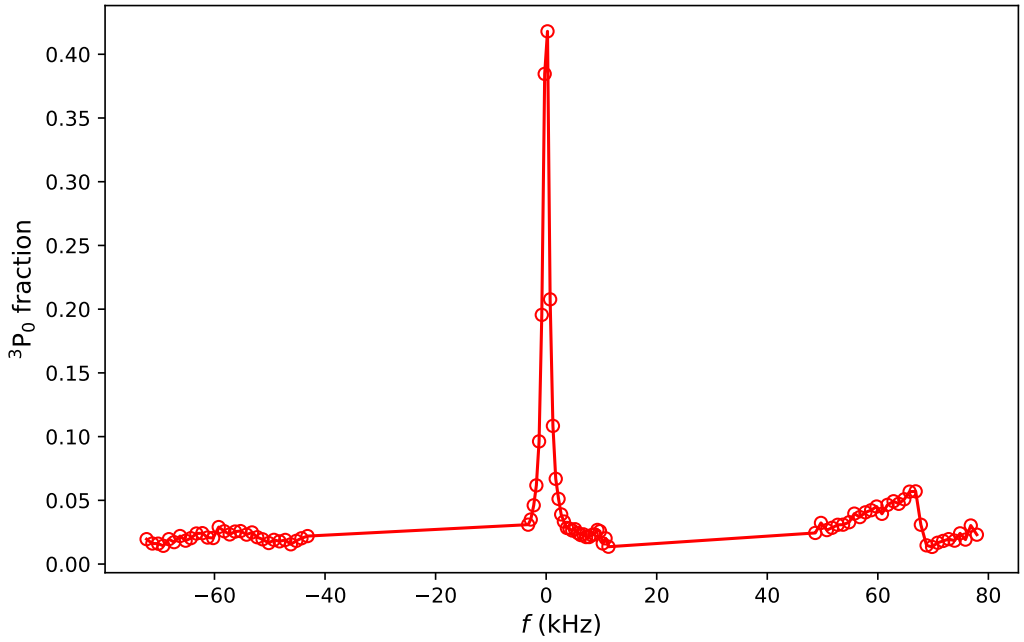

Figure 4.17: Clock transition spectroscopy in the 1D optical lattice. The sideband transition signal gives a trapping frequency around 65 kHz. The clock laser is turned on for 30 ms.

excited clock states. The data is fitted with a Lorentzian function $L(f) = \text{offset} + A \cdot \frac{\Gamma/2}{(f-f_0)^2+(\Gamma/2)^2}$, where a width Γ=(607.8±25.6) Hz is observed. The observed broadening is primarily attributed to the varied ac Stark shift generated by the Gaussian profile of the clock beam.

As discussed in Section 4.2, a concave mirror is utilized to retro-reflect the incoming lattice beam and create a standing wave, which generates the periodic trapping potential to trap the atoms. We use a focused Gaussian beam to describe the lattice laser:

$$\vec{E}(r,z) = \vec{E}_0 \frac{\omega_0}{\omega(z)} \exp(-\frac{r^2}{\omega^2(z)}) \exp(-ikz), \tag{4.47}$$

where $\vec{E}_0$ is the field at the focal point; $\omega(z) = \omega_0\sqrt{1+(z/l_R)^2}$ with the Rayleigh length $l_R = \frac{\pi\omega_0^2}{\lambda}$; $\omega_0 \equiv \omega(0)$ is the waist radius. With this, the electric field of the lattice can be expressed by

$$\begin{aligned} \vec{E}_{\text{lattice}} &= \vec{E}(r,z) + \vec{E}(r,-z) \\ &= 2\vec{E}_0(r,z) \exp(-\frac{r^2}{\omega^2(z)}) \cos(kz), \end{aligned} \tag{4.48}$$

And the trapping potential of the lattice is

$$U_{\text{lattice}} = -U_0 \exp\left(\frac{-2r^2}{\omega_0}\right) \cos^2(kz) \tag{4.49}$$

where $U_0 = 4\alpha_n P/\pi\epsilon_0 c\omega_0^2$ is the trap depth, α_n is the atomic polarizability, P is the laser beam power. The trap depth is dependent on the power of lattice beam, which can be regarded as harmonic when

$U_0 \gg k_B T$. The trapping frequencies are the relevant parameters to characterize the optical lattice. The axial and radial trapping frequencies can be calculated by $\omega_z^2 = \frac{1}{m}\frac{\partial^2 U_{\text{lattice}}}{\partial z^2}$ and $\omega_r^2 = \frac{1}{m}\frac{\partial^2 U_{\text{lattice}}}{\partial r^2}$ at the focal position:

$$\omega_z = \sqrt{\frac{2k^2 U_0}{m}} = 2\sqrt{\frac{U_0 \omega_{rec}}{\hbar}};\ \omega_r = \sqrt{\frac{4U_0}{m\omega_0^2}}, \tag{4.50}$$

where $\omega_{rec} = \hbar k^2/2m$ is the recoil frequency of the lattice.

Consider the clock transition in optical lattice, the interaction Hamiltonian in a rotating frame with rotating wave approximation can be written as [103]

$$H_{int} = \frac{\hbar\Omega}{2} e^{ik\hat{z}} |e\rangle\langle g| + h.c., \tag{4.51}$$

when the atoms are trapped in a harmonic potential with $\hat{z} = \sqrt{\frac{\hbar}{2m\omega_z}}(\hat{a} + \hat{a}^\dagger)$, where $\hat{a}$ and $\hat{a}^\dagger$ are the annihilation and creation operators. Then the interaction part in the Hamiltonian is rewritten as

$$H_{int} = \frac{\hbar\Omega}{2}(e^{i\eta(\hat{a}+\hat{a}^\dagger)}|e\rangle\langle g| + h.c.), \tag{4.52}$$

where $\eta = \sqrt{\omega_{698,rec}/\omega_z}$ is the Dicke parameter. Analogous to the two-level system we discussed in Chapter 2, the Rabi frequency can be defined as [103]

$$\frac{\hbar\Omega_{eg}}{2} = \langle e,\ n_e|H_{int}|g,\ n_g\rangle = \frac{\hbar\Omega}{2}\langle n_e|e^{-i\eta(\hat{a}+\hat{a}^\dagger)}|n_g\rangle, \tag{4.53}$$

where n_e and n_g are the motional state in lattice associated with excited ($|e\rangle$) and ground ($|g\rangle$) states. The Rabi frequency is given by [104]

$$\Omega_{eg}(n_e, n_g) = \Omega e^{-\eta^2/2}\sqrt{\frac{n_<!}{n_>!}}\eta^{|n_e - n_g|} L_{n_<}^{|n_e - n_g|}(\eta^2), \tag{4.54}$$

where $n_<$ and $n_>$ are the lesser and greater of the two motional states; and $L_j^\alpha(x)$ is the jth generalized Laguerre polynomial. The Hamiltonian with the resolved sideband transition can be written as

$$H = \hbar\begin{pmatrix} -\Delta + \omega_z(n_e - n_g) & \Omega_{eg}(n_e, n_g)/2 \\ \Omega_{ge}(n_e, n_g)/2 & 0 \end{pmatrix}, \tag{4.55}$$

The states basis of the system are $|g\rangle \otimes |n_g\rangle$ and $|e\rangle \otimes |n_e\rangle$. Therefore, the excitation probability can be expressed by [103]

$$P_{e,n_e} = \frac{|\Omega_{eg}|^2}{|\Omega_{eg}|^2 + [\Delta - \omega_z(n_e - n_g)]^2}\sin^2\left(\frac{t}{2}\sqrt{|\Omega_{eg}|^2 + [\Delta - \omega_z(n_e - n_g)]^2}\right) \tag{4.56}$$

When $n_e = n_g$, the equation above expresses the transition within the same motional state, the Hamiltonian and excitation probability of which are reduced to the two-level system described in section 2.2.3. In cases where $n_e \neq n_g$, the expression above indicates that the sideband transitions occur when the detuning $\Delta = \omega_z$ for $n_e - n_g = \pm 1$. The experimental findings regarding this are depicted in Figure 4.17. Based on the spectroscopy of sideband transition, the trapping frequency for the optical lattice is approximately (65±0.5) $kHz. In our experimental setup, we apply the lattice laser with a power of 1\ W and beam waist of 80\ \mu$m, which theoretical gives a trapping frequency of 70 kHz according to the expression in Equation 4.50.

Discrepancies between the experimental and theoretical values could stem from power losses in the optical path and through the viewport. Besides, deviations from an ideal Gaussian profile in the transverse profile induced by the optical path might influence the trapping frequency.

Additionally, from the sideband spectroscopy of the clock transition, we can obtain the mean occupation of the atoms in motional states [105]:

$$\bar{n} = \frac{A_{\mathrm{rsb}}}{A_{\mathrm{bsb}} - A_{\mathrm{rsb}}} = 0.51 \tag{4.57}$$

where A_{rsb} and A_{bsb} is the amplitude of the first red sideband and first blue sideband. The averaged occupation of the atoms can be expressed as [101]

$$\bar{n} = \frac{\sum_{n_i} n_i e^{-\frac{n_i \hbar\omega}{k_B T}}}{\sum_{n_i} e^{-\frac{n_i \hbar\omega}{k_B T}}} = \frac{1}{e^{-\frac{\hbar\omega}{k_B T}} - 1}. \tag{4.58}$$

Therefore, from the occupation, the temperature of the atoms is calculated to be 550 nK. This value is close to the temperature we measured with time-of-flight strategy.

The sideband broadening illustrated in Figure 4.17 is attributed to the anharmonicity of the motion. Typically, the atomic motion within an optical lattice is perceived as harmonic when considering only axial motion, neglecting radial movement. The observed broadening and asymmetry stem from atoms within the optical lattice exhibiting classical motion in the radial direction, where $\hbar\omega_r \gg k_B T_r$. As atoms radially oscillate, they experience varying axial trap frequencies due to the dependence of trap intensity on their radial position. For detailed theoretical insights, references [103][106] provide further exploration on this topic.

4.4 Bragg Diffraction

In our dual atom interferometer setup, we utilize a moving lattice operating at 813.427 nm ($f_{\mathrm{magic}} =$ 368554.58(28) GHz [68][69]) to implement Bragg diffraction. The Bragg diffraction technique serves dual purposes: velocity selection and interferometric pulses. This section focuses on the calibration process of Bragg diffraction in our experimental system.

4.4.1 Frequencies involved in the Bragg pulse sequence

The atoms are initially in the momentum state $|p_i = a\hbar k\rangle$, where k is the wavenumber of the Bragg beam, a is the real number. Here we consider Bragg pulse that transfers the atoms between $|p_i = a\hbar k\rangle$ and $|p_f = (a+2)\hbar k\rangle$. In this case, we need a angular frequency difference of

$$\begin{aligned} \Delta\omega_a &= \frac{1}{\hbar}\frac{p_f^2 - p_i^2}{2m} \\ &= \left[(a+2)^2 - a^2\right]\frac{\hbar^2 k^2}{2m} \\ &= (4a+4)\frac{\hbar^2 k^2}{2m} \end{aligned} \tag{4.59}$$

where m is the atomic mass, ω_r is the recoil angular frequency of the Bragg beam.

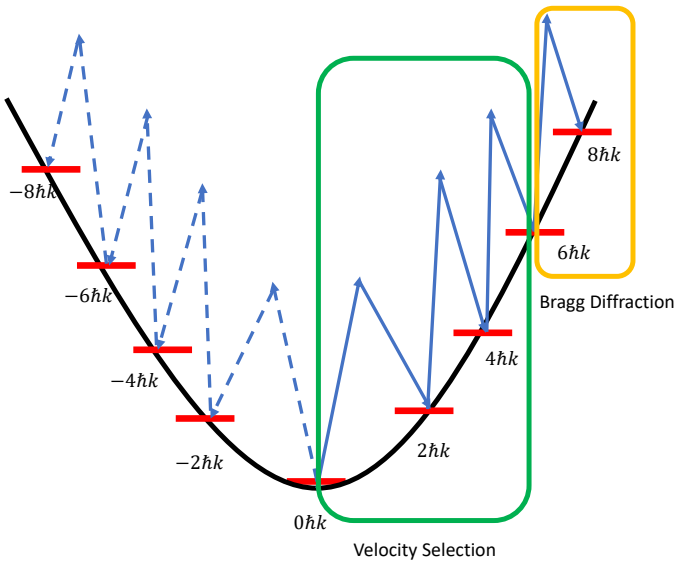

Figure 4.18: Bragg pulse scheme for velocity selection and demonstration of atom interferometer. During the velocity selection phase, three first-order on-resonant Bragg pulses are applied to transfer the atoms with low temperature from 0 momentum state to 6$\hbar$k state. The last Bragg pulse is applied to interrogate the momentum state transition between 6$\hbar$k and 8$\hbar$k for the pulses in atom interferometer.

During the Bragg diffraction pulses, as the atomic sample is in free space and falling, it experiences a frequency shift in the pulses caused by the Doppler effect. Therefore, in order to compensate the effect, we chirp the frequency of the pulses with a rate of

$$\alpha = k_{\text{eff}} \cdot g \approx 24 \text{ kHz/ms} \tag{4.60}$$

where $k_{\text{eff}} = 2k$ is the effective wavenumber of the Bragg pulses (k is the wavenumber of the Bragg beam), $g = 9.781$ m/s^2 is the gravitational acceleration. The details about the chirping during the experiment sequence will be described in Section 5.2.2.

4.4.2 Bragg pulses for velocity selection and interferometry

The atom interferometer is operated by interrogating the Bragg diffraction between atoms and a moving lattices at a magic-wavelength of 813.427 nm. As discussed in Chapter 2, this external state manipulation is sensitive to the initial velocity of the sample. To ensure an efficient implementation of the interferometer, it is essential to prepare the atomic sample with a low temperature. The atoms are cooled and captured in the red MOT with a temperature of approximately 700 nK, which corresponds to an 1-σ momentum width of

$$\Delta p = \sqrt{m_{Sr} k_B T} = 1.51\hbar k \tag{4.61}$$

Consequently, a velocity selection stage becomes necessary, and we implement the selection stage by applying three Bragg π-pulses centered at the resonance frequency considering zero temperature. This

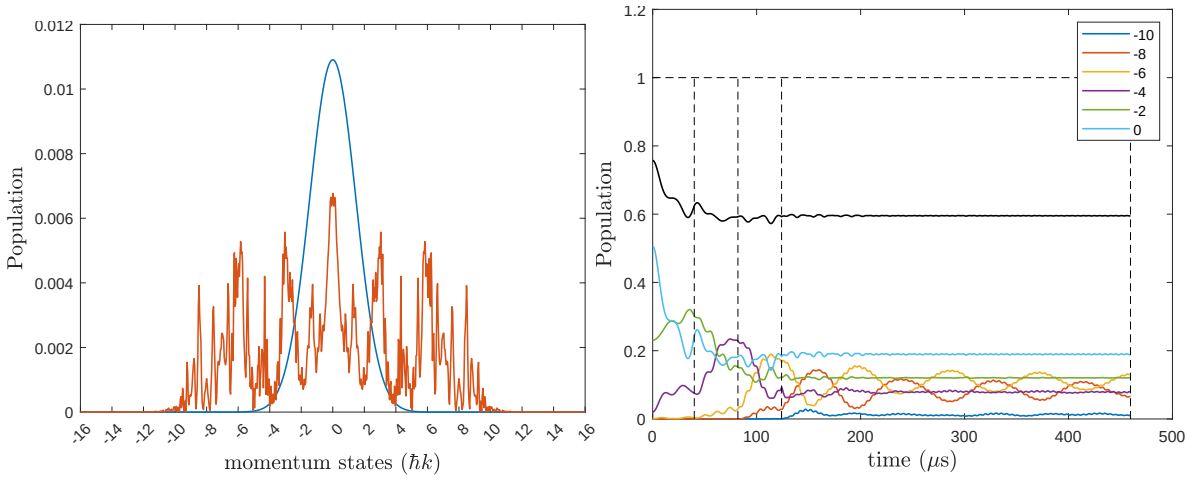

Figure 4.19: Numerical simulation of the imperfection of velocity selection. (a) Momentum distribution with the initial temperature of 700 nK (blue curve) and the momentum distribution after 3 π-pulses of velocity selection (orange curve). (b) The population evolution of each momentum state with 3 π-pulses velocity selection and Rabi oscillation between $6\hbar k$ and $8\hbar k$. The first three vertical dashed line denote the end of velocity selection pulses, while the region between the third and forth vertical dashed lines is the Rabi oscillation of the Bragg diffraction between 6- and 8-$\hbar k$. The black curve is the population sum over the momentum states in negative side. The Rabi frequency is Ω=3.5ω_r, and the normalization is done with eleven state (from -10 to 10 $\hbar k$)

selects the atoms with low temperature and bring them to $6\hbar k$. The configuration for velocity selection and interferometry pulses are illustrated in Figure 4.18.

The selected atoms along the vertical direction have a temperature of approximately 180 nK, demonstrating a significant reduction compared to the atoms in the lattice, which gives the momentum width of

$$\Delta p = 0.76\hbar k \tag{4.62}$$

After the selection stage, about 10% of atoms are selected for further processing. Subsequently, interferometer pulses are applied to transition the momentum state of the atoms between $6\hbar k$ and $8\hbar k$ for the quantum sensing stage.

However, it's essential to acknowledge that the velocity selection stage is not perfect due to the initial velocities of the atoms in the red MOT. Figure 4.19 provides a simulation of the momentum distribution and Rabi oscillation, taking into account the influence of Doppler effects. The simulation was conducted with an atomic temperature of 700 nK and a Rabi frequency of $\Omega = 3.5\omega_r$.

Figure 4.19 illustrates the momentum distribution before (blue) and after (orange) the velocity selection stage considering the effect of a finite temperature of 700 nK. From Figure 4.19(a), it is evident that the momentum distribution following velocity selection is broad in $6\hbar k$, potentially leading to reduced efficiency in Bragg pulses due to the off-resonance effect. Additionally, the population prepared in $6\hbar k$ is relatively low, which results in a decreased signal-to-noise ratio during detection.

The dynamics of population evolution for the momentum states from 0- to -10-$\hbar k$ throughout the velocity selection and Rabi oscillation is presented in Figure 4.19(b). Due to the complexity of the momentum distribution shown in Figure 4.19(a), the population evolution of the state $a\hbar k$ is obtained by the sum over the dynamics of the momentum states from $(a-1)\hbar k$ to $(a+1)\hbar k$. The black curve represents the populations of states on the zero and negative side. During the velocity selection stage, three Bragg pulses are applied, marked by distinct segments in Figure 4.19(b). These pulses consist of a dual Bragg diffraction initially, succeeded by two single Bragg diffraction pulses. Subsequent to the final selection pulse, the system enters the Rabi oscillation stage, where the populations at 6-$\hbar k$ and 8-$\hbar k$ are manipulated. Figure 4.19(b) exhibits an imperfect shift during the Rabi oscillations, attributed to the momentum distribution after the velocity selection.

To align the numerical simulation results with the experimental data, a rescaling of the amplitude was carried out. The normalization is done between only 6-, 8- and 10-$\hbar k$, and the results are presented in Figure 4.20. Following the velocity selection stage, we observe an offset in 8-$\hbar k$ due to the off-resonance effect of the Bragg pulses. Additionally, there is a fraction of 4- and 10-$\hbar k$ oscillation during the Bragg pulses, resulting from the finite temperature of the atomic sample. To evaluate the agreement between between theory and experiment, the experimental data is fitted with the function $P = a \cdot \cos\Omega t \exp(-\tau/t) + \text{offset}$, where a Rabi frequency $\Omega/(2\pi) = 17.6 \pm 0.2$ kHz is obtained. Compared to the Rabi frequency 18.0 kHz we used in the theoretical calculation, this discrepancy is likely attributed to power reductions occurring as the laser beams passing through the optical elements and the viewport.

4.5 Conclusion

In conclusion, this chapter is aiming to comprehensively address several crucial preparation stages for quantum sensing.

Our setup involved constructing an optical lattice to confine atoms, with one of the horizontal lattices aligning with the clock laser. The vertical lattice, formed by merging two cross-polarized beams, serves as a source for both the lattice and Bragg diffraction. Additionally, we elaborate on the setup and performance of phase difference lock between the beams.

Following the loading of atoms into the optical lattice, the clock transition is implemented. Due to the zero-nuclear spin in ^{88}Sr, the clock transition is forbidden. To enable this transition, the magnetic induced spectroscopy is implemented. A detailed study of the clock transition's Rabi oscillation is undertaken by varying the interrogation time while maintaining constant laser power and magnetic fields. Furthermore, a comprehensive theoretical model is developed to investigate damping effects resulting from inhomogeneity broadening due to the clock laser beam profile.

Since Bragg diffraction is sensitive to the initial velocity of the atomic sample, it is important to start with a low temperature. We apply three Bragg pulses, thereby facilitating velocity selection. After the velocity selection phase, the atoms with low temperature are prepared in 6$\hbar$k. Then we observe

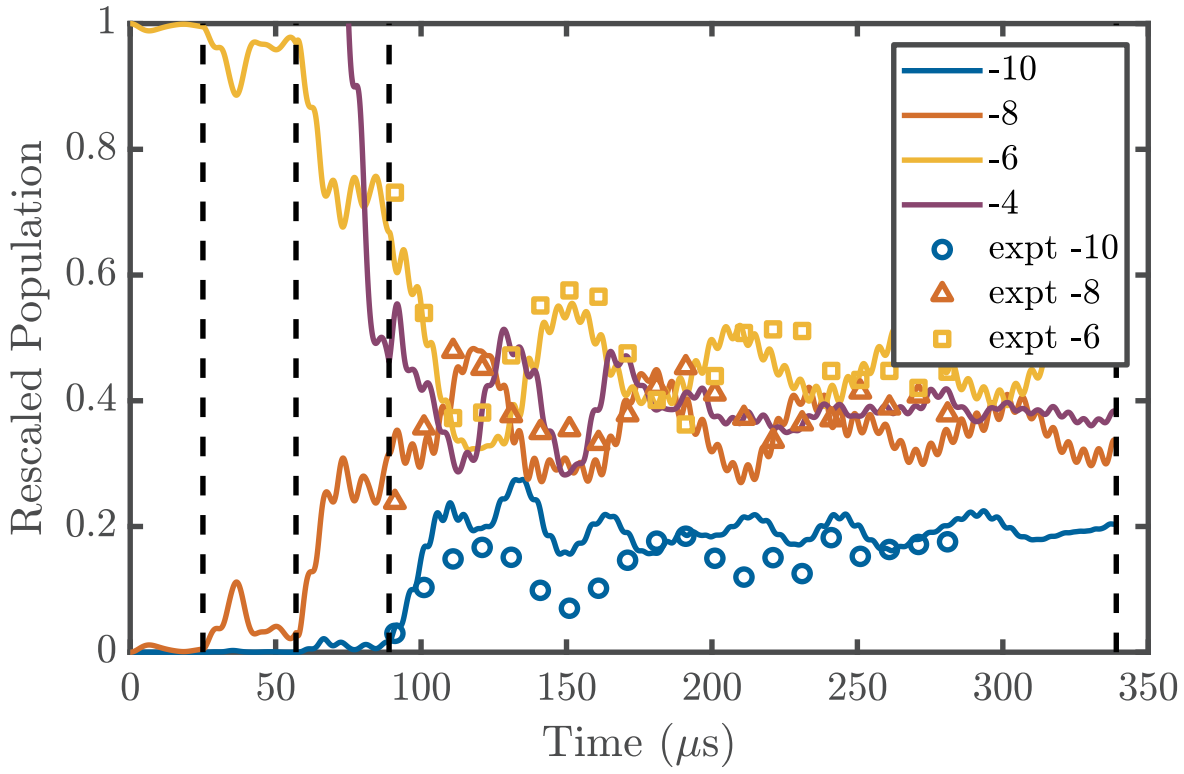

Figure 4.20: Comparison of the Rabi oscillation between the theoretical simulation and experimental data after rescale of the amplitudes, where the normalization is taken with 6-, 8- and 10-$\hbar k$. Similar as Figure 4.19(b), the first three regions separated by the vertical lines are the velocity selection pulses, which are followed by the Rabi oscillation part. The Rabi frequency is $5\omega_r$.

the Rabi oscillation and calibrate the Bragg diffraction. During the atom interferometer phase, the employment of Bragg diffraction allows us to manipulate the momentum states 6- and 8-$\hbar k$.

The subsequent chapter will delve into quantum sensing experiments, encompassing a dual interferometer with atoms in both ground and excited states of the clock transition. Additionally, the measurement of state-dependent force will be explored using the dual interferometer setup.

Chapter 5

Experimental results

5.1 Introduction

In this chapter, the experiment for differential inertial sensing with the prepared atomic sample is discussed. I begin by describing the experimental scheme, covering the sequence, frequency setting of the Bragg pulses, and the subsequent data analysis. The dual atom interferometer is realized by performing the atom interferometer with an atomic sample in the statistical mixture of ground $^1S_0$ and excited $^3P_0$ clock states, with which the universality of free-fall can tested. Furthermore, this scheme allows us to probe state-dependent forces, as elaborated in section 5.4. To introduce state-dependent forces, a light field gradient generated by a 671 nm beam is applied on the interferometer trajectory. This gradient induces state-sensitive acceleration through a differential light shift gradient. Consequently, the state-dependent force experienced can be quantified by analyzing the phase difference between the ground and excited clock states observed in the dual atom interferometer.

5.2 Experimental scheme

5.2.1 Overview of experimental sequence for dual atom interferometer

The experimental sequence for the demonstration of dual atom interferometer is depicted in Figure 5.1. Following the two-stage MOTs described in Section 3.4, a 1D horizontal optical lattice with a beam waist of 80 μm is turned on to trap a fraction of atoms ($\sim 10^5$) from the red MOT. Notably, this horizontal lattice is overlapped with the clock laser beam. Subsequently, the clock transition is implemented to prepare the atomic sample in a mixture of ground and excited clock states. The interrogation time for the clock transition is set to 30 ms, with which the system is put into a statistical mixture.

Since the efficiency of the Bragg diffraction pulses is sensitive to the temperature of the atomic sample, an initial velocity selection stage is conducted using three Bragg pulses. After this selection, the temperature of the atomic sample is approximately 180 nK. Then the Mach-Zehnder interferometer

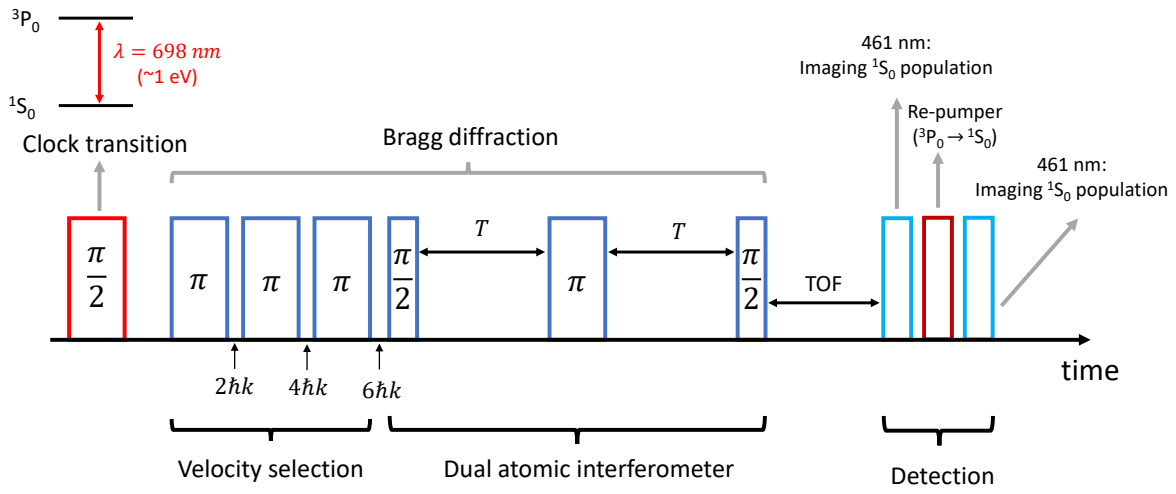

Figure 5.1: Experimental sequence for dual atom interferometer. After loading into the optical lattice, the clock transition is implemented to prepare the atoms in a mixture of ground $^1S_0$ and excited $^3P_0$ states. This is followed by three Bragg pulses for the velocity selection. Then the Mach-Zehnder interferometer is conducted with the prepared atomic sample. A time-of-flight period and state-dependent fluorescence are performed to detect the momentum state population of $^1S_0$ and $^3P_0$. The momentum population of both clock states are measured using the broad $^1S_0 \rightarrow {}^3P_0$ transition at 461 nm.

based on Bragg diffraction is performed by manipulating the momentum states between $6\hbar k$ and $8\hbar k$ with a Rabi frequency of around 13 kHz.

In interferometry based on Bragg diffraction, the momentum states of the atomic sample are manipulated while the internal state remains the same. Therefore, to detect the population of distinct momentum state after the interferometry stage, the atoimic sample is let to further expand by 17 ms to spatially separate the two different momentum states. The atoms in ground state $^1S_0$ are firstly imaged with a resonant 461 nm probe beam ($I = 30I_0$) for 35 μs, which removes the atoms in ground state. Subsequently, repump beams are applied for 2 ms to transfer the excited state atoms from $^3P_0$ to $^1S_0$, followed by a second imaging pulse to detect the momentum state distribution in $^3P_0$.

5.2.2 Frequency-chirp of the Bragg pulses

During the Mach-Zehnder interferometry stage, the atomic cloud undergoes free fall along vertical axis with a velocity change $v_z(t) = v_0 + gt$. This movement necessitates frequency shifting of the Bragg pulses to account for the changing velocities during free fall. As described in section 4.4, to compensate this frequency shift, we chirp the frequency difference between beams composing the Bragg pulses to keep the resonance condition for the two-photon transition, namely $\vec{k}_{\text{eff}} \cdot \vec{v} = 2k(gt + v_0)$.

The interference fringes phase of a Mach-Zehnder interferometer is expressed by the formula [12]

$$\Delta\Phi = (k_{\text{eff}} g - \alpha)T^2 + (\phi_{\text{I}} - 2\phi_{\text{II}} + \phi_{\text{III}}), \tag{5.1}$$

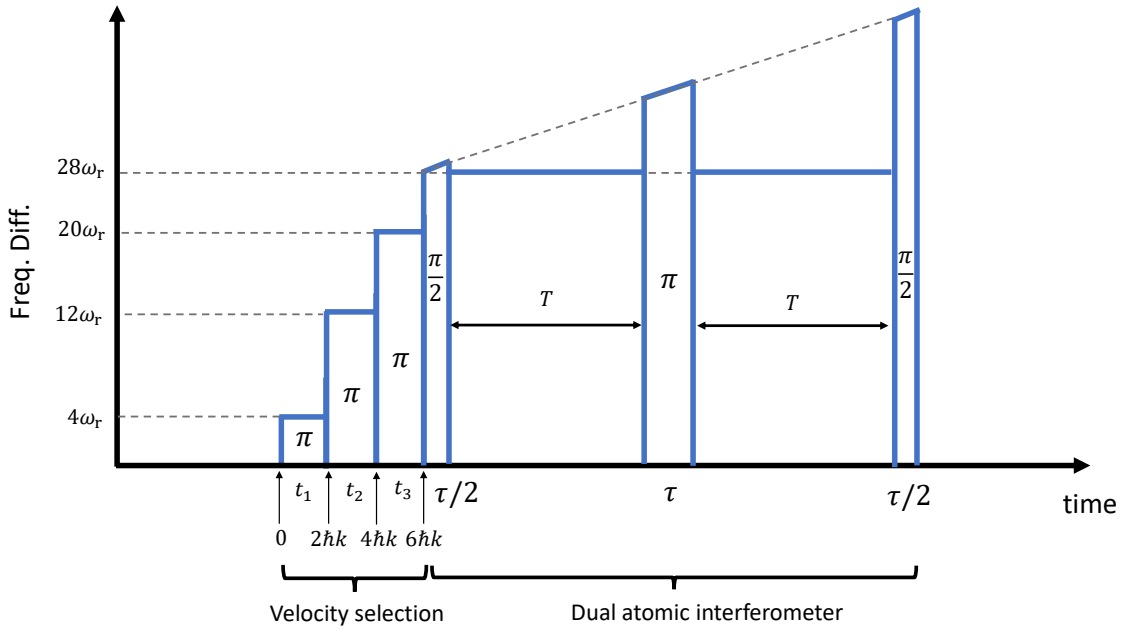

Figure 5.2: Bragg pulse frequency setting in the experiment. The frequency difference between the two beams that composing the Bragg pulses is fixed at the resonance during the velocity selection pulses. For the pulses of Mach-Zehnder interferometer, the Bragg diffraction frequency is chirped to compensate the velocity change during the interrogation between atom and light field, while during the free-evolution time, the Bragg beam frequency is tuned back to the resonance for the transition $6\hbar k$ to $8\hbar k$ without considering the velocity change to accumulate interference phase.

where $\Delta\Phi$ is the interferometer phase; $k_{\text{eff}} = 2k$ is the effective wave-number of the optical field; g is the gravity; T is the free-evolution time between the pulses; α is the chirp rate during the interferometry; ϕ_{I}, ϕ_{II} and ϕ_{III} are the phase difference between the two lasers composing the Bragg pulse for the $\pi/2$-, π- and $\pi/2$-pulses respectively.

The frequency change of the Bragg pulses during the experimental sequence is illustrated in Figure 5.2, and the specific frequency setting of the Bragg pulses for the velocity selection and atom interferometer are detailed in Table 5.1. The Rabi frequency of Bragg diffraction is 13 kHz, corresponding to a π-pulse duration of 40 μs. The frequencies of the first three π-pulses during the velocity selection stage are set to be $4\omega_r$, $12\omega_r$, and $20\omega_r$ without chirping. However, for the atom interferometer pulse, a chirp rate of 24 Hz/μs is implemented to compensate for the Doppler effect during both the laser interrogation and the free-evolution time. Moreover, in the dark time, the frequency of the Bragg beam is tuned back to a fix frequency difference of $28\omega_r$ for the phase accumulation. Notably, the same DDS is utilized during both the velocity selection and interferometer stages, ensuring the preservation of phase continuity when switching between different configurations. Therefore, considering that the two-photon resonance condition is fulfilled at each Bragg sequence, and $\Phi_I - 2\Phi_{II} + \Phi_{III} = 0$, the

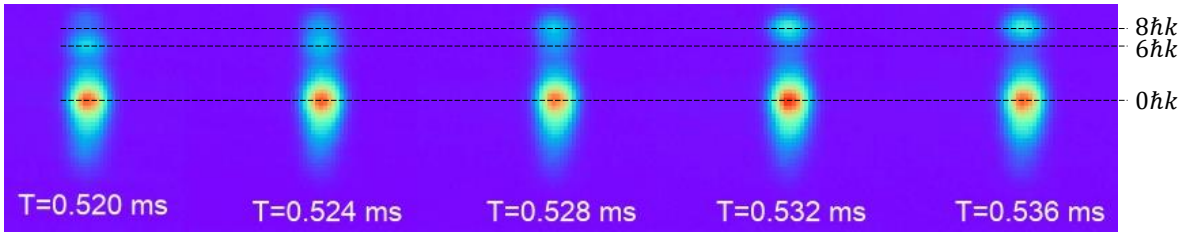

Figure 5.3: Fluorescence image of the $^1S_0$ level for the output of the Mach-Zehnder atom interferometer with the dark time scanning. The dashed lines denote the momentum states of $0\hbar k$, $6\hbar k$ and $8\hbar k$.

interferometry phase is given by

$$\Delta\Phi = kgT^2. \tag{5.2}$$

Time	Transition	Stage	Freq. Diff. $\Delta\omega$ (start)	Freq. Diff. $\Delta\omega$ (end)	Chirp α
0 to 40 μs	$0 \rightarrow 2\hbar k$	VS	13.68 kHz	13.68 kHz	-
42 to 82 μs	$2\hbar k \rightarrow 4\hbar k$	VS	41.04 kHz	41.04 kHz	-
84 to 124 μs	$4\hbar k \rightarrow 6\hbar k$	VS	68.40 kHz	68.40 kHz	-
126 to 146 μs	$6\hbar k \leftrightarrow 8\hbar k$	AI	95.76 kHz	95.28 kHz	24 Hz/μs
148 to (148+T) μs	-	AI	95.76 kHz	95.76 kHz	-
(150+T) to (190+T) μs	$6\hbar k \leftrightarrow 8\hbar k$	AI	(95.28-0.024×T) kHz	(94.32-0.024×T) kHz	24 Hz/μs
(192+T) to (192+2T) μs	-	AI	95.76 kHz	95.76 kHz	-
(194+2T) to (214+2T) μs	$6\hbar k \leftrightarrow 8\hbar k$	AI	(94.32-0.024×2T) kHz	(93.84-0.024×2T) kHz	24 Hz/μs

Table 5.1: Frequency setting during the experiment. VS: velocity selection; AI: atom interferometer. T is the dark time in the unit of μs.

In Table 5.1, the precision of the Bragg frequency setting is set up to the second digit, which may introduce imperfections in the phase accumulation. To account for this, an extra phase $2k_{\text{eff}}g\mathrm{d}tT$ is incorporated into the analysis, as described in Section 5.3. Additionally, there is also a 2 μs time gap between the switches of the pulses, caused by the delay of lab control system. When switching off the pulses, the Bragg beams are off during this 2 μs, while the frequency of the beam stays same as the frequency of the pulse. This delay can be account into the parameter dt. When the pulses are switched on, the frequency is kept same as the dark time during this 2 μs delay, which gives some frequency mismatch on the Bragg pulses. Fortunately, for the dual AI experiment, the differential phase is the key result so this common mode influence can be neglected.

5.2.3 Data analysis

The images captured during the detection with varying dark times are depicted in Figure 5.3. Each image is an average of five shots. The dashed lines denote the position of $0\hbar k$, $6\hbar k$ and $8\hbar k$ momentum states after time-of-flight period, where the profile at 0 $\hbar k$ corresponds to the atoms that are not

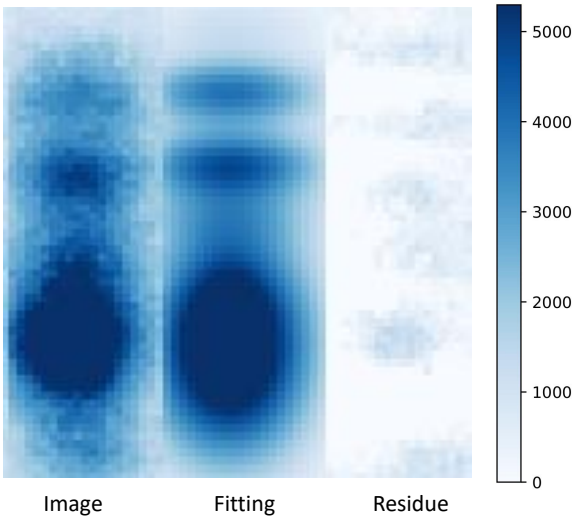

Figure 5.4: An example for the image fitting at the output of the interferometrywhile the middle image depicts the fitting outcome achieved by combining eleven 2D Gaussian functions. The residue shown on the left highlights the differences between the experimental data and the fitted model. Specifically, the three most prominent peaks correspond to the 0, 6 and 8 $\hbar k$ momentum states.

selected by the first three pulses.

In the subsequent data analysis, we employ a sum of eleven 2D Gaussian functions to determine the population from $-10\hbar k$ to $10\hbar k$:

$$f(x,z) = \sum_i A_i \exp\left[-\left(\frac{(x-x_{i0})^2}{2\sigma_{ix}^2} + \frac{(z-z_{i0})^2}{2\sigma_{iz}^2}\right)\right], \tag{5.3}$$

where $i = -10, -8, ..., 10$ denotes the i-th momentum states. We set the x_{i0} and y_{i0} as fixed values, obtained from $x_{i0} = x_{00} + i \times \hbar k/m \times T_{\text{tot}}$. Here, T_{tot} represents the overall duration encompassing velocity selection, interferometry, and the time-of-flight period. The parameters A_i, σ_{ix} and σ_{iy} are determined through fitting process. Subsequently, the population of each state is calculated as follows:

$$P_i = A_i \cdot \sigma_{ix} \cdot \sigma_{iz}, \tag{5.4}$$

Figure 5.4 illustrates one example of the image fitting results with the sum of eleven 2D Gaussian functions. The parameters such as σ_{ix} and σ_{iz} can be obtained, where we assume that σ_{ix} is independent of the index i ($\sigma_{ix} \sim \sigma_{0x}$), while $\sigma_{iz} \neq \sigma_{0z}$ if $i \neq 0$. This fitting results as well as the low residue indicate the fitting procedure is capturing most of the experimental profile.

5.3 Dual atom interferometer

With the experimental scheme established in Section 5.2, we are able to execute dual atom interferometer with the atomic sample in a mixture of ground and excited clock states. This enables the demonstration of differential inertial sensing, with the two states separated in the optical domain.

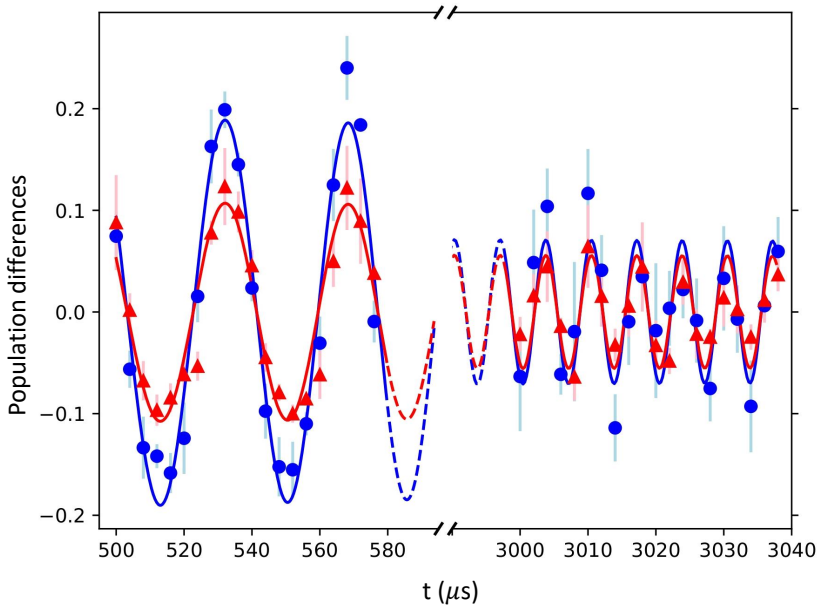

Figure 5.5: Interferometry fringes for ground ($^1S_0$) and excited ($^3P_0$) state with the dark time scanning around 0.5 ms and 3 ms. The blue dot and curve illustrate the experimental data and fitting of the $^1S_0$ interferometry fringes respectively, while the red denotes the results of $^3P_0$ state. The population differences are calculated from $(P_8 - P_6)/2$. The error bars are obtained from the standard deviation of 4 sets of data.

5.3.1 Experimental results

The experimental fringes for the two states ($^1S_0$ and $^3P_0$) in the dual atom interferometer are depicted in Figure 5.5, denoted in blue and red respectively. The population differences are calculated from $(P_8 - P_6)/2$, and the normalization is done with P_6 and P_8. Each data point depicted in Figure 5.5 is the averaged result of four values obtained from the image analysis discussed in section 5.2.3. The images are averaged with 5 shots and the error bars calculated from the standard deviation across these four sets of data. Consequently, each data point presented in the fringe plot entails a total of 20 experiment shots.

The fringes from the ground state are firstly fitted using the function:

$$f(T) = a_g \cdot \cos\left(k_{\text{eff}} \cdot g \cdot (T + \mathrm{d}t_g)^2 + \phi_g\right) \cdot \exp(-T/\tau_g), \tag{5.5}$$

where a_g, g, τ_g, ϕ_g and $\mathrm{d}t_g$ are obtained from the fitting. We remind that the parameter $\mathrm{d}t_g$ is introduced to account for the imperfections due to the chirping during the interferometry stage. The exponential term describes the decay of the fringes, and ϕ_g is the phase offset of the fringes.

Using these fitting parameters obtained from the ground state fringes, we perform a fit on the data points of the excited state with the equation:

$$f(t) = a_e \cdot \cos\left(2k_{\text{eff}} \cdot (g + dg)(T + \mathrm{d}t_g)^2 + \phi_g\right) \cdot \exp(-T/\tau_e), \tag{5.6}$$

The parameters g, ϕ_g and $\mathrm{d}t_g$ in Eq. 5.6 are constants and determined through the fitting of the

ground state data. The parameter dg is obtained from the fitting, interpreted as the result of test for universality of free-fall, a_e and τ_e are the amplitude and decay of the fringes in excited state. With the fitting, we find the value of $\mathrm{d}g/g = (1.8 \pm 3.1) \times 10^{-4}$.

Several other atom interferometer platforms have been performed for testing the weak equivalence principle. One such example involves a Bragg atom interferometer conducted in a gradiometer configuration with rubidium atoms to compare the free-fall in hyperfine states and in coherent superposition states [29]. An Eötvös ratio with a relative uncertainty at 10^{-9} is achieved by operating the differential atom interferometer with a dark time of 80 ms. Other experiments have explored comparisons of free fall behavior between different atom species and atoms in diverse spin orientations [23][25][26][107]. The uncertainty of the tests based on atom interferometer can be achieved at the level of 10^{-12}, obtained by comparison of the gravitational acceleration between two isotopes of rubidium [23]. compared to these platforms, the limitation of our experimental system is mainly from the finite temperature of the gas, which will be discussed in section 5.5. Notably, precise measurements has been conducted with other platforms such as torsion balances in a laboratory setting [19][20], Lunar ranging[21] or Earth's orbit[22], leading to verification of weak equivalence principle at 10^{-13}, 10^{-13}, and 10^{-15} level, respectively.

5.3.2 Non-magic effect

In our dual atom interferometer scheme, we utilize the magic-wavelength of the clock transition to obtain the same polarizability for the ground and excited clock states. This gives an identical Rabi frequency as well as the light shift during the experiment. To further investigate, we conduct the interferometry process with the Bragg beams operating at non-magic wavelengths, as depicted in Figure 5.6. Figure 5.6 (a) and (b) showcase the fringes obtained with the Bragg beams operating at 369.40468 THz and 367.68629 THz respectively, approximately ± 1 THz away from the magic-wavelength (368.55468 THz).

Through an identical analysis approach as applied in the dual atom interferometer setup, the sensitivity obtained in non-magic cases is of the same order as in magic case. We do not observe any extra phase shift between states $^1\mathrm{S}_0$ and $^3\mathrm{P}_0$ due to the non-magic beams within the sensitivity range of our system. Figure 5.6 presents the comparison of the fringes at three wavelengths, the phase shift between different wavelengths is matched with the wave-number difference of the three cases. This can be theoretically quantified as $\Delta\phi = 2\Delta k g T^2$, where Δk represents the wave-number difference between the Bragg beam wavelengths. The theoretical values of the phase shifts are calculated as $\Delta\phi_{\mathrm{th1}} = -3.1$ rad and $\Delta\phi_{\mathrm{th2}} = 3.2$ rad, corresponding to the phase differences between the magic and non-magic 1 and 2 cases. The experimental results give $\Delta\phi_{\mathrm{exp1}} = (-3.04 \pm 0.11)$ rad and $\Delta\phi_{\mathrm{exp2}} = (3.25 \pm 0.13)$ rad, showing an agreement with the theoretical values.

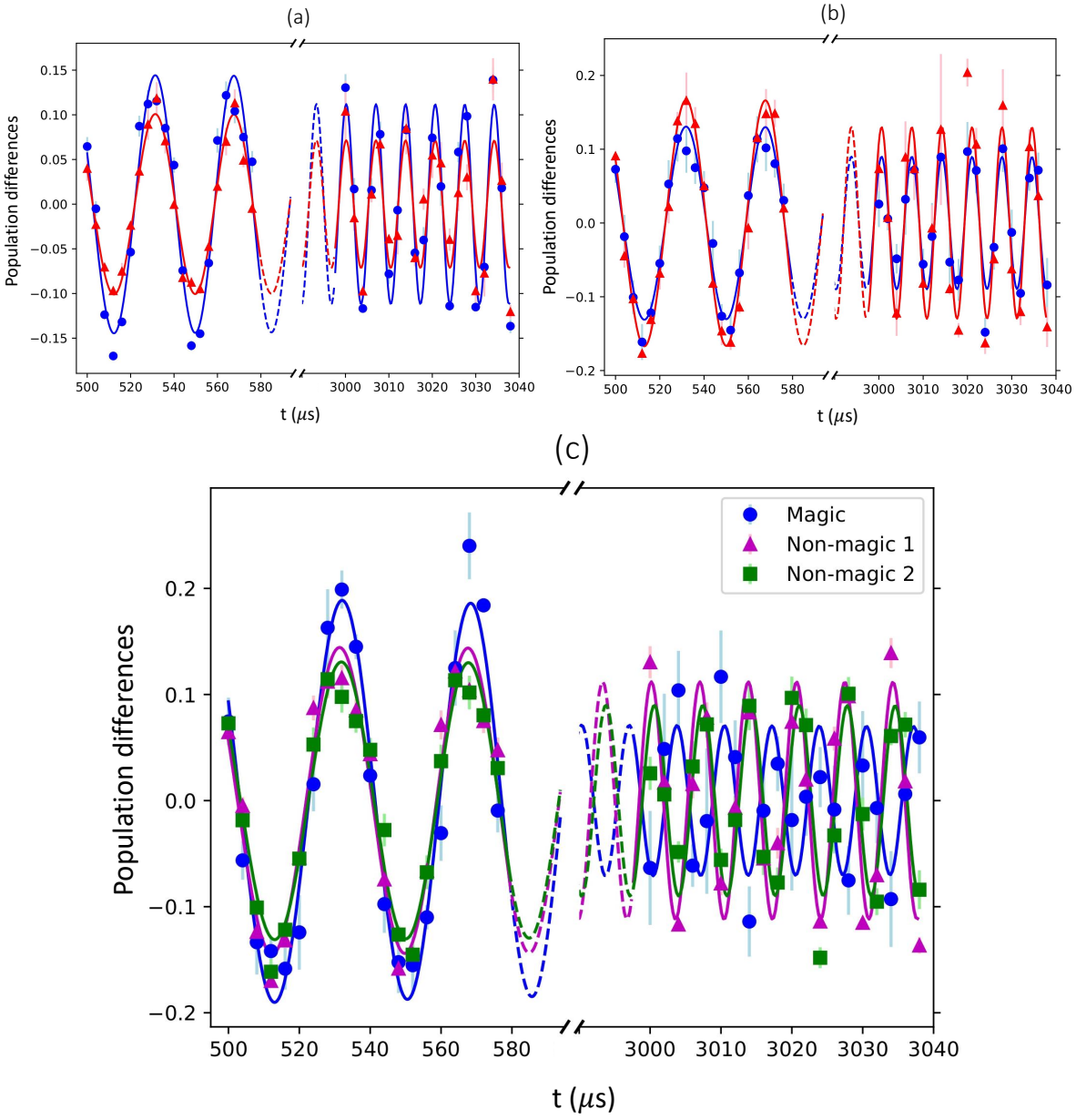

Figure 5.6: Dual AI fringes with the Bragg beam operating at non-magic wavelength: (a) $f_{\text{non-magic1}}$=369.40468 THz; (b) $f_{\text{non-magic2}}$=367.68629 THz. (c) The comparison of the fringes between the magic and non-magic cases. The magic-wavelength is f_{magic}=368.55468 THz.

5.4 Measurement of state-dependent force

Our dual atom interferometer configuration facilitates the probing of state-dependent forces through the differential phase. In this context, we introduce an external optical field gradient on the Mach-Zehnder interferometer path, leading to state-sensitive acceleration. Consequently, this approach allows us to quantify the state-dependent forces by analyzing the phase difference between the ground and excited states detected in the dual atom interferometer.

5.4.1 Theoretical model

In this section, I delve into the theoretical model concerning the measurement of state-dependent forces.

5.4.1.1 Differential acceleration provided by light shift

We first consider a laser beam applied on the atomic sample in a mixture state of $^1\mathrm{S}_0$ and $^3\mathrm{P}_0$. The real part of the polarizability difference can be expressed as

$$\delta\alpha = \mathrm{Re}(\alpha_e - \alpha_g), \tag{5.7}$$

where α_g and α_e are the polarizability of ground ($^1\mathrm{S}_0$) and excited ($^3\mathrm{P}_0$) states. The differential light shift along z-axis provided by the light is given by

$$U(z) = -\frac{1}{2\epsilon_0 c}\delta\alpha I(z), \tag{5.8}$$

where $I(z) = I_0 \exp(-2z^2/\omega^2)$ is the intensity of the laser beam, and $I_0 = 2P/(\pi\omega^2)$ is the peak intensity. The internal state-sensitive acceleration is then induced by this differential light shift:

$$a(z) = -\nabla U(z)/m, \tag{5.9}$$

where m is the mass of the atom. Therefore, this difference of the acceleration between ground and excited state can be encoded into the interferometry phase and measured via the differential phase between the two states.

For the experimental demonstration, we apply a Gaussian beam operating at 671 nm. With the significant energy separation between the two clock states, the differential polarizability $\Delta\alpha$ can be notably large, detectable forces within the sensitivity range of our apparatus. Specifically, for strontium atoms at 671 nm, as depicted in Figure 5.7, we observ $\Delta\alpha \simeq 1672$ a.u., with $\alpha_{^1\mathrm{S}_0} \simeq -353$ a.u. and $\alpha_{^3\mathrm{P}_0} \simeq 1319$ a.u..

Given the polarizability and the profile of the 671 nm beam, we can numerically calculate the potential difference and the resulting differential acceleration. The blue curve in Figure 5.8 illustrates the potential difference generated by the beam along z-axis, which is proportional to the intensity of the beam. The orange curve in Figure 5.8 represents the differential acceleration, proportional to the gradient of potential difference as indicated in Eq 5.9. Notably, this analysis reveals that the differential

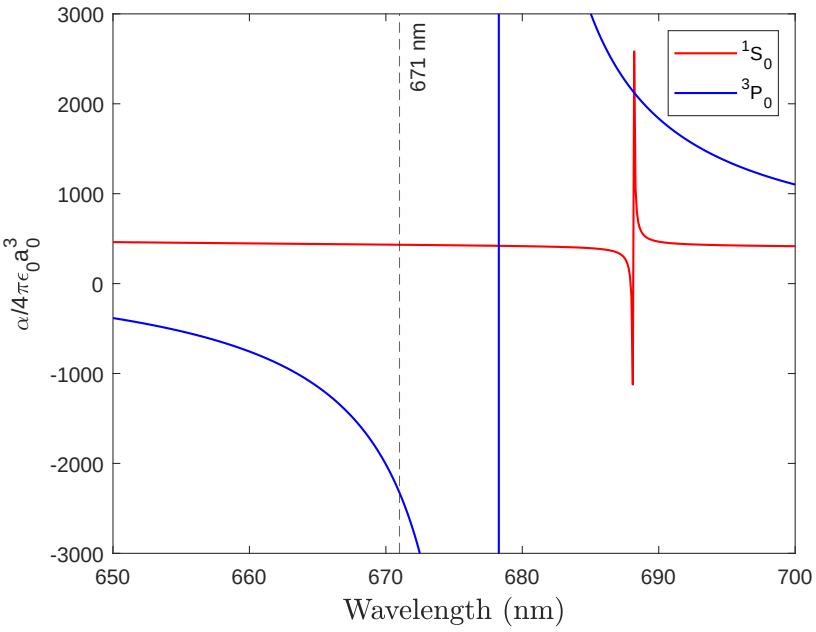

Figure 5.7: The calculated polarizability for the state $^1S_0$ and $^3P_0$ from 650 nm to 700 nm. The polarizabilities at 671 nm are highlighted by the dashed line, which is the wavelength of the external field we applied on the atomic sample to provide the state-dependent acceleration.The parameters in this calculation are obtained from [1].

acceleration is zero when atoms are located at the center of the beam. The maximal acceleration is obtained at $z = \sigma$=$\omega_{671}/2$=350 μm, where ω_{671} denotes the waist of the 671 nm laser beam.

5.4.1.2 Phase difference induced by differential acceleration

Consider the $\pi/2$-T-π-T-$\pi/2$ Mach-Zehnder atom interferometer, where k is the magnitude of the wave vector. T is the dark time. I also remind that the interferometer is performed only along z-axis.

The maximum separation during the atom interferometer is given by $\delta z = \hbar k_{eff} T/m$, where $k_{eff} = 2nk$ is the effective wavevector and n is the diffraction order. Over the interferometer, the atoms experience a free fall in gravity through a distance that is given by $z_g = 2v_0 - 2gT^2$, where v_0 is the initial velocity of the atoms. Taking the interrogation time as 2 ms, we obtain δz=22 μm and z_g=230 μm, which are smaller than the typical length scale of the transverse beam profile. For simplicity, I take z as the initial position of the atom and $a(z)$ is considered to be constant during the atom interferometer phase. Under these assumptions, the interferometric phase difference between the two internal states is given by

$$\Delta\phi(z) = k_{\text{eff}} a(z) T^2 \tag{5.10}$$

Therefore, the state-dependent acceleration can be encoded into the differential phase between the two internal states.

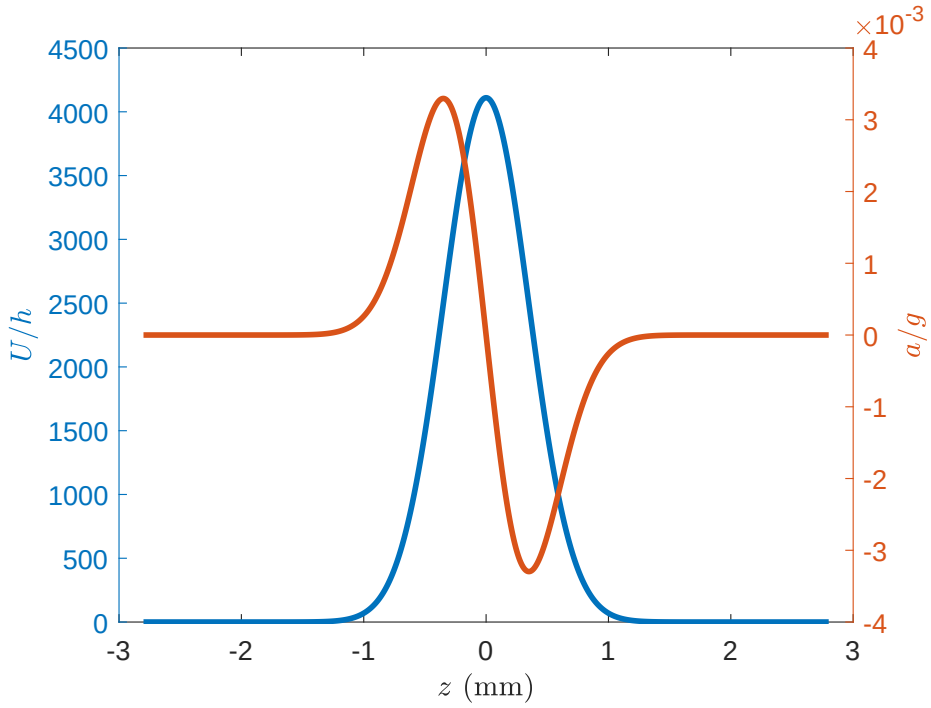

Figure 5.8: Potential difference (blue curve) and differential acceleration (orange curve) along z-axis induced by the 671 nm beam. The calculation is done with the 671 nm laser beam waist of ω_{671}=700μm, and the power is 670 mW.

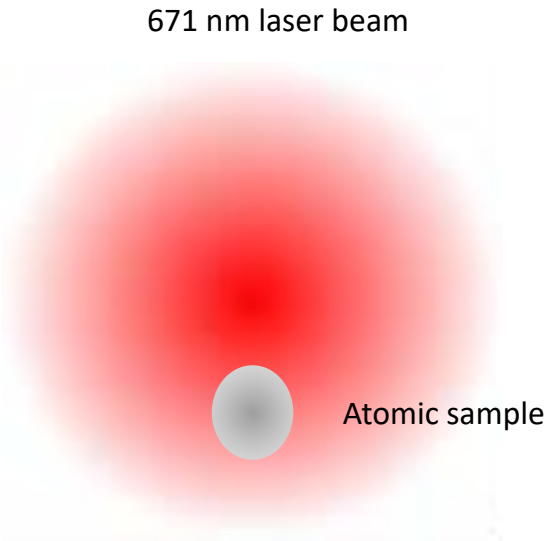

Figure 5.9: Configuration of 671 nm laser with atomic sample.

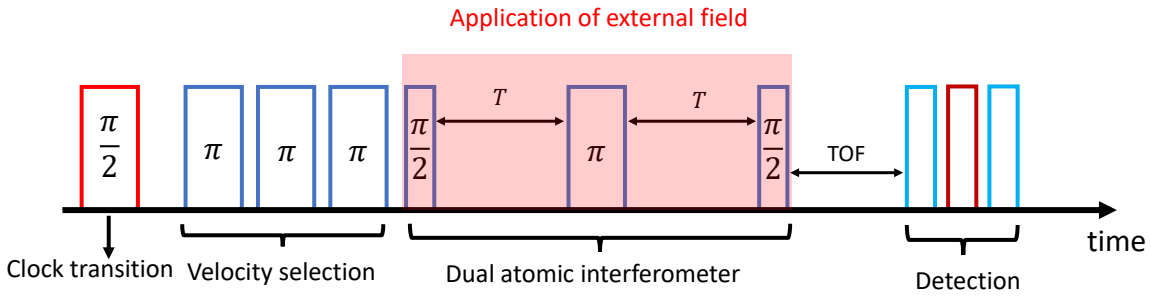

Figure 5.10: Dual atom interferometer sequence with the application of an additional external field. The light field is applied during the Mach-Zehnder interferometer stage to provide the differential potential for the probing of state-dependent force.

5.4.2 Experimental demonstration

5.4.2.1 Experimental scheme

The sequence for probing state-dependent force is illustrated in Figure 5.10. The external optical field is activated during the Mach-Zehnder atom interferometer stage. During the dual atom interferometer, the 671 nm beam provided a differential force, induced by the differential light shift between the ground and excited states. Consequently, the state-dependent force can be detected from the phase difference between the ground and excited clock states. The 671 nm laser beam is aligned on horizontal plane and collimated with a beam waist of 700 μm.

5.4.2.2 Experimental results

To calibrate the performance of the differential inertial sensing, we measure the phase difference with different power of 671 nm beam. The interference fringes corresponding to varied powers (670 mW, 410 mW, 200mW) are illustrated in Figure 5.11, where the differential phases induced by the external field gradient are observed. Each data points are averaged with 5 sets, and each set of data is determined from the fitting results of the image averaged with 10 single shots. The error bars shown in the figure are calculated from the standard deviation across the 5 sets of data.

To obtain the phase difference, both the ground and excited states fringes are fitted by

$$f(t) = a \cdot \cos(k_{\text{eff}} \cdot gt^2 + \phi_i) + \text{offset}. \tag{5.11}$$

In the dual atom interferometer scheme, where the differential phase holds significance, we take $k_{\text{eff}} = 2\pi/\lambda$ ($\lambda = 813.427$ nm is the wavelength of Bragg beams) and $g = 9.781$ as constants in the fitting. Parameters like a, ϕ_i ($i = e, g$) and offset are determined from the fitting. The phase distinction $\Delta\phi = \phi_e - \phi_g$, representing the discrepancy between the phases of the excited and ground clock states, can be computed from the fitting results.

The differential phase values obtained at different dark times are presented in Figure 5.12 and 5.13. In Figure 5.12, the fringes for $^1S_0$ (blue) and $^3P_0$ (purple) are displayed with the fitting function in

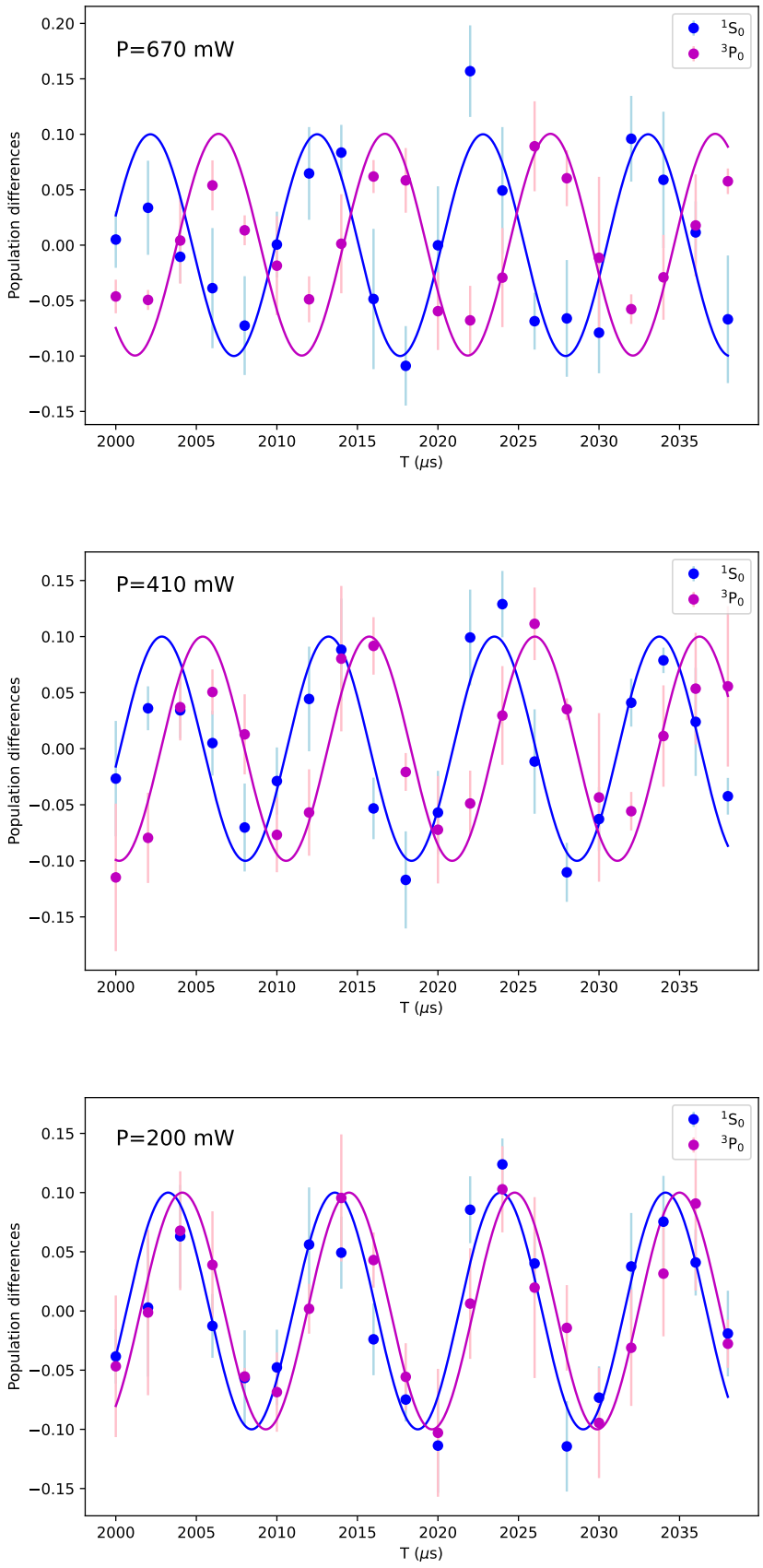

Figure 5.11: Interferometry fringes in ground and excited clock states with different intensity of the external light field. Top: 670 mW; middle: 410 mW; bottom: 200 mW.

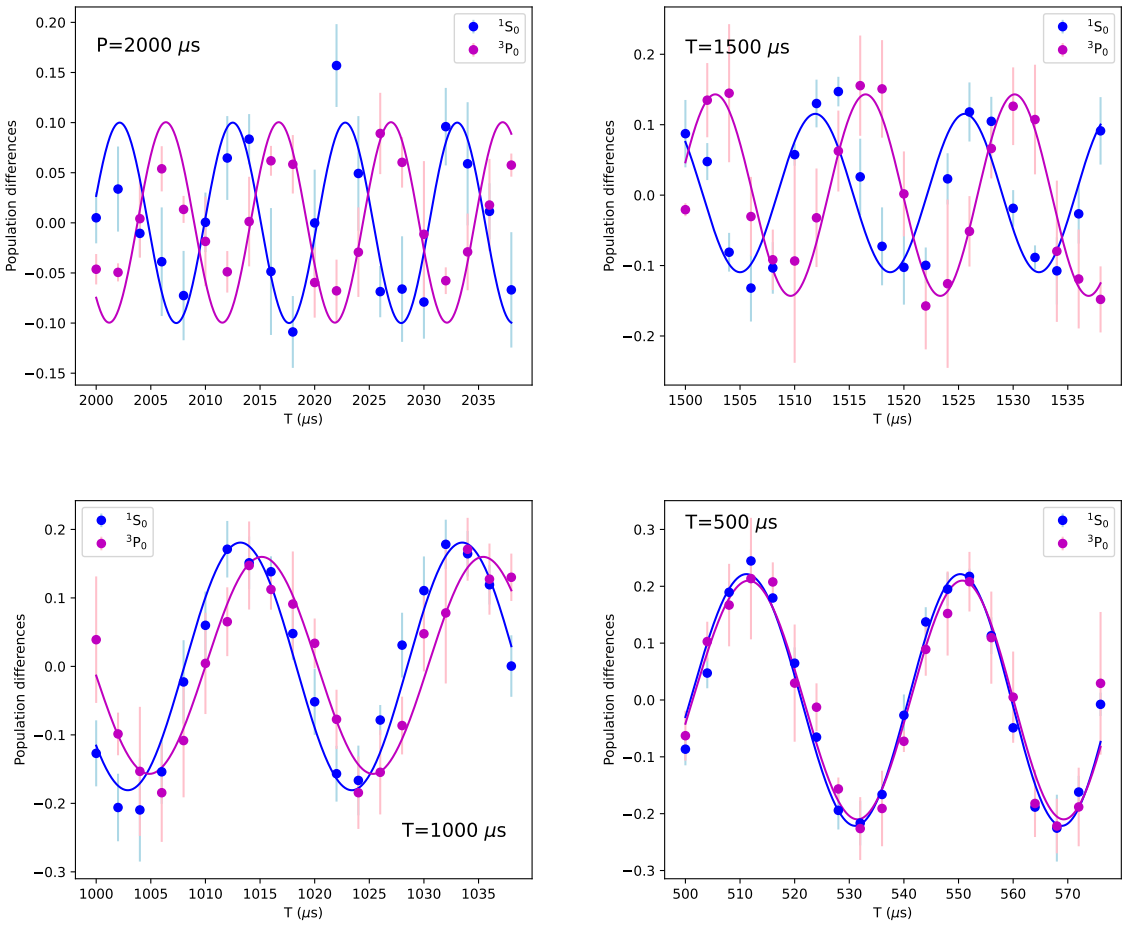

Figure 5.12: Differential phase measured in the dual atom interferometer with various dark time (0.5 ms, 1 ms, 1.5 ms and 2 ms). The blue dots and curve are the population difference of experimental data and fitting results of $^1S_0$, while the purple represents the results for $^3P_0$.

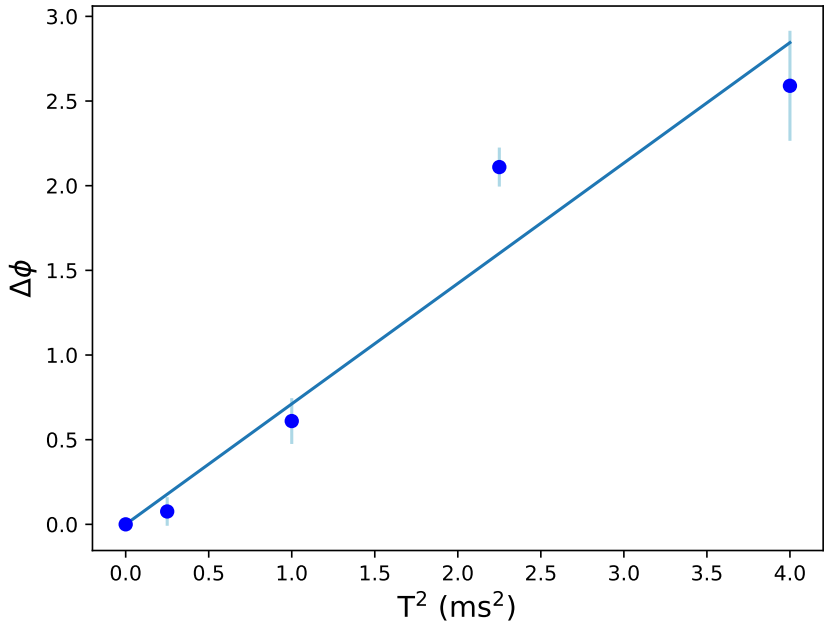

Figure 5.13: Differential phase measured in the dual atom interferometer versus the square of dark time. The solid curve shows the fitting results of the experimental data. The fitting function is $f(T^2) = C \cdot T^2$.

Eq 5.11, where the phase difference $\Delta\phi$ can be extracted. Due to the presence of state-dependent acceleration, the phase difference accumulation is proportional to T^2. Therefore, the data points depicted in Figure 5.13 are fitted using a quadratic function $f(T^2) = C \cdot T^2$. From the fitting we found a slope of C_{exp}=(0.71±0.06)×10^6 rad/s^2, for a 671 nm laser power of 670 mW. Comparatively, the theoretical maximum slope predicted is C_{th}=0.72×10^6 rad/s^2. This theoretical value is calculated from the phase accumulation expression in Eq 5.10, where the state-sensitive acceleration is calculated from the potential difference in Eq 5.9 with given 671 nm beam properties. We found an agreement with between the theoretical and experimental values within the corresponding uncertainties.

5.5 Finite temperature: limitation of the system performance

The Eötvös ratio obtained in our dual atom interferometer system is $(1.8 \pm 3.1) \times 10^{-4}$. Compared to the state-of-art test platforms, this moderate value is mainly limited by the finite temperature of the atomic sample. This leads to imperfection of the Bragg pulses and limits the dark time to a few milliseconds, which indicates that preventing the high atomic temperature in the experiment is necessary. In this section. the limitation and the potential strategies to overcome it are discussed.

There are two main limitations caused by the finite temperature in our system. Firstly, the non-zero initial velocity of the atomic sample results in reduced efficiency of the Bragg pulses due to the

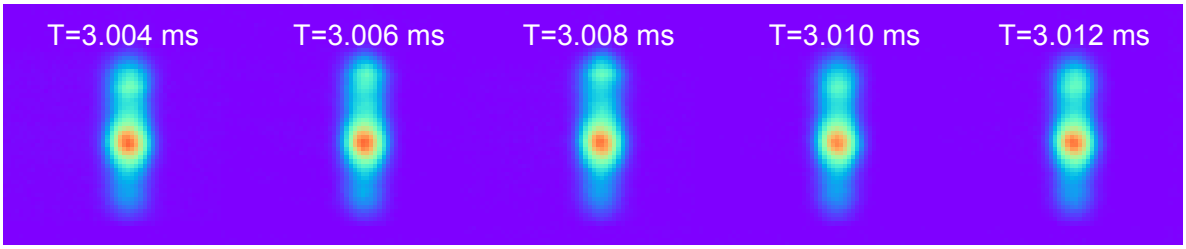

Figure 5.14: Images from the dual atom interferometer output in ground state with the dark time around 3 ms and with time-of-flight period of 17 ms.

Doppler effect. Consequently, this leads to the broadening of the momentum distribution and the presence of multiple velocity classes. The details about this have been discussed in section 4.4.2.

Secondly, the free expansion resulting from the finite temperature during the dark time and time-of-flight period might also hinder the spatial separation of different momentum states, contributing to a decrease in the signal-to-noise ratio. Also, the size of the atomic cloud poses a limitation, making it challenging for different momentum states to be spatially separated during the time-of-flight period. This issue can complicate the analysis of fluorescence images and result in a reduction in the signal-to-noise ratio. Therefore, preventing large temperature is necessary in our experiment.

As depicted in Figure 5.14, I present averaged images under a dark time around 3 ms. Compared to the images with shorter interrogation time (around 500 μs) shown in Figure 5.3, the longer dark times lead to more significant free expansion, resulting in a larger atomic sample at the output port of the interferometer. This expansion poses a challenge in effectively separating different momentum states spatially. Take the interrogation time as 3 ms for an example, the expansion during the dark time can be calculated by

$$\sigma = \sqrt{\frac{k_B T}{m} \cdot t^2 + \sigma_0^2}, \tag{5.12}$$

where T is the temperature of atoms; t is the total free expansion time, including the two interrogations and time-of-flight (17 ms); σ_0 is the initial size of the atomic sample. By inserting the experimental values $t = 3 \times 2 + 17$ ms, $T = 180$ nK, and the atomic size is initially measured to be $\sigma_0 = 150$ μm, the cloud size on the detection can be theoretically determined to be $\sigma = 177$ μm. However, after 17 ms time-of-flight period, the separation between 6- and 8-$\hbar k$ is given by

$$\Delta z = \frac{2\hbar k}{m} \cdot t_{TOF} \approx 190 \ \mu m \tag{5.13}$$

Thus, the oscillation observed in the fluorescence image is vague, which results in a reduction of the signal-to-noise ratio in the data fitting of the detection image.

To address this challenge, one potential strategy is to employ large momentum transfer techniques. This can be achieved by combining Bragg diffraction with Bloch oscillations, as outlined in [34][108]. Here, the Bragg diffraction is utilized to coherently split different momentum states, followed by the application of accelerating lattices during the Bloch oscillation stage to enhance the momentum transfer. Additionally, there is another magic-wavelength presence at approximately 477 nm, which

gives a larger momentum kick during the Bragg pulses. The large momentum separation between the two states makes the spatial separation easier, and this can potentially increase the signal-to-noise ratio when analyse the fluorescence signal.

In addition to large momentum transfer, reducing the atomic sample temperature through cooling processes presents an alternative solution to mitigate the limitations arising from initial atomic velocities. One possible method is to conduct sideband cooling in the optical lattice [68]. With a mean occupation number of $\bar{n} = 0.51$, there is room for improvement with the narrow transition $^1S_0 \leftrightarrow ^3P_0$.

In conclusion, the finite temperature of the atomic sample represents a significant source of error and noise in our experiment. This limitation constrains the dark time of the interferometer and introduces statistical uncertainties at the 10^{-4} level. Additionally, the second-order Zeeman effect can contribute to phase shift errors and noise. Specifically, with a magnetic field bias of B and gradient of δB, differential accelerations $\delta a \propto B \cdot \delta B$ are experienced by the atoms in ground and excited clock states. Fortunately, the magnetic field can be controlled at the mG-level with our compensation system installed, resulting in phase noise below μrad. The uncertainty introduced by the second-order Zeeman shift is below 10^{-9}. Moreover,owing to the dual atom interferometer configuration adopted in our experiment, manipulation of atoms in ground and excited states occurs concurrently and at identical positions. Consequently, the AC Stark effect induced by intensity fluctuations in the Bragg beams is considered a common noise source. This effect, often a significant systematic error in various atom interferometer setups, is mitigated in our experimental setup [29][14].

5.6 Conclusion

In this chapter, I present the experimental results of dual atom interferometer for differential inertial sensing. This approach involves preparing the atomic sample with a mixture of ground and excited clock states, followed by velocity selection and subsequent Mach-Zehnder interferometry. By conducting the interferometer with atoms in both ground and excited states simultaneously, we effectively test the weak equivalence principle. Currently, our setup achieves a sensitivity at the 10^{-4} level, with limitations stemming from the finite temperature and size of the atomic sample. Additionally, this scheme enables detection of state-dependent forces from the phase differences of the fringes. To exhibit this, we introduce a 671 nm beam with a Gaussian profile onto the interferometry path as an external force during quantum sensing.

Addressing the limitations posed by the finite temperature of the atoms is crucial for enhancing the dual atom interferometer's performance. These limitations result in reduced signal-to-noise ratio and restricted dark times. Implementing alternative cooling strategies like sideband cooling in lattice structures can yield lower-temperature atomic samples. Furthermore, utilizing Bragg beams operating at an alternative magic wavelength around 477 nm may offer increased separation between states, potentially enhancing the signal-to-noise ratio during fluorescence image analysis. Additionally, integrating a vibration isolation platform within the system might be a upgrade to minimize noise introduced by

the retro-reflect mirror of the Bragg beams.

Chapter 6

Conclusion and Outlook

In summary, this thesis presents an experimental setup designed to produce an ultra-cold strontium atomic source. Building upon this setup, we introduce and validate a dual atom interferometer concept utilizing the clock transition in ^{88}Sr, offering potential applications in differential inertial sensing.

Our work involves the development of a compact ultra-cold Sr experimental system featuring transverse loading of atoms into the 2D-MOT. We investigate the system's performance for ^{88}Sr experimentation. A novel hybrid bi-color slowing scheme is proposed and realized using two crossed-polarized beams to address the magnetic-sensitive $m = 0 \rightarrow m = -1$ and magnetic-insensitive $m = 0 \rightarrow m = 0$ transitions of the $^1S_0 \rightarrow ^1P_1$ line. This approach aims to enhance the atomic flux, and we observe a 10-fold improvement in the number of atoms in 461 nm-MOT with the bi-color slowing beam. While this improvement is smaller than the 20-fold enhancement achieved with a Zeeman slower adopting an optimal magnetic field profile [86], our system demonstrates comparable performance in terms of the number of atoms prepared in the blue MOT, amounting to approximately 10^9 atoms. Notably, our system offers advantages in terms of simplicity, compactness, and lower power consumption compared to previous approaches [86], thanks to the short distance between the oven and 2D MOT, as well as the transverse loading of the 2D MOT.

Following the 461 nm-MOT, the 689 nm-MOT is performed to cool the atom below 1 μK via the narrow intercombination line $^1S_0 \rightarrow ^3P_1$. Around 10^7 ultra-cold atoms are prepared in 689 nm MOT, which gives the transfer efficiency below 5%. This transfer efficiency is mainly limited by the power of the 689nm beam during the last stage of red MOT. While lower power contributes to achieving a lower temperature, it reduces the number of atoms during the process.

Moreover, we implement an active control of the stray magnetic field to compensate slow-varying fluctuations around the 50 Hz of the AC line. With this active compensation, a typical rms magnetic field noise of 10 μG at low frequency (0.001 to 5 Hz) and 370 μG between 10 and 100 Hz are achieved. The enhanced stability benefits a Sr MOT operated on the 689 nm transition by minimizing induced position fluctuations.

In our experimental setup, three standing waves operating at 813.427 nm are generated to create

the optical lattice. Two of them are aligned on the horizontal plane and one is along the vertical axis. One of the horizontal standing waves overlaps with 698 nm laser beam for the implementation of clock transition. The vertical lattice, consisting of two cross-polarized beams, serves as the moving lattice for Bragg diffraction. The magnetically induced spectroscopy is implemented in this system, where an 80 G magnetic field and 50W/cm^2 are applied to achieve a Rabi frequency of 360 Hz, preparing the atoms in a statistical mixture of the ground ^{1}S$_0$ and excited ^{3}P$_0$ clock states. Furthermore, velocity selection is carried out using Bragg pulses to prepare the atomic sample with a temperature around 180 nK ($0.76\hbar k$).

With the prepared atomic sample, we explored a dual atom interferometer scheme, where the atoms in ^{1}S$_0$ and ^{3}P$_0$ clock states are simultaneously manipulated by the same interferometric sequence. The interferometer is based on Bragg pulses operating at 813.427 nm magic-wavelength, where we observe a differential phase-shift between two clock states in a free-falling Mach-Zehnder interferometer. This can be interpreted as a verification of the weak equivalence principle. Notably, we found an Eötvös ratio at the level of 10^{-4}.

Moreover, our dual atom interferometer scheme enables the determination of the state-dependent forces. This is demonstrated and studied by introducing an extra light field gradient on the interferometer trajectory. The large differential polarizability induces an extra state-dependent accumulated phase in the dual interferometer.

The achieved sensitivity level in our dual AI scheme, while moderate compared to the state-of-the-art platforms [29][23], is mainly limited by the finite temperature of the prepared atomic sample, restricting the interrogation time to few milliseconds. The free expansion during dark time and time-of-flight period makes it challenging to spatially separate different momentum states, thereby reducing the signal-to-noise ratio during detection image analysis. Additionally, the initial velocity introduces off-resonant effects in Bragg diffraction, leading to the complexity of velocity classes. Strategies such as large momentum transfer and temperature reduction may be employed to overcome this limitation.

The dual atom interferometer scheme holds promising potential for future applications. Firstly, while the current experiment utilized a clock-statistical mixture, future studies could investigate the test of the quantum weak equivalence principle utilizing pure states [109]. The test operator

$$\hat{M}_g \hat{M}_i^{-1} \approx \begin{pmatrix} r_1 & r \\ r^* & r_2 \end{pmatrix} \tag{6.1}$$

can be implemented. Here $\hat{M}_\alpha = m_\alpha \hat{I} + \frac{\hat{H}_\alpha}{c^2}$ is the mass-energy operators for inertial ($\alpha = i$) and gravitational ($\alpha = g$) mass, and $\hat{H}_\alpha$ is the contribution from the internal energy to the inertial and gravitational mass. In the context of classical weak equivalence principle, we have $r_1 = r_2 = 1$, which can be tested by different species of atoms or atoms in a statistical mixture of internal states, as discussed in this thesis. Furthermore, the quantum weak equivalence principle is valid if $r = 0$. This off-diagonal term reflects the coupling between different energy eignstates and can be tested using pure states. Based on the dual atom interferometer scheme with clock transition in strontium atoms,

one can envision a test of the quantum weak equivalence principle in the optical domain. This holds the potential to enhance the test by several orders of magnitude compared to tests conducted in the radio-frequency domain that have been previously reported [29].

Moreover, most accelerometers and gravimeters typically let the atoms evolve in free space, accumulating phase with $\phi = k_{\text{eff}} a T^2$. However, achieving higher sensitivity requires larger interferometry setups. An interesting alternative might be replacing the free-falling scheme with guided interferometry, where atoms are spatially frozen midway in the interferometer sequence in an optical lattice for an extended period, enabling the accumulation of phase in the gravitational potential. This approach, demonstrated in previous works, like those cited in references [110] and [111], could potentially render the experimental setup more compact compared to the traditional free-falling Mach-Zehnder interferometer. A potential systematic effect in trapped interferometry could be the phase shift due to the trap. Our dual atom interferometer scheme may provide a potential strategy for the measurement of this light shifts. When the dual atom interferometer is performed with different internal states, by adding the lattice beam on the interferometry path (shown in Figure 5.9), the differential light shift between the two states can be obtained from the phase shift of the two fringes. This information might prove useful in post-processing to account for systematic phase shifts arising from trapping potentials. The same method can also be utilized in the evaluation of polarizability. In addition, the state-dependent force measurement opens up the possibility to resolve the information of the environment such as magnetic field, since a differential acceleration $\delta a \propto B \cdot \delta B$ can be encoded into the phase shift in the fringes of dual atom interferometer.

Lastly, this scheme holds for measuring the time-dilation effects using atom interferometry. The traditional setups like free-falling Mach-Zehnder and Ramsey-Bordé type are not sensitive to the gravitational redshift. However, it has been proposed that the asymmetric Ramsey-Bordé geometry with the internal state splitting can resolve the proper time difference in spacial relativity [112]. This concepts might be demonstrated with the dual atom interferometer system. Additionally, measurements of relativistic or gravitational redshift have been reported on non-interferometric systems using either an optical clock in motion [113] or two incoherent optical clocks located at two different altitude in the Earth's gravitational field [113][114][115]. However, so far there is no test of gravitational red shift using atom interferometer, where the clock shall be activated either before [31] or during [32] the interferometeric sequence. By modifying the scheme of dual atom interferometer and implementing the wave-guided atom interferometer discussed in [31][32], it can be sensitive to gravitational redshift.

Bibliography

[1] M. S. Safronova, S. G. Porsev, U. I. Safronova, M. G. Kozlov, and Charles W. Clark. Blackbody-radiation shift in the Sr optical atomic clock. *Phys. Rev. A*, 87:012509, Jan 2013.

[2] Jianing Li, Kelvin Lim, Swarup Das, Thomas Zanon-Willette, Chen-Hao Feng, Paul Robert, Andrea Bertoldi, Philippe Bouyer, Chang Chi Kwong, Shau-Yu Lan, and David Wilkowski. Bi-color atomic beam slower and magnetic field compensation for ultracold gases. *AVS Quantum Science*, 4(4):046801, 12 2022.

[3] Frederic Leroux. *Non-Abelian geometrical quantum gate operation in an ultracold strontium gas.* PhD thesis, Nanyang Technological University, 2017.

[4] Nist database of atomic species. Last accessed: Nov 2023.

[5] Y. N. Martinez de Escobar, P. G. Mickelson, P. Pellegrini, S. B. Nagel, A. Traverso, M. Yan, R. Côté, and T. C. Killian. Two-photon photoassociative spectroscopy of ultracold ^{88}Sr. *Phys. Rev. A*, 78:062708, Dec 2008.

[6] A. Stein, H. Knöckel, and E. Tiemann. The 1S+1S asymptote of Sr2 studied by Fourier-transform spectroscopy. *The European Physical Journal D*, 57:171–177, Apr 2010.

[7] William D. Phillips and Harold Metcalf. Laser deceleration of an atomic beam. *Phys. Rev. Lett.*, 48:596–599, Mar 1982.

[8] E. L. Raab, M. Prentiss, Alex Cable, Steven Chu, and D. E. Pritchard. Trapping of neutral sodium atoms with radiation pressure. *Phys. Rev. Lett.*, 59:2631–2634, Dec 1987.

[9] Pippa Storey and Claude Cohen-Tannoudji. The Feynman path integral approach to atomic interferometry. A tutorial. *Journal de Physique II*, 4(11):1999–2027, 1994.

[10] Richard H. Parker, Chenghui Yu, Weicheng Zhong, Brian Estey, and Holger Müller. Measurement of the fine-structure constant as a test of the standard model. *Science*, 360(6385):191–195, 2018.

[11] Léo Morel, Zhibin Yao, Pierre Cladé, and Saïda Guellati-Khélifa. Determination of the fine-structure constant with an accuracy of 81 parts per trillion. *Nature*, 588:61–65, 2020.

[12] Mark Kasevich and Steven Chu. Atomic interferometry using stimulated Raman transitions. *Phys. Rev. Lett.*, 67:181–184, Jul 1991.

[13] Zhong-Kun Hu, Bu-Liang Sun, Xiao-Chun Duan, Min-Kang Zhou, Le-Le Chen, Su Zhan, Qiao-Zhen Zhang, and Jun Luo. Demonstration of an ultrahigh-sensitivity atom-interferometry absolute gravimeter. *Phys. Rev. A*, 88:043610, Oct 2013.

[14] T. Mazzoni, X. Zhang, R. Del Aguila, L. Salvi, N. Poli, and G. M. Tino. Large-momentum-transfer Bragg interferometer with strontium atoms. *Phys. Rev. A*, 92:053619, Nov 2015.

[15] M. J. Snadden, J. M. McGuirk, P. Bouyer, K. G. Haritos, and M. A. Kasevich. Measurement of the Earth's gravity gradient with an atom interferometer-based gravity gradiometer. *Phys. Rev. Lett.*, 81:971–974, Aug 1998.

[16] F. Sorrentino, Q. Bodart, L. Cacciapuoti, Y.-H. Lien, M. Prevedelli, G. Rosi, L. Salvi, and G. M. Tino. Sensitivity limits of a Raman atom interferometer as a gravity gradiometer. *Phys. Rev. A*, 89:023607, Feb 2014.

[17] T. L. Gustavson, P. Bouyer, and M. A. Kasevich. Precision rotation measurements with an atom interferometer gyroscope. *Phys. Rev. Lett.*, 78:2046–2049, Mar 1997.

[18] D. S. Durfee, Y. K. Shaham, and M. A. Kasevich. Long-term stability of an area-reversible atom-interferometer Sagnac gyroscope. *Phys. Rev. Lett.*, 97:240801, Dec 2006.

[19] S. Schlamminger, K.-Y. Choi, T. A. Wagner, J. H. Gundlach, and E. G. Adelberger. Test of the equivalence principle using a rotating torsion balance. *Phys. Rev. Lett.*, 100:041101, Jan 2008.

[20] T A Wagner, S Schlamminger, J H Gundlach, and E G Adelberger. Torsion-balance tests of the weak equivalence principle. *Classical and Quantum Gravity*, 29(18):184002, Aug 2012.

[21] James G Williams, Slava G Turyshev, and Dale H Boggs. Lunar laser ranging tests of the equivalence principle. *Classical and Quantum Gravity*, 29(18):184004, Aug 2012.

[22] Pierre Touboul, Gilles Métris, Manuel Rodrigues, Joel Bergé, Alain Robert, Quentin Baghi, Yves André, Judicaël Bedouet, Damien Boulanger, Stefanie Bremer, Patrice Carle, Ratana Chhun, Bruno Christophe, Valerio Cipolla, Thibault Damour, Pascale Danto, Louis Demange, Hansjoerg Dittus, Océane Dhuicque, Pierre Fayet, Bernard Foulon, Pierre-Yves Guidotti, Daniel Hagedorn, Emilie Hardy, Phuong-Anh Huynh, Patrick Kayser, Stéphanie Lala, Claus Lämmerzahl, Vincent Lebat, Fran çoise Liorzou, Meike List, Frank Löffler, Isabelle Panet, Martin Pernot-Borràs, Laurent Perraud, Sandrine Pires, Benjamin Pouilloux, Pascal Prieur, Alexandre Rebray, Serge Reynaud, Benny Rievers, Hanns Selig, Laura Serron, Timothy Sumner, Nicolas Tanguy, Patrizia Torresi, and Pieter Visser. *microscope* mission: Final results of the test of the equivalence principle. *Phys. Rev. Lett.*, 129:121102, Sep 2022.

[23] Peter Asenbaum, Chris Overstreet, Minjeong Kim, Joseph Curti, and Mark A. Kasevich. Atom-interferometric test of the equivalence principle at the 10^{-12} level. *Phys. Rev. Lett.*, 125:191101, Nov 2020.

[24] Sebastian Fray, Cristina Alvarez Diez, Theodor W. Hänsch, and Martin Weitz. Atomic interferometer with amplitude gratings of light and its applications to atom based tests of the equivalence principle. *Phys. Rev. Lett.*, 93:240404, Dec 2004.

[25] Lin Zhou, Shitong Long, Biao Tang, Xi Chen, Fen Gao, Wencui Peng, Weitao Duan, Jiaqi Zhong, Zongyuan Xiong, Jin Wang, Yuanzhong Zhang, and Mingsheng Zhan. Test of equivalence principle at 10^{-8} level by a dual-species double-diffraction Raman atom interferometer. *Phys. Rev. Lett.*, 115:013004, Jul 2015.

[26] Xiao-Chun Duan, Xiao-Bing Deng, Min-Kang Zhou, Ke Zhang, Wen-Jie Xu, Feng Xiong, Yao-Yao Xu, Cheng-Gang Shao, Jun Luo, and Zhong-Kun Hu. Test of the universality of free fall with atoms in different spin orientations. *Phys. Rev. Lett.*, 117:023001, Jul 2016.

[27] Brett Altschul, Quentin G. Bailey, Luc Blanchet, Kai Bongs, Philippe Bouyer, Luigi Cacciapuoti, Salvatore Capozziello, Naceur Gaaloul, Domenico Giulini, Jonas Hartwig, Luciano Iess, Philippe Jetzer, Arnaud Landragin, Ernst Rasel, Serge Reynaud, Stephan Schiller, Christian Schubert, Fiodor Sorrentino, Uwe Sterr, Jay D. Tasson, Guglielmo M. Tino, Philip Tuckey, and Peter Wolf. Quantum tests of the Einstein equivalence principle with the STE-QUEST space mission. *Advances in Space Research*, 55(1):501–524, Jan 2015.

[28] T. Kovachy, P. Asenbaum, C. Overstreet, C. A. Donnelly, S. M. Dickerson, A. Sugarbaker, J. M. Hogan, and M. A. Kasevich. Quantum superposition at the half-metre scale. *Nature*, 528:530–533, Dec 2015.

[29] G. Rosi, G. D'Amico, L. Cacciapuoti, F. Sorrentino, M. Prevedelli, M. Zych, C. Brukner, and G. M. Tino. Quantum test of the equivalence principle for atoms in coherent superposition of internal energy states. *Nature Communications*, 8:15529, Jun 2017.

[30] Savas Dimopoulos, Peter W. Graham, Jason M. Hogan, and Mark A. Kasevich. Testing general relativity with atom interferometry. *Phys. Rev. Lett.*, 98:111102, Mar 2007.

[31] Albert Roura. Gravitational redshift in quantum-clock interferometry. *Phys. Rev. X*, 10:021014, Apr 2020.

[32] Fabio Di Pumpo, Christian Ufrecht, Alexander Friedrich, Enno Giese, Wolfgang P. Schleich, and William G. Unruh. Gravitational redshift tests with atomic clocks and atom interferometers. *PRX Quantum*, 2:040333, Nov 2021.

[33] Christian Ufrecht, Fabio Di Pumpo, Alexander Friedrich, Albert Roura, Christian Schubert, Dennis Schlippert, Ernst M. Rasel, Wolfgang P. Schleich, and Enno Giese. Atom-interferometric

test of the universality of gravitational redshift and free fall. *Phys. Rev. Res.*, 2:043240, Nov 2020.

[34] Pierre Cladé. Bloch oscillations in atom interferometry. *La Rivista del Nuovo Cimento*, 38(4):173â207, Apr 2015.

[35] Guglielmo M. Tino, Angelo Bassi, Giuseppe Bianco, Kai Bongs, Philippe Bouyer, Luigi Cacciapuoti, Salvatore Capozziello, Xuzong Chen, Maria L. Chiofalo, Andrei Derevianko, Wolfgang Ertmer, Naceur Gaaloul, Patrick Gill, Peter W. Graham, Jason M. Hogan, Luciano Iess, Mark A. Kasevich, Hidetoshi Katori, Carsten Klempt, Xuanhui Lu, Long-Sheng Ma, Holger MÃŒller, Nathan R. Newbury, Chris W. Oates, Achim Peters, Nicola Poli, Ernst M. Rasel, Gabriele Rosi, Albert Roura, Christophe Salomon, Stephan Schiller, Wolfgang Schleich, Dennis Schlippert, Florian Schreck, Christian Schubert, Fiodor Sorrentino, Uwe Sterr, Jan W. Thomsen, Giuseppe Vallone, Flavio Vetrano, Paolo Villoresi, Wolf von Klitzing, David Wilkowski, Peter Wolf, Jun Ye, Nan Yu, and Mingsheng Zhan. SAGE: A proposal for a space atomic gravity explorer. *Eur. Phys. J. D*, 73(11):228, Nov 2019.

[36] Hidetoshi Katori, Masao Takamoto, V. G. Pal'chikov, and V. D. Ovsiannikov. Ultrastable optical clock with neutral atoms in an engineered light shift trap. *Phys. Rev. Lett.*, 91:173005, Oct 2003.

[37] Jun Ye, H. J. Kimble, and Hidetoshi Katori. Quantum state engineering and precision metrology using state-insensitive light traps. *Science*, 320(5884):1734–1738, Jun 2008.

[38] Andrei Derevianko and Hidetoshi Katori. Colloquium: Physics of optical lattice clocks. *Rev. Mod. Phys.*, 83:331–347, May 2011.

[39] Jean Dalibard, Fabrice Gerbier, Gediminas Juzeliūnas, and Patrik Öhberg. Colloquium: Artificial gauge potentials for neutral atoms. *Rev. Mod. Phys.*, 83:1523–1543, Nov 2011.

[40] Immanuel Bloch, Jean Dalibard, and Sylvain Nascimbéne. Quantum simulations with ultracold quantum gases. *Nature Physics*, 8:267–276, Apr 2012.

[41] N. R. Cooper, J. Dalibard, and I. B. Spielman. Topological bands for ultracold atoms. *Rev. Mod. Phys.*, 91:015005, Mar 2019.

[42] Xinye Xu, Thomas H. Loftus, Josh W. Dunn, Chris H. Greene, John L. Hall, Alan Gallagher, and Jun Ye. Single-stage sub-Doppler cooling of alkaline earth atoms. *Phys. Rev. Lett.*, 90:193002, May 2003.

[43] Thomas H. Loftus, Tetsuya Ido, Martin M. Boyd, Andrew D. Ludlow, and Jun Ye. Narrow line cooling and momentum-space crystals. *Phys. Rev. A*, 70:063413, Dec 2004.

[44] David Wilkowski. Runaway evaporation for optically dressed atoms. *Journal of Physics B: Atomic, Molecular and Optical Physics*, 43(20):205306, Oct 2010.

[45] M. Chalony, A. Kastberg, B. Klappauf, and D. Wilkowski. Doppler cooling to the quantum limit. *Phys. Rev. Lett.*, 107:243002, Dec 2011.

[46] Martin M. Boyd, Tanya Zelevinsky, Andrew D. Ludlow, Sebastian Blatt, Thomas Zanon-Willette, Seth M. Foreman, and Jun Ye. Nuclear spin effects in optical lattice clocks. *Phys. Rev. A*, 76:022510, Aug 2007.

[47] A. V. Taichenachev, V. I. Yudin, C. W. Oates, C. W. Hoyt, Z. W. Barber, and L. Hollberg. Magnetic field-induced spectroscopy of forbidden optical transitions with application to lattice-based optical atomic clocks. *Phys. Rev. Lett.*, 96:083001, Mar 2006.

[48] Robin Santra, Ennio Arimondo, Tetsuya Ido, Chris H. Greene, and Jun Ye. High-accuracy optical clock via three-level coherence in neutral bosonic ^{88}Sr. *Phys. Rev. Lett.*, 94:173002, May 2005.

[49] Tao Hong, Claire Cramer, Warren Nagourney, and E. N. Fortson. Optical clocks based on ultranarrow three-photon resonances in alkaline earth atoms. *Phys. Rev. Lett.*, 94:050801, Feb 2005.

[50] Xavier Baillard, Mathilde Fouché, Rodolphe Le Targat, Philip G. Westergaard, Arnaud Lecallier, Yann Le Coq, Giovanni D. Rovera, Sebastien Bize, and Pierre Lemonde. Accuracy evaluation of an optical lattice clock with bosonic atoms. *Opt. Lett.*, 32(13):1812–1814, Jul 2007.

[51] Vitaly D. Ovsiannikov, Vitaly G. Pal'chikov, Alexey V. Taichenachev, Valeriy I. Yudin, Hidetoshi Katori, and Masao Takamoto. Magic-wave-induced $^1\mathbf{S}_0 - ^3\mathbf{P}_0$ transition in even isotopes of alkaline-earth-metal-like atoms. *Phys. Rev. A*, 75:020501, Feb 2007.

[52] T. Akatsuka, M. Takamoto, and H. Katori. Optical lattice clocks with non-interacting bosons and fermions. *Nat. Phys.*, 4:954, Oct 2008.

[53] R. Le Targat, L. Lorini, Y. Le Coq, M. Zawada, J. Guéna, M. Abgrall, M. Gurov, P. Rosenbusch, D.G. Rovera, B. Nagórny, R. Gartman, P.G. Westergaard, M.E. Tobar, M. Lours, G. Santarelli, A. Clairon, S. Bize, P. Laurent, P. Lemonde, and J. Lodewyck. Experimental realization of an optical second with strontium lattice clocks. *Nat. Commun.*, 4:2109, Jul 2013.

[54] Andrew D. Ludlow, Martin M. Boyd, Jun Ye, E. Peik, and P. O. Schmidt. Optical atomic clocks. *Rev. Mod. Phys.*, 87:637–701, Jun 2015.

[55] Tobias Bothwell, Druv Kedar, Eric Oelker, John M Robinson, Sarah L Bromley, Weston L Tew, Jun Ye, and Colin J Kennedy. JILA SrI optical lattice clock with uncertainty of 2.0×10^{-18}. *Metrologia*, 56:065004, Jun 2019.

[56] Liang Hu, Nicola Poli, Leonardo Salvi, and Guglielmo M. Tino. Atom interferometry with the Sr optical clock transition. *Phys. Rev. Lett.*, 119:263601, Dec 2017.

[57] Peter W. Graham, Jason M. Hogan, Mark A. Kasevich, and Surjeet Rajendran. New method for gravitational wave detection with atomic sensors. *Phys. Rev. Lett.*, 110:171102, Apr 2013.

[58] S Kolkowitz, T. Bromley, S. L.and Bothwell, M. L. Wall, G. E. Marti, A. P. Koller, X. Zhang, A. M. Rey, and J. Ye. Spin-orbit-coupled fermions in an optical lattice clock. *Nature (London)*, 542:66, Feb 2017.

[59] Shankari V. Rajagopal, Kurt M. Fujiwara, Ruwan Senaratne, Kevin Singh, Zachary A. Geiger, and David M. Weld. Quantum emulation of extreme non-equilibrium phenomena with trapped atoms. *Ann, Phys.*, 529(8):1700008, May 2017.

[60] A. Heinz, A. J. Park, N. Šantić, J. Trautmann, S. G. Porsev, M. S. Safronova, I. Bloch, and S. Blatt. State-dependent optical lattices for the strontium optical qubit. *Phys. Rev. Lett.*, 124:203201, May 2020.

[61] Andrew J. Daley, Martin M. Boyd, Jun Ye, and Peter Zoller. Quantum computing with alkaline-earth-metal atoms. *Phys. Rev. Lett.*, 101:170504, Oct 2008.

[62] A. V. Gorshkov, A. M. Rey, A. J. Daley, M. M. Boyd, J. Ye, P. Zoller, and M. D. Lukin. Alkaline-earth-metal atoms as few-qubit quantum registers. *Phys. Rev. Lett.*, 102:110503, Mar 2009.

[63] A. Goban, R. B. Hutson, G. E. Marti, S. L. Campbell, M. A. Perlin, P. S. Julienne, J. P. D'Incao, A. M. Rey, and J. Ye. Emergence of multi-body interactions in a fermionic lattice clock. *Nature*, 563:369–373, Nov 2018.

[64] R P del Aguila, T Mazzoni, L Hu, L Salvi, G M Tino, and N Poli. Bragg gravity-gradiometer using the $^1S_0$-$^3P_1$ intercombination transition of ^{88}Sr. *New Journal of Physics*, 20(4):043002, Apr 2018.

[65] Tomoya Akatsuka, Masao Takamoto, and Hidetoshi Katori. Three-dimensional optical lattice clock with bosonic ^{88}Sr atoms. *Phys. Rev. A*, 81:023402, Feb 2010.

[66] Z. W. Barber, C. W. Hoyt, C. W. Oates, L. Hollberg, A. V. Taichenachev, and V. I. Yudin. Direct excitation of the forbidden clock transition in neutral ^{174}Yb atoms confined to an optical lattice. *Phys. Rev. Lett.*, 96:083002, Mar 2006.

[67] D.A. Steck. *Quantum and Atom Optics*. 2007.

[68] Tetsuya Ido and Hidetoshi Katori. Recoil-free spectroscopy of neutral Sr atoms in the Lamb-Dicke regime. *Phys. Rev. Lett.*, 91:053001, Jul 2003.

[69] Krehlik Przemyslaw Morzynski Piotr, Nawrocki Jerzy and et al. Absolute measurement of the $^1S_0$ - $^3P_0$ clock transition in neutral ^{88}Sr over the 330 km-long stabilized fibre optic link. *Scientific Reports*, 5:17495, Dec 2015.

[70] Matthew Norcia, Aaron Young, William Eckner, Eric Oelker, Jun Ye, and Adam Kaufman. Seconds-scale coherence on an optical clock transition in a tweezer array. *Science*, 366:eaay0644, Sep 2019.

[71] S. L. Campbell, R. B. Hutson, G. E. Marti, A. Goban, N. Darkwah Oppong, R. L. McNally, L. Sonderhouse, J. M. Robinson, W. Zhang, B. J. Bloom, and J. Ye. A fermi-degenerate three-dimensional optical lattice clock. *Science*, 358(6359):90–94, Oct 2017.

[72] Holger Müller, Sheng-wey Chiow, and Steven Chu. Atom-wave diffraction between the raman-nath and the Bragg regime: Effective Rabi frequency, losses, and phase shifts. *Phys. Rev. A*, 77:023609, Feb 2008.

[73] E.M. Wright and P. Meystre. Theory of an atomic interferometer in the Raman-Nath regime. *Optics Communications*, 75(5):388–396, Mar 1990.

[74] S. Gupta, K. Dieckmann, Z. Hadzibabic, and D. E. Pritchard. Contrast interferometry using Bose-Einstein condensates to measure h/m and α. *Phys. Rev. Lett.*, 89:140401, Sep 2002.

[75] C. Keller, J. Schmiedmayer, A. Zeilinger, T. Nonn, S. Dürr, and G. Rempe. Adiabatic following in standing-wave diffraction of atoms. *Applied Physics B*, 69:303–309, Oct 1999.

[76] Kathryn Moler, David S. Weiss, Mark Kasevich, and Steven Chu. Theoretical analysis of velocity-selective Raman transitions. *Phys. Rev. A*, 45:342–348, Jan 1992.

[77] Jason M. Hogan, David M. S. Johnson, and Mark A. Kasevich. Light-pulse atom interferometry. *arXiv, physics.atom-ph*, 0806.3261, Jun 2008.

[78] A Peters, K Y Chung, and S Chu. High-precision gravity measurements using atom interferometry. *Metrologia*, 38(1):25, Feb 2001.

[79] R. P. Feynman. Space-time approach to non-relativistic quantum mechanics. *Rev. Mod. Phys.*, 20:367–387, Apr 1948.

[80] R.P. Feynman, A.R. Hibbs, and D.F. Styer. *Quantum Mechanics and Path Integrals*. Dover Books on Physics. Dover Publications, 2010.

[81] Giacomo Lamporesi, Simone Donadello, Simone Serafini, and Gabriele Ferrari. Compact high-flux source of cold sodium atoms. *Rev. Sci. Instrum.*, 84(6):063102, Jun 2013.

[82] Ingo Nosske, Luc Couturier, Fachao Hu, Canzhu Tan, Chang Qiao, Jan Blume, Y. H. Jiang, Peng Chen, and Matthias Weidemüller. Two-dimensional magneto-optical trap as a source for cold strontium atoms. *Phys. Rev. A*, 96:053415, Nov 2017.

[83] Matteo Barbiero, Marco G. Tarallo, Davide Calonico, Filippo Levi, Giacomo Lamporesi, and Gabriele Ferrari. Sideband-enhanced cold atomic source for optical clocks. *Phys. Rev. Appl.*, 13:014013, Jan 2020.

[84] C. C. Kwong. *Coherent transmission of light through a cold atomic cloud*. PhD thesis, Nanyang Technological University, 2017.

[85] T. G. Tiecke, S. D. Gensemer, A. Ludewig, and J. T. M. Walraven. High-flux two-dimensional magneto-optical-trap source for cold lithium atoms. *Phys. Rev. A*, 80:013409, Jul 2009.

[86] Tao Yang, Kanhaiya Pandey, Mysore Srinivas Pramod, Frederic Leroux, Chang Chi Kwong, Elnur Hajiyev, Zhong Yi Chia, Bess Fang, and David Wilkowski. A high flux source of cold strontium atoms. *Eur. Phys. J. D*, 69(10):226, Oct 2015.

[87] Thierry Chanelière, Jean-Louis Meunier, Robin Kaiser, Christian Miniatura, and David Wilkowski. Extra-heating mechanism in Doppler cooling experiments. *Journal of the Optical Society of America B*, 22(9):1819, Sep 2005.

[88] K. Pandey, C. C. Kwong, M. S. Pramod, and D. Wilkowski. Linear and nonlinear magneto-optical rotation on the narrow strontium intercombination line. *Phys. Rev. A*, 93:053428, May 2016.

[89] W Kwiatkowski and S Tumanski. The permalloy magnetoresistive sensors-properties and applications. *J. Phys. E: Sci. Instr.*, 19(7):502–515, Jul 1986.

[90] Andrea Bertoldi, Davide Bassi, Leonardo Ricci, Daniele Covi, and Stefano Varas. Magnetoresistive magnetometer with improved bandwidth and response characteristics. *Rev. Sci. Instrum.*, 76(6):065106, May 2005.

[91] Bertoldi, A., Botti, L., Covi, D., Buffa, R., Bassi, D., and Ricci, L. Noise and response characterization of an anisotropic magnetoresistive sensor working in a high-frequency flipping regime. *Eur. Phys. J. Appl. Phys.*, 33(1):51–57, Jan 2006.

[92] C. C. Kwong, T. Yang, M. S. Pramod, K. Pandey, D. Delande, R. Pierrat, and D. Wilkowski. Cooperative emission of a coherent superflash of light. *Phys. Rev. Lett.*, 113:223601, Nov 2014.

[93] PJ Hobson, J Vovrosh, B Stray, M Packer, J Winch, N Holmes, F Hayati, K McGovern, R Bowtell, MJ Brookes, et al. Bespoke magnetic field design for a magnetically shielded cold atom interferometer. *arXiv preprint*, 2110.04498, Jun 2021.

[94] Silvia S Hidalgo-Tobon. Theory of gradient coil design methods for magnetic resonance imaging. *Concepts in Magnetic Resonance Part A*, 36(4):223–242, 2010.

[95] Long-Sheng Ma, Peter Jungner, Jun Ye, and John L. Hall. Delivering the same optical frequency at two places: accurate cancellation of phase noise introduced by an optical fiber or other time-varying path. *Opt. Lett.*, 19(21):1777–1779, Nov 1994.

[96] Yannick Bidel. *Piégeage et refroidissement laser du strontium, Etude de l'effet des interférences en diffusion multiple*. PhD thesis, Université Nice Sophia Antipolis, 2002.

[97] T. Zanon-Willette, S. Almonacil, E. de Clercq, A. D. Ludlow, and E. Arimondo. Quantum engineering of atomic phase shifts in optical clocks. *Phys. Rev. A*, 90:053427, Nov 2014.

[98] Thomas Zanon-Willette, Andrew D. Ludlow, Sebastian Blatt, Martin M. Boyd, Ennio Arimondo, and Jun Ye. Cancellation of stark shifts in optical lattice clocks by use of pulsed Raman and electromagnetically induced transparency techniques. *Phys. Rev. Lett.*, 97:233001, Dec 2006.

[99] T. Zanon-Willette, F. Impens, E. Arimondo, D. Wilkowski, A. V. Taichenachev, and V. I. Yudin. Robust quantum sensors with twisted-light fields induced optical transitions. *arXiv, physics.atom-ph*, 2306.17620, Sep 2023.

[100] Zeb Barber. *Ytterbium optical lattice clock.* PhD thesis, University of Colorado, Boulder, 2007.

[101] R. Hobson. *An Optical Lattice Clock with Neutral Strontium.* PhD thesis, University of Oxford, 2016.

[102] Benquan Lu, Xiaotong Lu, Jiguang Li, and Hong Chang. Theoretical calculation of the quadratic Zeeman shift coefficient of the clock state for strontium optical lattice clock. *Chinese Physics B*, 31(4):043101, Mar 2022.

[103] Travis L. Nicholson. *A new record in atomic clock performance.* PhD thesis, University of Colorado, Boulder, 2015.

[104] D. J. Wineland and Wayne M. Itano. Laser cooling of atoms. *Phys. Rev. A*, 20:1521–1540, Oct 1979.

[105] Wui Seng Leong, Mingjie Xin, Zilong Chen, Yu Wang, and Shau-Yu Lan. Large array of Schrödinger cat states facilitated by an optical waveguide. *Nature Communications*, 11:5295, Oct 2020.

[106] S. Blatt, J. W. Thomsen, G. K. Campbell, A. D. Ludlow, M. D. Swallows, M. J. Martin, M. M. Boyd, and J. Ye. Rabi spectroscopy and excitation inhomogeneity in a one-dimensional optical lattice clock. *Phys. Rev. A*, 80:052703, Nov 2009.

[107] A. Bonnin, N. Zahzam, Y. Bidel, and A. Bresson. Simultaneous dual-species matter-wave accelerometer. *Phys. Rev. A*, 88:043615, Oct 2013.

[108] Brian Vincent Estey. *Precision Measurement in Atom Interferometry Using Bragg Diffraction.* PhD thesis, UC Berkeley, 2016.

[109] Magdalena Zych and Caslav Brukner. Quantum formulation of the Einstein equivalence principle. *Nature Physics*, 14:1027–1031, Oct 2018.

[110] Victoria Xu, Matt Jaffe, Cristian D. Panda, Sofus L. Kristensen, Logan W. Clark, and Holger Müller. Probing gravity by holding atoms for 20 seconds. *Science*, 366(6466):745–749, Nov 2019.

[111] Cristian D. Panda, Matthew J. Tao, Miguel Ceja, and Holger Müller. Measuring gravity by holding atoms. *arXiv, physics.atom-ph*, 2310.01344, Oct 2023.

[112] Sina Loriani, Alexander Friedrich, Christian Ufrecht, Fabio Di Pumpo, Stephan Kleinert, Sven Abend, Naceur Gaaloul, Christian Meiners, Christian Schubert, Dorothee Tell, Étienne Wodey, Magdalena Zych, Wolfgang Ertmer, Albert Roura, Dennis Schlippert, Wolfgang P. Schleich, Ernst M. Rasel, and Enno Giese. Interference of clocks: A quantum twin paradox. *Science Advances*, 5(10):eaax8966, Oct 2019.

[113] C. W. Chou, D. B. Hume, T. Rosenband, and D. J. Wineland. Optical clocks and relativity. *Science*, 329(5999):1630–1633, Sep 2010.

[114] W. F. McGrew, X. Zhang, R. J. Fasano, S. A. Schäffer, K. Beloy, D. Nicolodi, R. C. Brown, N. Hinkley, G. Milani, M. Schioppo, T. H. Yoon, and A. D. Ludlow. Atomic clock performance enabling geodesy below the centimetre level. *Nature*, 564:87–90, Nov 2018.

[115] Masao Takamoto, Ichiro Ushijima, Noriaki Ohmae, Toshihiro Yahagi, Kensuke Kokado, Hisaaki Shinkai, and Hidetoshi Katori. Test of general relativity by a pair of transportable optical lattice clocks. *Nature Photonics*, 14:411–415, Jul 2020.